Aalborg Universitet

AALBORG UNIVERSITY
DENMARK

Control of Grid Interactive PV Inverters for High Penetration in Low Voltage Distribution Networks

Demirok, Erhan

Publication date:
2012

Document Version
Publisher's PDF, also known as Version of record

Link to publication from Aalborg University

Citation for published version (APA):
Demirok, E. (2012). Control of Grid Interactive PV Inverters for High Penetration in Low Voltage Distribution Networks. Department of Energy Technology, Aalborg University.

General rights
Copyright and moral rights for the publications made accessible in the public portal are retained by the authors and/or other copyright owners and it is a condition of accessing publications that users recognise and abide by the legal requirements associated with these rights.

? Users may download and print one copy of any publication from the public portal for the purpose of private study or research.
? You may not further distribute the material or use it for any profit-making activity or commercial gain
? You may freely distribute the URL identifying the publication in the public portal ?

Take down policy
If you believe that this document breaches copyright please contact us at vbn@aub.aau.dk providing details, and we will remove access to the work immediately and investigate your claim.

Downloaded from vbn.aau.dk on: April 25, 2017

Control of Grid Interactive PV Inverters for High Penetration in Low Voltage Distribution Networks

by

Erhan Demirok

Dissertation submitted to Faculty of Engineering, Science, and Medicine
at Aalborg University in partial fulfillment of the requirements
for the degree of Doctor of Philosophy in Electrical and Electronic Engineering

Aalborg University
Department of Energy Technology
Aalborg, Denmark
August 2012

Aalborg University
Department of Energy Technology
Pontoppidanstraede 101
9220 Aalborg East
Denmark
Phone: +45 9940 9240
Fax: +45 9815 1411
Web: http://www.et.aau.dk

Copyright © Erhan Demirok, 2012
Printed in Denmark by UniPrint
ISBN 978-87-92846-21-1

Abstract

Regarding of high density deployment of PV installations in electricity grids, new technical challenges such as voltage rise, thermal loading of network components, voltage unbalance, harmonic interaction and fault current contributions are being added to tasks list of distribution system operators (DSOs) in order to maintain at least the same power quality as before PVs were not revealed. Potential problems caused by high amount of PV installations can be avoided with technical study of both power system and power electronics areas that also benefit for new grid connection requirements. Any network management scheme or weakly-prepared grid connection requirements without paying attention to PV integration problems can bring potential risk of unintentional disconnections of these generating plants that likely increase payback time and extra energy losses of these renewable energy sources. On the other hand, unnecessarily strict grid connection requirements may cause less utilization of solar potential and may lead to additional cost on PV plants.

PV based generating plants are basically interfaced to electricity grid via power inverters. Hardware and control design requirements of these inverters may depend on grid connection rules which are forced by DSOs. Minimum requirement expected from PV inverters is to transfer maximum power by taking direct current (DC) form from PV modules and release it into AC grid and also continuously keep the inverters synchronized to the grid even under distorted conditions. Chapter 2, therefore; overviews the latest ancillary services such as real power reduction during over frequency/over voltage events and reactive power control for static grid voltage support function of PV inverters. In case of high density of PV integration, grid connection

rules which do not consider interaction among multiple PV inverters with the grid may allow unlimited number of PV plant connections and lead to unstable network operation. Harmonic emissions from multiple inverters connected to the same feeder and resulting in a network resonance can be a good example for this problem but PV inverters connected to highly capacitive networks are able to employ extra current and voltage harmonics compensation to avoid triggering network resonances at low order frequencies. The barriers such as harmonics interaction, flicker, fault current contribution and dc current injections from inverters can be figured out as long as the maximum PV hosting capacity of networks fully exploits available solar potential of geographical region. Therefore, grid voltage rise and thermal limits of network components will be considered as the most prevalent barriers in the thesis.

One of the focuses in this thesis is to develop a simulation tool and methodology for the estimation of maximum PV hosting capacity of LV distribution networks based on grid voltage rise and transformer hot-spot temperature limitations (Chapter 3 and 4). Rooftop PV installations in power capacity below 6 kWp have widespread usage in residential areas and are usually single-phase connected to 230/400-V grid. Since realistic assessment of PV integration should include both single- and three-phase PV connections, a three-phase load flow script which is able to allow more precise estimation of PV hosting capacity in unbalanced cases has been developed in Chapter 3 for future studies. Modeling of power system components has been revised in three-phase coordinates. The developed script has been validated with comparison results obtained from IEEE distribution test networks and from commercial software within the tolerable errors.

Current status on planning and operation of distribution networks has been also briefly summarized from PV integration perspective in Chapter 4. The possible network problems arisen from high penetration of PV plants or in other words, network limitation factors against increasing PV penetration to further levels can differ depending on network structures. For example, voltage rise will likely be essential limiting factor in the networks which have long-distant feeders. Unfortunately, there is

no a unique network structure, but at least, critical reference LV networks can be characterized from statistical analysis of real networks. Therefore, reference models of critical LV networks (suburban and farm) from literature have been revised and accordingly, their PV hosting capacities have been estimated by means of the developed load flow calculations. Invoking thermal model of distribution transformers can also contribute on more accurate estimation of PV hosting capacity.

As the other focus, the most considerable work of this thesis has been dedicated to the local voltage support methods of PV inverters in Chapter 5. The objective here is to compensate voltage rise owing to PV systems by absorbing reactive power from the grid. Thus, more PV power can be allowed for grid connection as long as steady-state grid voltage is in admissible range. However, grid voltage support of PV inverters by reactive power control is limited in distribution networks. The main reasons are high R/X ratio of LV networks, PV inverter current limitation, transformer and cable/line thermal limits with increased reactive power flow. Therefore, the highest voltage drop should be realized with minimum reactive power absorption from the grid. Weak points of voltage support strategies which were already imposed by grid codes have been underlined and two new methods have been proposed. In order to prevent unnecessary reactive power absorption from the grid during admissible voltage range or to increase reactive power contribution from the inverters during grid overvoltage condition, the proposed methods have been inherited from standard *cos(φ)* and *Q(U)* methods by combining their properties. Finally, both simulation and experimental validation of these methods have been provided in Chapter 5.

Acknowledgements

Acknowledgements are given to the Danfoss Solar Inverter A/S and Aalborg University for the financial support for this PhD project.

The PhD project was carried out under supervision of Prof. Remus Teodorescu (as main supervisor), Assoc. Prof. Dezso Sera (co-supervisor for the whole period) from Aalborg University, Denmark and Prof. Pedro Rodriguez (co-supervisor for the first two year) from Abengoa Research, Spain. My deepest gratefulness goes to my supervisors for their guidance, encouragement and valuable contributions throughout my doctorate study. Additionally, many thanks to the technical steering committee of my doctorate study composed of Dr. Uffe Borup and Dr. Søren B. Kjær from Danfoss Solar Inverters A/S for their helpful comments and suggestions in progress of the project.

I would like to thank Kenn H. B. Frederiksen from EnergiMidt A/S, Denmark and Carl Stephansen from GasCon/EnviDan A/S, Denmark for their help involved in getting distribution network layouts, energy measurement data and further technical discussions.

Special thanks to Dr. Georg Kerber from EnBW Regional AG in Stuttgart, Germany, my colleagues Martin Loedl and Peter Esslinger from the Associated Institute of Power Transmission Systems at Technical University of Munich, Germany where I spent my three-month study abroad period with their kind hospitability.

I want to thank to all my colleagues from Department of Energy Technology for their friendship and company..

Special thanks go to Omer Goksu, Mufit Altin, Osman S. Senturk, and Assoc. Prof. Tamas Kerekes for sharing their experience and time with me during my doctorate study

Table of Contents

Chapter 1
Introduction

This chapter presents the background and the motivation of the thesis, followed by the aims of the project, continuing with a list of the main contributions and concluding with the outline of the thesis.

1.1 Background and Motivation

20-% target of total energy production from renewables until 2020 and national stimulations around Europe make renewable sources more attractive. Although electricity cost generated from photovoltaics (PV) is still high at the moment, recent results from European Photovoltaic Industry Association (EPIA) shows that PV is highly accelerated and coming into picture with more amounts as compared to the other renewable sources (Fig. 1.1) [1.1]. For example, PV installation booming has been clearly observed in Denmark from 2010 to 2011 by means of introducing net-metering tariff for private residential and institution units. More than 58% of the cumulative installed capacity has been realized only in 2011 and grid-connected distributed PV applications constitute large amount (90% by the end of 2011) of the cumulative installed PV capacity [1.2]. Thus it is expected that electricity generation prices will become well-balanced between wind and PV technologies in near future around Europe.

This increasing amount of solar photovoltaic (PV) installations into electrical power systems can create potential risk of unintentional trips of these sources which likely

increase payback time and energy losses unless network and PV system interconnection issues (such as voltage rise, thermal loading of equipments, voltage unbalance, flicker, harmonic emissions, network resonance, direct current injections, fault current contribution etc.) are taken into consideration. "Connect and forget" concept of PVs has to be transformed to the "grid integration" concepts that can provide optimum reactions against grid disturbances in the sense of more energy harvesting from high penetration of distributed sources. New concepts aligned to the "grid integration" can be accomplished by either low-cost local control of PV units without communication infrastructures or centralized/decentralized control with communication medium.

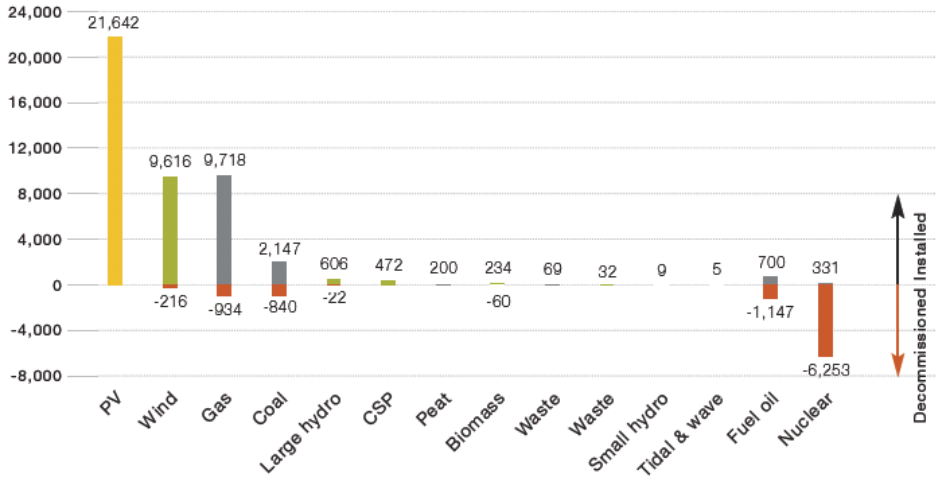

Fig. 1.1. Power generation capacities added in the EU 27 in 2011 (MW) published in EPIA global market outlook report [1.1].

1.2 Aims of the Project

1.2.1 Problem Formulation

The penetration level is already coming to the point where limitation of PV connection is in question anymore in order to avoid high cost of network reinforcements realized by distribution network operators (DNOs). Accordingly, maximum distributed

generation and minimum network reinforcement at the same time is becoming a challenging task. Voltage rise, thermal limits of components, voltage unbalance, network losses, harmonic emissions, network resonance and dc injections are the possible problems which need detail attention when high number of PV generators is integrated into the network.

Grid voltage limitation and ***thermal overloading*** of network components (transformers, cables etc.) are considered as the most prevalent barriers for high penetration of PV systems in distribution networks. Voltage limit usually becomes more critical than the thermal overloading of network equipments in rural and farm distribution networks since thermal limits of transformers and cables are usually high enough not to create overloading condition but long radial feeders can elevate the equivalent impedance seen by the PV systems. The question of how much voltage rise is allowed with DG connections is clearly defined in EN 50160 [1.3] based grid codes as ±10% band in most European countries. On the other hand, some inverter control measures [1.4] such as reactive power absorption from the grid when local voltage is being increased can cause equipment overloading in the network. Therefore, parameter settings of local voltage support strategies become a challenging task for reducing network losses, reactive energy consumption and thermal loading of network equipment.

Residential PV systems less than 5 kW ranges are mostly connected to the grid through single-phase inverters. In this case ***unbalanced power flow*** arises in the network if PV systems are connected unevenly to the grid among three phase lines. In addition to grid voltage rise and transformer thermal limits, voltage unbalance problem may become another notable limitation on the amount of PV connection. So, realistic three-phase network models are required to assess these problems with minimum level of assumptions.

1.2.2 Objective

The goal of this project is to analyse, model and develop new local voltage support strategies of PV inverters for increasing PV hosting capacity of low voltage (LV) distribution networks. A new simulation tool that accounts of unbalances has been developed for future uses. Two new grid voltage support strategies based on reactive power supply are proposed, investigated and verified by extensive load flow simulations and implementation.

1.2.3 Limitations

In reality, *irradiance* is the primary energy source for PV systems. Electrical power generated by PV modules can additionally vary depending on *ambient/module temperature* and *DC voltage* across the modules. Among these, irradiance and ambient temperature are environmental factors that are not controllable and only DC voltage is regulated in such a way that maximum DC power is extracted from the modules by means of maximum power point trackers (MPPT). Then, DC-AC voltage source inverters are employed to interface DC power to the distribution network. After all, certain level of power will be lost through MPPT, converters, wiring, etc. During this study, for the sake of simplicity, rated power of PV systems are directly specified as kW and kVAr referenced to the grid side and are modelled as constant P-Q sources. In future study, irradiance level on the module surface and ambient temperature can be specified as input data, and average models of converters can be exploited with realistic conversion efficiency curves. Distributed PV inverters which are less than 10-kW ratings are taken into consideration in the project. Inverters implemented in the laboratory setup are limited to maximum 1.5-kW real power operation.

Regarding of steady-state voltage and transformer loading analysis, only fundamental frequency (50 Hz) voltages and currents are considered here.

As the most prevalent used structure, distribution networks are operated in radial configuration although some particular implementations may utilize meshed structure.

Therefore, in the context of this thesis, distribution networks have been limited to radial feeders.

Residential units (apartments, buildings) constituting loads and rooftop PV systems have actually diversified power consumption and generation profiles. However, in the thesis, identical average consumption and generation power profiles have been assigned equally to all residential units.

1.3 Main Contributions

A short list of contributions is included in the order they appear in the thesis.

- Modeling and simulation of distribution networks with 3-phase unbalanced load flow

By means of 3-phase load flow simulation tool developed in Matlab®, loads and distribution generators are able to be connected in single-phase or three-phase configurations. Thus, neutral currents, neutral-to-ground voltages, line-to-neutral voltages can be computed and eventually voltage unbalance can be investigated. The tool is also able to simulate various reactive power control strategies of state-of-the art PV inverters.

- Estimation of maximum PV hosting capacity of distribution networks

Diverse network constraints such as overvoltage limit, voltage unbalance index, equipment overloading and neutral current limitation are applied on the load flow simulations. Thermal model of distribution transformers have been exploited for more accurate estimation of maximum allowable PV connection.

- New static voltage support strategies based on reactive power supply of PV inverters have been proposed

New local grid voltage support methods, $cos\varphi(P,U)$ and $Q(U,P)$, have been proposed to reduce total reactive energy import (or grid losses) and to improve the voltage support coordination of PV inverters along radial feeder, in respectively. Resulting maximum allowable PV penetration levels with various reactive power methods are compared by the load flow simulations.

1.4 Outline of the Thesis

This thesis is divided into two parts: Part I – Report and Part II – Publications. Part I is a summary report of the work done throughout the research and contains 5 chapters.

Chapter 1: Introduction, focuses on the background and motivation regarding the research done in this thesis. Furthermore, the objectives and limitations of the project are enumerated. The chapter is concluded with the list of publications.

Chapter 2: Overview of static grid voltage support strategies with PV inverters, gives some important distributed PV-grid interaction issues reported in the literature. Recent grid standards related to connection of distributed generators into the low voltage (LV) distribution networks are presented to realize network limitations, followed by the discussions about the voltage support methods proposed so far to increase PV hosting capacity of LV networks. The chapter finishes with the summary of advantages and disadvantages of reactive power methods.

Chapter 3: New three-phase unbalanced load flow tool for distribution networks, presents an unbalanced three-phase load flow program that is mainly developed for investigation of steady-state voltage variations, thermal limits of network components and resulted power losses in distribution networks. A breadth-first search algorithm based ordering scheme is described and used with backward-forward sweep load flow solution. Next, power systems modeling of some components (lines/cables, transformers, voltage regulators, shunt capacitors and loads) are briefly given in three-phase representation. Finally, load flow solver developed in Matlab® is validated on IEEE 4-bus and 13-bus test networks. As an ancillary service provided by state of the art PV inverters, thus, different reactive power control strategies can be implemented by means of this tool.

Chapter 4: LV distribution networks and estimation of their maximum PV hosting capacities, presents a methodology for the estimation of photovoltaic (PV) hosting capacity of low voltage (LV) distribution networks. General considerations on network

planning procedure and typical network structures are given in the chapter. Steady-state voltage variations and thermal loading of transformers as two main limitations are addressed. Since distribution network characteristics are not unique, critical reference LV networks have been built and used to estimate the amount of maximum allowable PV connections.

Chapter 5: Increasing PV hosting capacity of LV distribution networks, presents and examines the static reactive power ancillary services of PV inverters which are connected to LV distribution networks by giving attention to the grid voltage support and grid losses. Two reference LV networks as described in the previous chapter have been used to evaluate reactive power methods in order to increase PV hosting capacity and the most predominant limitations of connecting more PV inverters are emphasized for each network type. Certain part of a real LV distribution network of Braedstrup suburban area in Denmark is also used in simulation as a case study model. Thermal model of transformer is employed in this case study. Regarding of the MV/LV transformer overloading and grid overvoltage limitations, new local grid voltage support methods (*cosφ(P,U)* and *Q(U,P)*) have been proposed. Resulting maximum allowable PV penetration levels with various reactive power methods are compared by load flow simulation.

1.5 List of Publications

I. Demirok, E., Gonzalez, P., Frederiksen, K.H.B., Sera, D., Rodriguez, P., Teodorescu, R., "Local reactive power control methods for overvoltage prevention of distributed solar inverters in low voltage grids", *IEEE Journal of Photovoltaics*, vol. 1, issue. 2, p. 174-182, 2011.

II. Demirok, E., Sera, D., Teodorescu, R., "Estimation of maximum allowable PV connection to LV residential power networks: A case study of Braedstrup", *1st International Workshop on Integration of Solar Power into Power Systems*, 24 October 2011, Aarhus, Denmark.

III. Demirok, E., Sera, D., Rodriguez, P., Teodorescu, R., "Enhanced local grid voltage support method for high penetration of distributed generators", *37th*

IEEE Annual Conference of Industrial Electronics Society (IECON), Melbourne, 7-10 November 2011.

IV. Demirok, E., Gonzalez, P.C., Svendsen, M.C., Frederiksen, K.H.B., Sera, D., Teodorescu, R., "Reactive power control strategy for distributed solar inverters in low voltage rural distribution grids without communication infrastructure", *IEEE Photovoltaic Specialists Conference (PVSC)*, Seattle, 2011.

V. Demirok, E., Frederiksen, K.H.B., Sera, D., Teodorescu, R., "An optimized reactive power control of distributed solar inverters in LV networks", *26th European Photovoltaic Solar Energy Conference and Exhibition (EUPVSEC)*, Hamburg, September 2011.

VI. Demirok, E., Sera, D., Teodorescu, R., Rodriguez, P., Borup, U., "Evaluation of the voltage support strategies for the low voltage grid connected PV generators", *IEEE Energy Conversion Congress and* Exposition, ECCE 2010, Atlanta, USA.

VII. Demirok, E., Sera, D., Teodorescu, R., Rodriguez, P., Borup, U., "Clustered PV inverters in LV networks: An overview of impacts and comparison of voltage control strategies", *Electric Power and Energy Conference (EPEC 2009)*, Canada.

1.6 Bibliography for Chapter 1

[1.1] *Global Market Outlook for Photovoltaics until 2016*, European Photovoltaic Industry Association, May 2012.

[1.2] *Trends Preview*, International Energy Agency (IEA) Task 1, July 2012.

[1.3] *Voltage characteristics of electricity supplied by public distribution systems*, EN 50160 Standard, 2009.

[1.4] *Erzeugungsanlagen am Niederspannungsnetz -Technische Mindestanforderungen fur Anschluss und Parallelbetrieb von Erzeugungsanlagen am Niederspannungsnetz (Generators connected to the low-voltage distribution network - Technical requirements for the connection to and parallel operation with low-voltage distribution networks)*, VDE-AR-N 4105, August 2011.

Chapter 2
Overview of Grid Static Voltage Support Strategies with PV Inverters

This chapter highlights how PV inverters could be actually a controllable element in distribution network by supporting the grid voltage profile; eventually maximizing their penetration level without violating power quality limits. Firstly, some important distributed PV-grid interaction issues reported in the literature are briefly presented. Then, recent grid standards related to connection of distributed generators into the low voltage (LV) distribution networks are mentioned to realize network limitations, followed by the discussions about the voltage support methods proposed so far to increase PV hosting capacity of LV networks. In conclusion, advantages and disadvantages of reactive power methods are summarized.

2.1 Background

The primary function of a PV inverter is to inject current synchronized with the grid where its magnitude depends on available PV power on the dc side and its angle with referenced to the grid voltage is adjusted in such a way that unity power factor is achieved unless reactive power service is requested by local network operator. Besides real power injection, secondary functions such as static reactive power service [2.1]-[2.10], low voltage fault ride-through (LVRT) [2.11], real power curtailment, voltage unbalance correction [2.12] can be added as ancillary services for providing reliable operation of distribution networks.

Some arising interaction problems between distributed generators (PV systems in this thesis) and LV networks can be grouped as: Voltage rise, harmonics, unintentional islanding, voltage dips and unbalance, DC injections and grid impedance variation.

2.1.1 Voltage rise

One of the notable impacts of high number of distributed PV inverters along LV network is the *voltage rise*. Fig. 2.1 demonstrates a typical radial feeder voltage profile under peak power consumption-no generation and light power consumption-maximum generation cases. The maximum voltage drop under peak consumption is an essential technical requirement of distribution network planning procedure so that tap settings of transformers and cross section of cables can be determined based on this requirement including economic considerations as well. However, when total power generation exceeds total consumption of the local feeder, then net power is exported to MV network. Depending on the amount of power flowing along the feeder, the cross-section of cables and feeder length, this reverse power flow will result in certain level of voltage boost. The highest voltage rise appears at the furthest end of the feeder due to more impedance seen by this node. Therefore, network operator should reserve an extra voltage margin for distributed PV systems in network planning stage by limiting PV connection capacity from the beginning.

2.1.2 Harmonics

One of the most concerns by network operators is the harmonic effect on public grid. The main question arises here as: Even individual PV inverters comply with standards; does the same thing happen with large number of PVs on the grid? On the other hand, which order harmonics induced by grid-interfaced inverters are the most critical? Considering network impedance and inverter output filters, the effect of high-order current harmonics are assumed to be damped sufficiently. However, it will be required to utilize big filters to suppress low-order harmonics from inverters therefore current controller based solutions must be developed for the low-order harmonics.

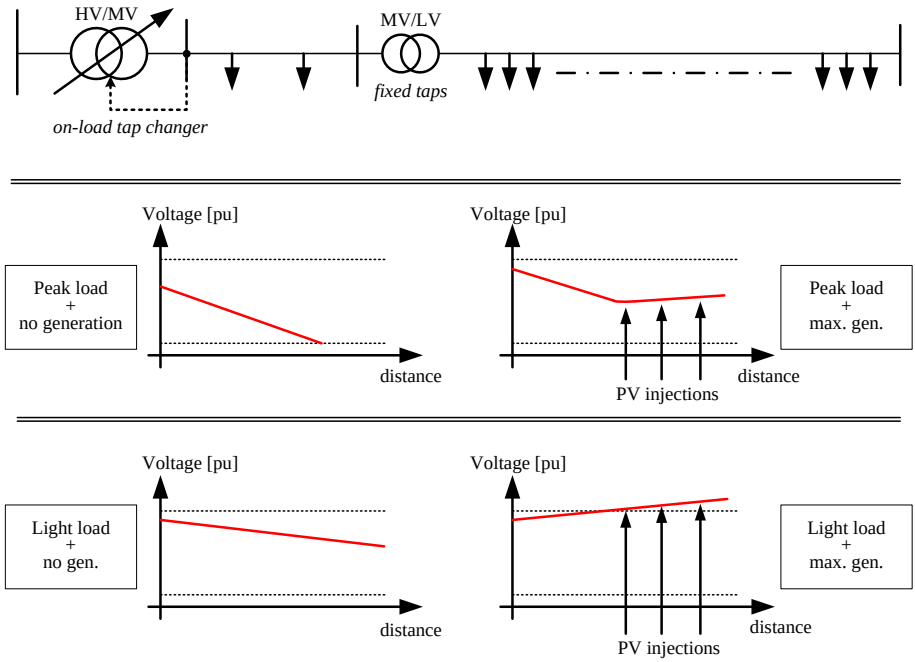

Fig. 2.1. Typical LV feeder voltage profile with various power consumption and generation amounts

Small distributed PV inverters might trigger a parallel resonance due to interaction between equivalent line inductance, capacitance of line and residential units, and injected harmonic currents by PV inverters. Especially, instead of using bigger inductors in the output filters, using larger capacitors are preferred by inverter manufacturers. Thus, equivalent resonance frequency of public LV network can decrease down to the fifth harmonic depending on the number of residential units, inverter output filter capacitances with high number of inverters, and line impedance [2.14].

Furthermore, normal operation of PV inverters might be also affected by background voltage distortions existing in the network if grid synchronization and current controllers are sensitive to the grid voltage. To improve the stability of PI current controllers especially during transients, grid voltage feed forward is typically included

with filters by having restricted bandwidth. In case of distorted voltages, injected currents will also have similar distortion so that current controllers can lead inverters to operate as negative resistors against to grid voltage distortions (see Fig. 2.2). Therefore, estimation of inverter harmonic current emissions based on ideal grid voltage conditions will not be adequate for indication of good performance. Unfortunately, grid standards at the time being do not impose current harmonic limits under non-ideal grid voltage cases.

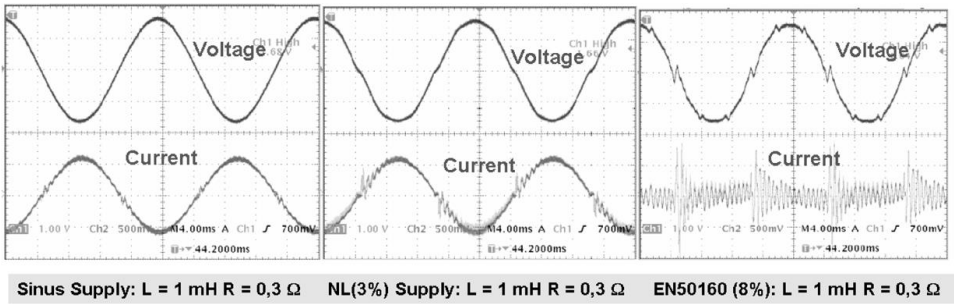

Fig. 2.2. Current emission of a PV inverter under perfect sinusoidal grid voltage-THD 0% (left), under the voltage THD 3% (middle), and under the voltage THD 8% (right). This test result is published in [2.14].

As highlighted in [2.15], some commercial inverters show different characteristics against background voltage distortion. Depending on the phase angle between injected current and grid voltage at the same harmonic, the inverter may attenuate, amplify or neutralize the grid voltage distortion.

Table 2.1 shows the conditions of harmonic voltage attenuation, neutralization and amplification from simulation results. Grid impedance angle at the H^{th} harmonic (ψ_{Hx}) will be required to damp or compensate voltage distortions [2.15].

Table 2.1. Harmonic current vs. voltage distortion [2.15].

	Attenuation	*Neutral*	*Amplification*
φ_{Hx}	$-\psi_{Hx}$	$90°-\psi_{Hx}$	$180°-\psi_{Hx}$

PV inverters can be tailored as parallel active filter for the attenuation of background voltage distortions. For example, in [2.16], an adjustable voltage harmonic compensator which can be integrated into distributed PV inverters has been proposed. A strategy of harmonic compensation in islanded operation has been also developed to share harmonic compensation loading between multiple inverters by using droop characteristic [2.17].

On the other hand, as an example, the effect of low solar irradiation level on injected current emissions is investigated in [2.18] with 14-kWp PV site measurements from Cyprus. Voltage and current THDs were monitored over a period of two weeks. As depicted in Fig. 2.3, total current THD is sensitive to irradiation changes whereas the total output voltage THD does not depend on irradiation level strongly.

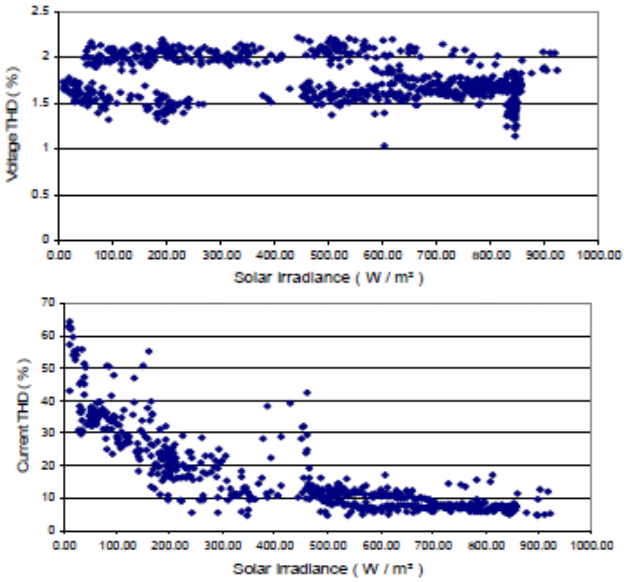

Fig. 2.3. Voltage (top) and current (bottom) THD vs. solar irradiance. This test result is published in [2.16].

2.1.3 Network islanding

Islanding is another interaction problem which should be taken into consideration when the penetration of PV inverters reach to critical levels compared to the peak demand capacity. Keeping in mind that most of the grid-connected inverters employ only inner current and outer dc voltage controllers based on the measured local grid voltage. In the absence of grid, voltage magnitude and its frequency will be determined by real and reactive power balance of total demand and generation in the isolated region. If a part of distribution network is disconnected due to maintenance purpose, short circuit faults or equipment failure, then inverters located in the isolated region shall cease current injection to avoid potential risks for line workers and damaging other electronic equipment. For this reason, islanding condition should be detected fast and accurately [2.19]-[2.20].

Islanding detection methods are mainly implemented in two ways assuming that a supervisory system with communication infrastructure does not exist in the network: Passive and active methods. While only local measurements are utilized to determine grid condition for passive methods, current or power injections by disturbing grid locally without loss of power quality are required for the active methods. In [2.21], passive methods are presented as over/under voltage (OUV), over/under frequency (OUF), voltage harmonics and phase monitoring based methods. Current harmonics injection, real/reactive power variation, capacitor connection, Sandia voltage shift (SVS), slip-mode frequency shift (SMS) methods are listed as active methods and their operation is basically based on perturbation of the local grid and measurement of the resulting grid voltage [2.22]. In case of multiple inverters located closer to each other, these grid perturbations due to islanding detection methods may cause unwanted inverter trips unless perturbation instances from multiple inverters are not synchronized.

2.1.4 Voltage dips

Voltage dip can be defined as drop of root-mean-square (RMS) of grid voltage in the range of 1-90 % of the nominal value within duration of half cycle to several seconds

[2.23]-[2.24]. Short circuits and high load start-ups are the main reasons of voltage dip. The characteristics of voltage dips can be in various types because a short circuit can be occurred in a symmetrical or unsymmetrical manner as depending fault type [2.25]. As the other power quality issue, *voltage dips*, may prevent normal operation of PV inverters if their controller structures are not properly designed. In [2.26], inverters' sensitivity to voltage dips has been investigated with 9 commercial inverters and typical behaviors of the inverters such as fast disconnection from the grid, current controller problem, the effect on the MPPT and ride-through have been outlined. Fig. 2.4 illustrates the evaluation results from [2.26] under different depth of voltage dips.

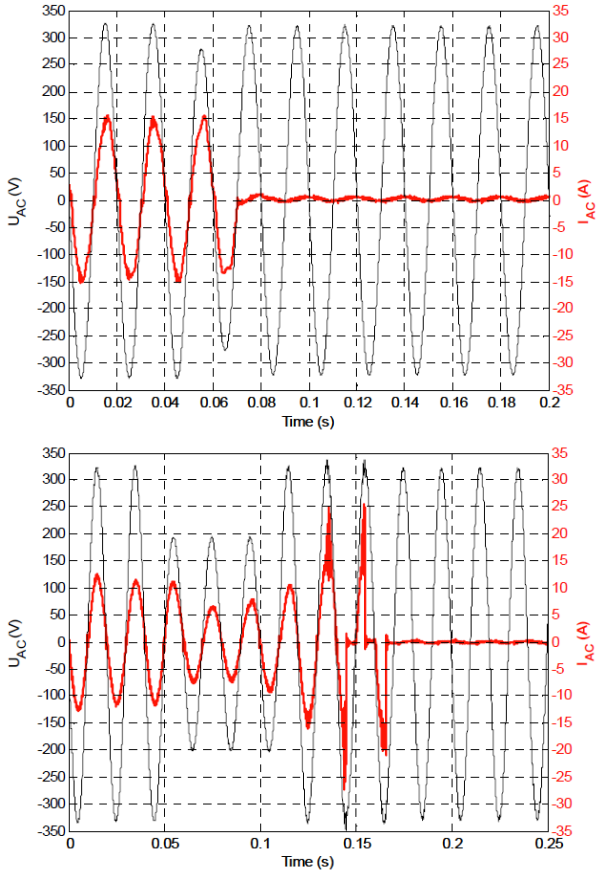

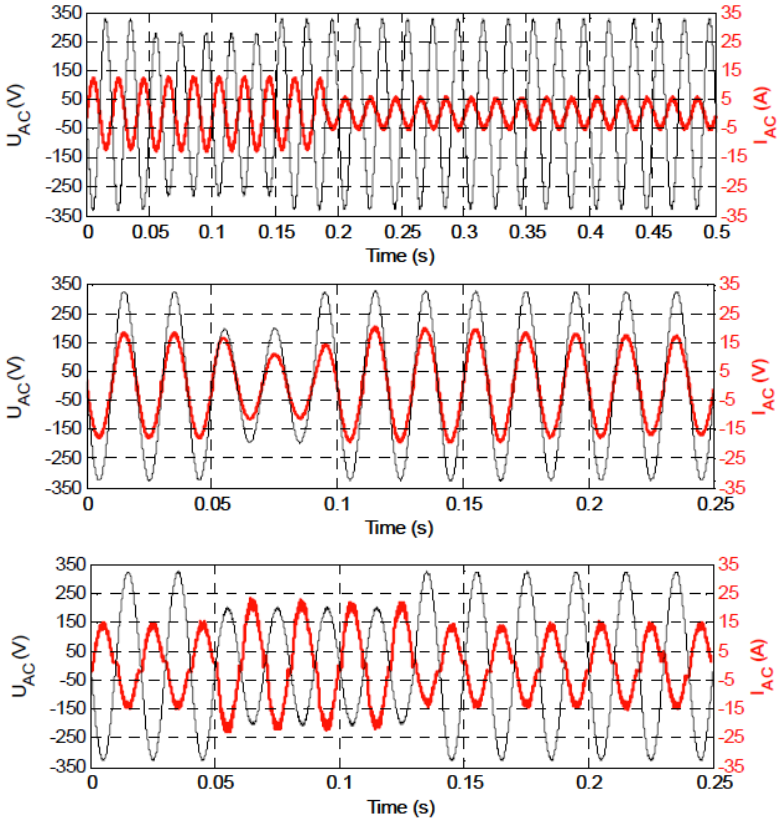

Fig. 2.4. Fast disconnection problem (first row), current controller problem (second row), slowness of MPPT (third row), good example of fast MPPT (fourth row), good example of ride-through (bottom). Test results are published by [2.26].

2.1.5 DC injections

DC current circulating in the network might saturate grid-interfaced magnetic components; generate pulsating torques, vibration and additional heating on electrical machines. Further on, half-cycle saturation causes reactive power loss in distribution transformers due to orthogonality of half-cycle current and voltage vectors [2.27]. Cyclo-converters and transformerless inverters are the potential reasons of dc current injection into LV network [2.28]-[2.29]. A dc detection device with disconnection feature for transformerless inverters is required in Germany, UK, Japan, Australia and

maximum allowable dc current varies between 0.5-1 percent of inverter rated current by various national standards [2.30].

2.1.6 Grid impedance variation

Grid interfaced inverters require output filter to attenuate high frequency contents in current. LCL filters have better stability and cost performance than L/LC/LLC filters with lower grid harmonic sensitivity [2.31]-[2.33]. However, active or passive methods are required to damp resonance frequency of LCL filter.

In [2.34]-[2.35], it is shown that if inverter with proportional + resonant (PR) controller and LCL filter are designed based on the stiff grid condition but it is connected to weak grid (higher grid inductance), then low frequency resonant controllers (at 5^{th} and 7^{th}) might be out of range of current controller bandwidth. Increasing proportional gain for extension of bandwidth can result in unstable closed-loop system. In similar way, at high frequency range, passive and active damping methods designed with respect to the strong grid condition become inefficient under weak grid condition. Accordingly, grid impedance information can increase the efficiency of active damping by adapting resonance damping of poles and zeros.

2.2 LV Grid Requirements for PV System Connections

In order to avoid energy yield deficiencies by PV systems and to provide reliable and stable grid operation, the grid-connected inverters must comply with certain country-specific or international grid standards imposed by distribution network operators. Focusing on grid support functions of the inverters, the essential norms can be listed as following:

- Grid voltage rise limitation due to distributed generation plants
- Automatic disconnection mechanism of generators
- Reconnection after trip
- Reactive power supply by generators
- Real power reduction of generators

Three standards, *EN 50160* (international) [2.23], *EN 50438* (international) [2.36] and *VDE-AR-N 4105* (Germany) [2.37], will be considered in this thesis. EN 50160 standard deals with the general norms for the network operator to maintain the supply voltage in normal conditions. On the other hand, EN 50438 and VDE-AR-N 4105 standards are more specifically related to the previously enumerated main norms of generators connected to distribution networks.

As the most important norm, *voltage rise limitation*, can directly affect the amount of generator connections to the grid. According to VDE-AR-N 4105 standard, maximum allowed voltage rise caused by the generators in LV networks is limited to ***3%***. Specifying this voltage rise limitation, network operators thus estimate maximum generator capacity of LV network by knowing individual generator rated power in kVA and their connection places. More details about voltage rise calculations are presented in Chapter 4. Once the amount of maximum generator connection capacity is determined, then regardless of whether allowed distributed generator capacity is fully utilized or not, steady-state grid voltage measured in 10-minute average must be maintained within the ±10% band of the nominal voltage both in MV and LV networks for 95% of a week as specified by EN 50160 standard. So, VDE-AR-N 4105 standard is applied at the network "planning" stage whereas EN 50160 deals with supply voltage at the network "operation" stage.

In case of abnormal grid conditions for a predetermined duration, the generators are required to stop energizing the grid, except for low-voltage ride-through (LVRT) feature which usually forces MV grid-connected generators to stay connected under voltage dip events. This automatic disconnection mechanism of generation plants (PV inverters in here) specifies over/under-voltage and over/under-frequency limit settings associated with their disconnection time as shown in Fig. 2.5. According to VDE-AR-N 4105, half-wave RMS voltages should be evaluated for the disconnection mechanism. Overvoltage condition (>1.1p.u.) is detected by forming 10-minute moving average of the measured voltage at every 3 seconds. Although 100 milliseconds is

specified as programmed disconnection time in VDE-AR-N 4105 standard, additional maximum 100-msec duration is permitted for the relay mechanics.

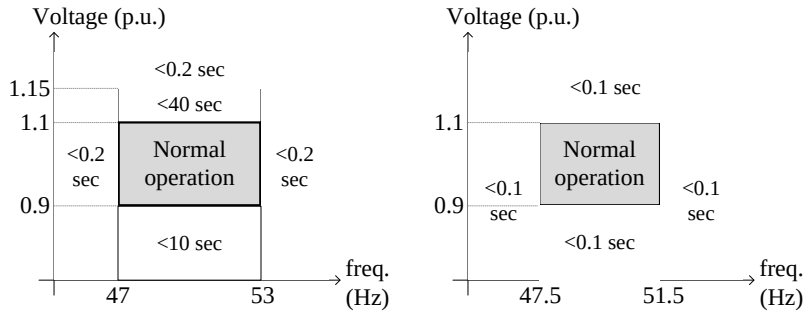

Fig. 2.5. Automatic disconnection mechanism settings. EN 50438 for Denmark (left) [2.36], VDE-AR-N 4105 (right) [2.37].

In order to prevent nuisance trip-reconnection cycles of the generators, VDE-AR-N 4105 standard introduces a norm for the reconnection after trip. The generator is allowed to connect back to the grid after trip as long as three following conditions are satisfied at the same time: (*0.85<V<1.1 p.u.*) & (*47.5<f<50.05 Hz*) & (minimum time *delay of 5 seconds*). During reconnection period, real power gradient is limited to $10\% \cdot P_{max}$ per minute.

Reactive power supply by the LV grid-connected generators is also specified in VDE-AR-N 4105. Allowable power factor operation ranges are defined as:

- If rated power of inverter is: $S_{rated} \leq 3.68$ kVA, then power factor (*PF*) operation can be limited to 0.95 leading and lagging according with EN 50438. No specification is introduced for the network operators.
- If $3.68kVA < S_{rated} \leq 13.8kVA$, the power factor control is limited to 0.95 leading and lagging. Corresponding PQ capability chart of the inverters is given in Fig. 2.6 (left).

- If $S_{rated} > 13.8kVA$, the power factor is limited to 0.90 leading and lagging as shown in Fig. 2.6 (right).

Implementation of reactive power supply can be realized by two different simple methods in LV networks: *fixed cosφ* and real power dependent power factor- *cosφ(P)* [2.37]. It is network operator's responsibility to select the suitable (optimized) reactive power strategy among these methods. Standard characteristic curve for *cosφ(P)* method is illustrated in Fig. 2.7. It should be noticed that reactive power supply starts only if output real power of the inverter exceeds a certain percent threshold (20%) of the rated power.

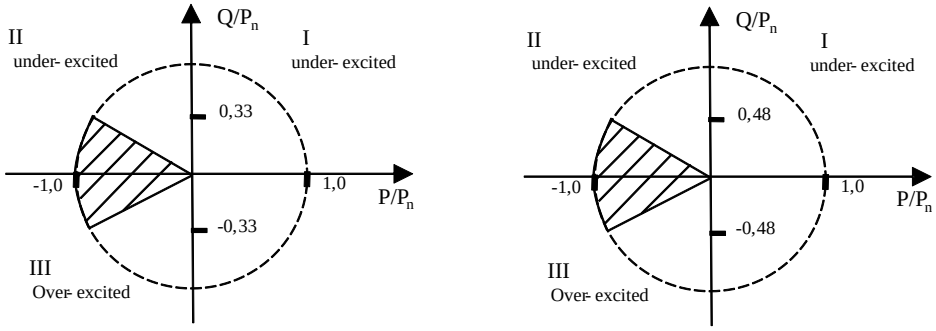

Fig. 2.6. PQ capability charts of the inverters for $3.68 < S_{rated} \leq 13.8$ kVA (left) and $S_{rated} > 13.8$ kVA (right) [2.37].

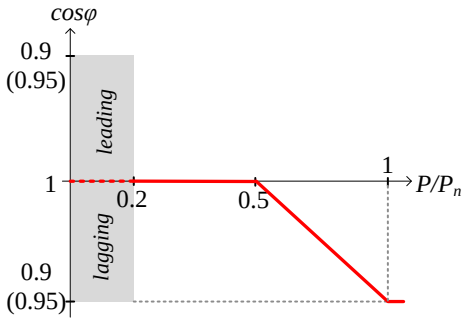

Fig. 2.7. PQ capability charts of the inverters for $3.68<S_{rated}\leq 13.8$ kVA (left) and $S_{rated}>13.8$ kVA (right) [2.37].

Thus, real power reduction of the inverters imposed by VDE-AR-N 4105 provides more controllable distributed generators to the network operators which are entitled to perform energy/network security management and frequency support. The inverters rated above 100 kW are required to reduce their real power outputs in increments of maximum 10% of the rated power. Otherwise, 100 %/60 %/30 %/0 % set points can be commanded by the network operators. Furthermore, inverters shall reach to real power set points in maximum one minute [2.37].

According to VDE-AR-N 4105, in case of over-frequency event (above 50.2 Hz), all controllable generators connected to LV networks are required reduce their real power outputs with a gradient of (see Fig. 2.8):

$$\Delta P = 0.4 \cdot P_{rated} \cdot \left(50.2 - f_{network}\right) \text{ for } 50.2 \leq f_{network} \leq 51.5Hz \qquad (2.1)$$

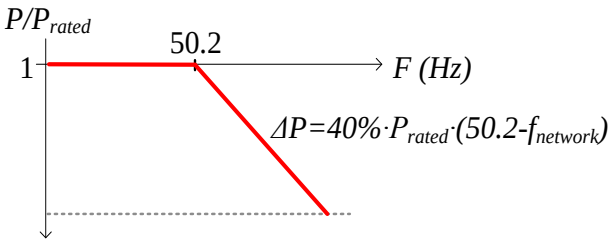

Fig. 2.8. Real power curtailment at over-frequency event [2.37].

It is obvious that grid voltage change criteria specified by both standards EN 50160 and VDE-AR-N 4105 are the most challenging limitation for the high PV penetration level. Therefore, this thesis deals with the voltage support methods helping to increase PV hosting capacity of distribution networks.

2.3 State-of-the-Art Strategies for Increasing PV Hosting Capacity of Distribution Networks

In this subsection, regarding of the voltage rise issue, some proved solutions from the literature to enable more generator connections are given briefly. The proved solutions mentioned here are not limited to only local autonomous operation of the generators in LV networks, but also the solutions requiring communication infrastructure have been considered. So, available grid voltage support strategies can be summarized as following:

1) Controlling real and reactive power supply of the generators,
2) Active transformer management,
3) Increasing cable cross-sections,
4) Energy storage,
5) Interconnecting distribution feeders (end nodes of feeders are connected),
6) Demand side management (DMS)

Real-reactive power control of the generators, active transformer management, energy storage system and DMS usually require a supervisory controller for optimal operation of the distribution networks whereas increasing cable cross-sections and interconnecting feeders are basically passive solution methods.

Load density, available network structure, technical and economical limitations will determine the most optimal solution. In [2.38], five different voltage support strategies except for real and reactive power control of the generators as listed above have been investigated. For instance, as comparing *solution 3* and *solution 4* with simulation of a test distribution network, the cost of battery has resulted ***36 times*** higher than the cost of cable doubling to reduce grid voltage level in the same amount [2.38]. However, revenue of the battery energy storage system can be increased further by combining it with demand side management system. Also, the location of storage system can affect the voltage support performance. The best result is achieved with the storage system connected to the end of feeder. As emphasized in [2.38], applying multiple voltage support solutions simultaneously could enhance the generator connection capacity

more. For instance, active transformer management and cable doubling together would increase the generator capacity without grid voltage violation equivalent to 5 times of the peak load. When each solution is utilized alone, then the maximum allowable generator connection capacity becomes 2 times of the peak load [2.38]. On the other hand, combination of the strategies does not always give the optimum result. It was investigated in the paper that the storage system and feeder interconnection strategies would result in a generator capacity with 2.7 times of the peak load.

In [2.39], the authors have employed three alternative voltage control solutions (real power curtailment, reactive power control and coordinated voltage control by using on-load tap changers-OLTC) on a 11-kV generic rural MV network model for increasing wind farm penetration level. An optimal power flow (OPF) has been developed with the following objective function [2.39]:

$$\phi = \min \sum_{i=1}^{n} C_t \cdot P_{Gi}^{curt} \tag{2.2}$$

where n is the total number of generators in the MV network, i is the node number, P_{Gi}^{curt} denotes the real power curtailment needed at i^{th} node, and C_t is the price of generation curtailment. In addition to objective function, network constraints (voltage and thermal limits, tap limits, reactive power limits) are also introduced to OPF. Then a wind farm is connected to a weak bus in the network with short-circuit power of 12 MVA. Annual generator revenue was a performance measure of active network control [2.39]. OLTC based coordinated voltage control has the highest revenue as penetration level increases (see Fig. 2.9) [2.39]. The least revenue was obtained at generation curtailment control. On the other hand, OLTC based coordinated voltage control would require communication infrastructure where this additional costs would decrease the revenue as well [2.39]. In the end, wind farm installation capacity has been increased 10 times by including OLTC control into active network management compared to lack of any solution.

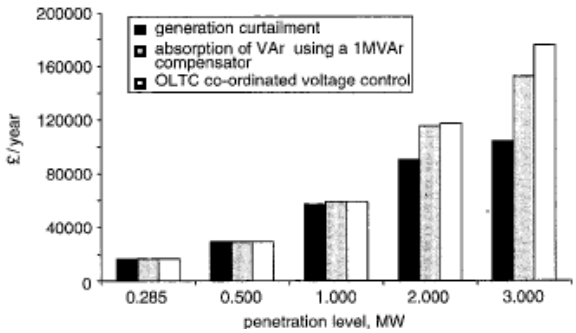

Fig. 2.9. Annual revenue comparison of a wind farm under different voltage control strategies. This simulation result published in [2.39].

If automation and communication platforms in distribution networks are not adequate to deliver and receive set commands/measurements to/from the generators and remote terminal units (RTUs), then local voltage support strategies could be fully utilized to enhance the connection capacity of the generators in the network. In [2.40], extensive load flow simulations on a particular MV network have been performed to assess different settings of local voltage dependent reactive power-*Q(V)* characteristic of PV inverters (shown in Fig. 2.10) on the voltage profile, network losses and total reactive energy imported. Dead-band, slope and minimum power factor are the required parameters to form a *Q(V)* characteristic. It was emphasized that dead-band should be used to reduce network losses and reactive energy import. Minimum power factor limit of 0.9 has been suggested for better voltage profiles. Eventually, the authors have proposed the following settings: V_n=1.05 p.u. (rated voltage after OLTC), V_{max}=1.09 p.u., *dead-band*=2%, *minimum power factor*=0.9 and the resulting *slope*=24.2 [2.40].

A local reactive power control has been proposed by Kerber et al. [2.10] on the basis of grid impedance measurement at each node. Location adaptive V-Q characteristic includes a dead-band as similar to Fig. 2.10 where the inverter operates at unity power factor in order to eliminate unnecessary reactive power flow on the network. Based on the value of equivalent impedance seen from the connection point toward the transformer, dead-band is adjusted in such a way that more reactive power would be

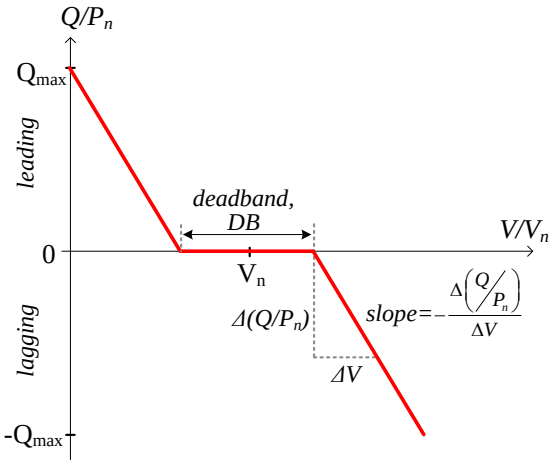

Fig. 2.10. Generic Q(V) characteristic for the voltage support [2.40].

absorbed by the inverter located at the end of feeder than that of the closest point to the transformer. Thus, total reactive power demand caused by the proposed strategy can be minimized while keeping the voltage in admissible range. The most important drawback is that available online grid impedance measurement techniques with high number of PV inverters running in parallel are highly possible to interact with each other in fact precision of impedance measurement can be largely influenced from neighbor inverters unless synchronization of signal injections is provided.

Another local voltage support method without need of communication infrastructure has been proposed by Tran-Quoc et.al. [2.41], [2.42]. Only output currents and voltages are measured to define local voltage window widths adaptively at each PV plant in terms of the location, the capacity of reactive power supply and local voltage. Using these data inputs, a fuzzy logic is then applied to calculate voltage window widths. In principle, if the local voltage is measured high, then the desired voltage window is maintained narrower (see Fig. 2.11). After determining voltage windows at each particular connection point, reactive and real power set values are generated on the basis of the local voltage condition (normal, perturbed, critical). In the normal state ($V_{min\_desired} \leq V \leq V_{max\_desired}$), PV inverter operates at unity power factor or PF/VAR

control mode. When the voltage moves into the yellow area ($V_{max\_desired} \leq V \leq V_{max\_admissible}$ or $V_{min\_admissible} \leq V \leq V_{min\_desired}$), only reactive power control is employed to support the local voltage. If reactive power is limited by the inverter, then local voltage continuously rises without ensuring any control capability. In this case, when the grid voltage level reaches to critical state, this time real power curtailment is managed in order to force the voltage being in admissible range (between 0.9 and 1.1p.u.) [2.41].

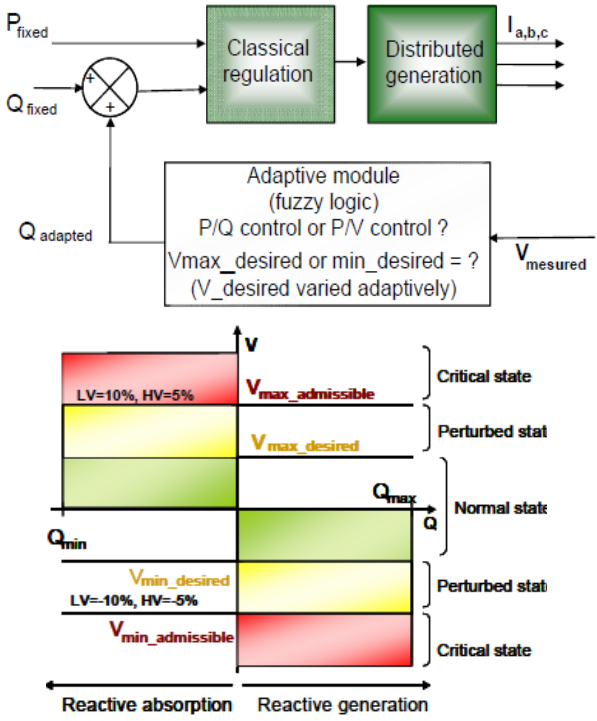

Fig. 2.11. Auto-adaptive local voltage support method [2.41]-[2.42].

2.4 Summary

Grid overvoltage condition is the most challenging problem with high penetration of PV systems in distribution networks. The side effects of other PV and grid interaction issues such as harmonics, voltage dips, etc. could be completely mitigated or reduced adequately with proper inverter controller design. However, grid overvoltage condition

may not be mitigated with PV inverters alone, and the severity of voltage rise problem also depends on the particular network characteristics (radial, long distant cables). The other possible control measures (active power management, energy storage, demand side management, cable doubling) can be also employed.

2.5 Bibliography for Chapter 2

[2.1] M. Braun, "Reactive power supply by distributed generators," *IEEE Power Energy Soc. Gen. Meeting*, pp. 1-8, July 2008.

[2.2] M. Braun, T. Stetz, T. Reimann, B. Valov, and G. Arnold, "Optimal reactive power supply in distribution networks – Technological and economic assessment for PV systems," *24th European Photovoltaic Solar Energy Conference*, Hamburg, September 2009

[2.3] J. Backes, C. Schorn, and H. Basse, "Cost-efficient integration of dispersed generation using voltage dependent reactive power control," *CIRED Workshop*, Lyon, France, 2010.

[2.4] B. Bletterie, A. Gorsek, B. Uljanic, "Enhancement of the network hosting capacity-Clearing space for/with PV," *25th European Photovoltaic Solar Energy Conference and Exhibition (EUPVSEC)*, Valencia, September 2010.

[2.5] C. Schwaegerl, M.H.J. Bollen, K. Karoui, A. Yagmur, "Voltage control in distribution systems as a limitation of the hosting capacity for distributed energy resources," *18th International Conference on Electricity Distribution Networks*, Turin, June 2005.

[2.6] P. Bousseau, E. Monnot, G. Malarange, O. Gonbeau, "Distributed generation contribution to voltage control," *International Conference on Electricity Distribution (CIRED)*, Vienna, May 2007.

[2.7] MetaPV Project, Deliverable D3.1, *Existing and Expectable Bottlenecks for the Integration of Large PV Generations Amounts*, Brussels, 2011.

[2.8] T. Stetz, W. Yan, M. Braun, "Voltage control in distribution systems with high level PV penetration-Improving absorption capacity for PV systems by reactive power supply," *25th European Photovoltaic Solar Energy Conference and Exhibition (EUPVSEC)*, Valencia, September 2010.

[2.9] G. Kerber, "Empfehlung zur Richtlinie zum Anschluss von Erzeugungs-anlagen an das Niederspannungsnetz (Recommendation on the policy for the capacity of generators connected to the low voltage networks)," Technical Report, Technical University of Munich, May 2009.

[2.10] G. Kerber, R. Witzmann, H. Sappl, "Voltage limitation by autonomous reactive power control of grid connected photovoltaic inverters," in *Conference on Compatibility and Power Electronics*, pp. 129-133, May 20-22, 2009.

[2.11] C.H. Benz, W.T. Franke, F.W. Fuchs, "Low voltage ride through capability of a 5 kW grid-tied solar inverter," *14th International Power Electronics and Motion Control Conference*, 2010.

[2.12] F. Wang, J.L. Duarte, M. Hendrix, "Control of grid-interfacing inverters with integrated voltage unbalance correction," *IEEE Power Electronics Specialists Conference*, pp. 310-316, June 2008.

[2.13] *Limit for harmonic current emissions (equipment input current ≤16A per phase),* EN 61000-3-2 Specification, 2004.

[2.14] J.H.R. Enslin, P.J.M Heskes, "Harmonic interaction between a large number of distributed power inverters and the distribution network," *IEEE Transactions on Power Electronics*, vol. 19, pp. 1586-1593, November 2004.

[2.15] C. Mayr, R. Brundlinger, B. Bletterie, "Photovoltaic inverters as active filters to improve power quality in the grid. What can state-of-the-art equipment achieve?" *9th International Conference on Electrical Power Quality and Utilisation*, October 2007.

[2.16] M. Hojo, T. Ohnishi, "Adjustable harmonic mitigation for grid-connected photovoltaic system utilizing surplus capacity of utility interactive inverter," *37th IEEE Power Electronics Specialists Conference*, PESC'06, pp. 1-6, 2006.

[2.17] T. Lee, P. Cheng, "Design of a new cooperative harmonic filtering strategy for distributed generation interface converters in an islanding network," *IEEE Transactions on Power Electronics*, vol. 22, pp. 1919-1927, September 2007.

[2.18] M. Patsalides et al, "The effect of solar irradiance on the power quality behavior of grid connected photovoltaic systems," *International Conference on Renewable Energy and Power Quality 2007* (ICREPQ 07), Sevilla, March 2007.

[2.19] *IEEE Recommended practice for grid interface of photovoltaic systems*, IEEE Standard 929-2000, 2000.

[2.20] *Standard for interconnecting distributed resources with electric power systems*, IEEE Standard 1547, 2003.

[2.21] F. De Mango, M. Liserre, A.D. Aquila, A. Pigazo, "Overview of anti-islanding algorithms for PV systems. Part I: Passive methods", 12th International *Power Electronics and Motion Control Conference*, pp. 1878-1883, September 2006.

[2.22] F. De Mango, M. Liserre, A.D. Aquila, "Overview of anti-islanding algorithms for PV systems. Part II: Active methods", *12th International Power Electronics and Motion Control Conference*, pp. 1884-1889, September 2006.

[2.23] *Voltage characteristics of electricity supplied by public distribution systems*, EN 50160 Standard, 2009.

[2.24] G. Yalcinkaya, M.H.J. Bollen, P.A. Crossley, "Characterization of voltage sags in industrial distribution systems," *IEEE Transactions on Industry Applications*, vol. 34, pp. 682-688, July-August 1998.

[2.25] M.H.J. Bollen, G. Olguin, M. Martins, "Voltage dips at the terminals of wind power installations," *Nordic Power Conference*, March 2004.

[2.26] B. Bletterie, R. Brundlinger, H. Fechner, "Sensitivity of photovoltaic inverters to voltage sags – Test results for a set of commercial products," *18th International Conference on Electricity Distribution*, Turin, June 2005.

[2.27] *DC Injection into Low Voltage AC Networks*, DTI technical report, 2005.

[2.28] L. Gertmar, P. Karlsson, O. Samuelsson, "On DC injection to AC grids from distributed generation," *EPE 2005*, 2005.

[2.29] Report IEA-PVPS T5-T10, "Impacts of power penetration from photovoltaic power systems in distribution networks", 2002.

[2.30] V. Salas, E. Olias, M. Alonso, F. Chenlo, "Overview of the legistlation of DC injection in the network for low voltage small grid-connected PV systems in Spain and other countries," *Renewable and Sustainable Energy Reviews*, vol. 12, pp. 575-583, 2008.

[2.31] M. Liserre, F. Blaabjerg, S. Hansen, "Design and control of an LCL-filter-based three-phase active rectifier," *IEEE Transactions on Industry Applications,* vol. 41, pp. 1281-1291, September/October 2005.

[2.32] S.V. Araujo, A. Engler, F.L.M. Antunes, "LCL filter design for grid-connected NPC inverters in offshore wind turbines," *The 7th International Conference on Power Electronics,* pp. 1133-1138, October 2007.

[2.33] Y. Tong, F. Tang, Y. Chen, F. Zhou, X. Jin, "Design algorithm of grid-side LCL-filter for three-phase voltage source pwm rectifier," *IEEE Power and Energy Society General Meeting-Conversion and Delivery of Electrical Energy in the 21st Century,* pp. 1-6, July 2008.

[2.34] M. Liserre, R. Teodorescu, F. Blaabjerg, "Stability of grid-connected PV inverters with large grid impedance variation," *35th Annual IEEE Power Electronics Specialists Conference,* pp. 4773-4779, 2004.

[2.35] M. Liserre, R. Teodorescu, F. Blaabjerg, "Stability of photovoltaic and wind turbine grid-connected inverters for a large set of grid impedance values," *IEEE Transactions on Power Electronics,* vol. 21, pp. 263-272, January 2006.

[2.36] *Requirements for the connection of micro-generators in parallel with public low-voltage distribution networks*, DS/EN 50438-2008.

[2.37] *Erzeugungsanlagen am Niederspannungsnetz - Technische Mindestanforderungen fur Anschluss und Parallelbetrieb von Erzeugungsanlagen am Niederspannungsnetz (Generators connected to the low-voltage distribution network - Technical requirements for the connection to and parallel operation with low-voltage distribution networks),* VDE-AR-N 4105, Aug. 2011.

[2.38] R. Niemi and P.D. Lund, "Alternative ways for voltage control in smart grids with distributed electricity generation," *International Journal of Energy Research,* 2011.

[2.39] S.N. Liew, G. Strbac, "Maximising penetration of wind generation in existing distribution networks," *IEE Proc.-Gener. Transm. Distrib,* Vol. 149, No. 3, May 2002.

[2.40] B. Bletterie, A. Gorsek, T. Fawzy, D. Premm, W. Deprez, F. Truyens, A. Woyte, B. Blazic and B. Uljanic, "Development of innovative voltage control for distribution networks with high photovoltaic penetration," *Progress in Photovoltaics: Research and Applications*, 2011.

[2.41] T. Tran-Quoc, E. Monnot, G. Rami, A. Almeida, C. Kieny, N. Hadjsaid, "Intelligent voltage control in distribution network with distributed generation," *19th International Conference on Electricity Distribution*, Vienna, May 2007.

[2.42] T. Tran-Quoc, T.M.C. Le, C. Kieny, N. Hadjsaid, S. Bacha, C. Duvauchelle, A. Almeida, "Local voltage control of PVs in distribution networks," *20nd International Conference on Electricity Distribution*, Prague, June 2009.

Chapter 3
A New Three-Phase Unbalanced Load Flow Tool for Distribution Networks

This chapter presents an unbalanced three-phase load flow program that is mainly developed for investigation of steady-state voltage variations, thermal limits of network components and resulted power losses in distribution networks. A breadth-first search algorithm based ordering scheme is described and used with backward-forward sweep load flow solution. Next, modelling of some power system components (lines/cables, transformers, voltage regulators, shunt capacitors and loads) are briefly given in three-phase representation. Finally, load flow solver developed in Matlab® is validated on IEEE 4-bus and 13-bus test networks. As an ancillary service provided by state of the art PV inverters, thus, different reactive power control strategies can be implemented by means of this tool.

3.1 Background

Power balance between generation-consumption and power quality are two essential targets on the overall electrical power system to be continuously maintained within the most economical way of delivery. Assuming that power balance, accordingly frequency control is provided by central generators under varying power demand conditions, network components will be exposed to certain amount of current and voltage stresses and will generate losses in the network. *Load flow* study here plays an important role as a tool to assess these stresses and network losses in the steady-state domain. Therefore,

objective of a load flow solution is to determine certain network state variables such as bus voltage magnitudes and angles, branch currents or power flows with the specified load and generators.

Minimum requirements of a load flow solution will vary depending on whether power system under study is transmission or distribution network. As an example, in transmission networks, power flow is usually balanced and the network structures likely involve meshed or looped lines. Regarding this, modelling of network components can be sufficient to represent as single phase components; and load flow solutions shall be developed in such a way that mesh structure is also covered. On the other hand, distribution networks in nature contain single-phase, two-phase, three-phase loads and four-wire cables/lines so that load flow solutions shall handle unbalanced power flow with three-phase modelling of network components. Since distribution networks mostly operate in radial structure, more straightforward and convergence guaranteed solutions can be provided by taking advantage of radial structure. A load flow solver tailored for three-phase unbalanced and meshed structures will be able to operate on both transmission and distribution networks; however, development of such a universal load flow solver is not focus of this dissertation. Therefore, only distribution network cases that a single slack bus is located at the beginning of the main feeder were considered when making decision on a suitable load flow method from several solutions. It is worth to notice that robustness against ill-conditioned situations, fast convergence and minimum memory allocation are common requirements for all types of load flow solutions.

Most of the load flow solvers proposed in the literature so far can be generally categorized into three groups:

- *Gauss-like* methods [3.1-3.4],
- *Newton-Raphson (NR)* based methods [3.5-3.13], and
- *Backward-forward sweep (BFS)* based methods [3.14-3.20],

The first version of load flow solvers were mostly based on Gauss-Seidel (GS) iterative methods that are resulting in poor convergence and high sensitivity to ill-conditioned situations for large-scale networks. In order to overcome these problems, network impedance matrix (Z_{bus}) based Gauss iterative method was proposed by H.E. Brown et.al. [3.1] in 1963. A similar approach (Gauss implicit Z_{bus}) but requiring less matrix formation subroutine was presented in [3.2] for finding solution of three-phase unbalanced distribution networks. Achieving less amount of computation time and preserving three-phase unbalanced situations were presented in [3.3] by means of phase-decoupled Gauss approach with implicit factorization of Y_{bus} matrix. Recently, an open source power system modelling and simulation environment, GridLAB-D, has been developed by U.S. Department of Energy in order to model smart grid applications in wide spectrum [3.4]. The simulation program currently uses GS method for the operation of transmission networks, and *BFS* method for the distribution networks that works separately. Three-phase current injection based *GS* method is being developed as reported in 2009 [3.4] so that a unique solver both for transmission and distribution networks will be implemented. The primary reason of choosing *GS* method is that the simulation environment can be performed on multiple processors as long as phase-decoupled Gauss approach is implemented. Another important reason is that GS method can start from poor initial guess voltages without loss of convergence although number of iteration increases to find the solution.

Application of *NR* iterative technique on the load flow studies firstly appeared in late 1950s [3.5]. However, at that period, *GS* based load flow solution methods were more common network planning tool until that optimally ordered and sparsity-oriented *NR* iterative programming techniques were developed to help improving memory space and ill-conditioned problems [3.6-3.7]. Today, *NR* based load flow method including its fast-decoupled and current injection variants [3.8-3.12] is widely employed in transmission networks for contingency and optimization analyses. Although *NR* based methods provide superior performance over the other methods in the sense of number of iterations, it may take longer time due to forming a Jacobian matrix and computing inverse Jacobian at each iteration. Regarding the distribution networks, first of all, large

number of branches and nodes with their corresponding phase components will make the size of Jacobian matrix bigger compared to that of transmission networks. Also, unsymmetrical, mutual couplings between phases and high R/X ratios of network components become more challenging in distribution networks due to singularity of Jacobian matrix. Decoupled Newton-like load flow methods [3.8-3.10] that assume low R/X ratios cannot be valid anymore in distribution networks. In [3.13], load flow solutions of several three-phase test networks with distributed generators (constant voltage mode) and voltage regulators were presented satisfactorily by exploiting sparsity methods and optimal ordering schemes in *NR* iterations.

As a last category of load flow solvers, *BFS* algorithm simply utilizes Kirchoff's circuit laws and takes advantage of special radial characteristics of distribution networks. Three-phase radial feeders were first time investigated in [3.14] and after that, ladder network theory was exploited in 1976 [3.2] as an iterative routine. In this and its variant methods, by starting from initial guess node voltages, load currents are calculated, all lateral/branch currents are sum up from end nodes towards the source node, and it is also possible that node voltages can be computed during this backward sweep process. In forward sweep process, specified source node voltage is set and, accordingly, subsequent node voltages are calculated by knowing the branch currents from the previous backward process. This iteration stops when termination requirement such as mismatch between the calculated and specified voltage magnitudes at source node meets a certain tolerance value. Nevertheless, this technique does not guarantee the convergence of load flow iterations if sequences of branches and nodes are not properly ordered. [3.16-3.18] proposed to enhance BFS method to solve weakly meshed structures in distribution networks using branch-oriented tree-numbering technique. A number of breakpoints are created on the interconnected meshed network and the resulting radial network is solved by means of BFS method. Equivalent current injections are inserted at the breakpoints using the multi-port compensation method in order to take network loops into account. On the other hand, as the number of breakpoints increases, the numerical efficiency of this method deteriorates. In [3.18], the same compensation-based load flow solution method was extended from single-

phase to three-phase weakly meshed distribution networks. Modelling of PV nodes (voltage controlled generators), voltage regulators, and unbalanced loads were also considered. More recently, direct approaches of BFS algorithms based on the branch-to-bus and bus-to-branch matrices have been presented in [3.19-3.20]. Since these matrices are only computed once, network solver can speed up the computation time. However, available direct approaches still need to be improved further by considering modelling of the transformers, line charging capacitances and voltage regulators.

To sum up, each load flow solution method will have certain limitations on the convergence, computation time, and network structure under study. Regarding of the focus of this dissertation, primary requirements expected from a load flow solver are listed as:

1. All class of loads such as 3-phase, 2-phase, single-phase and constant impedance, constant power, constant current or their combination shall be represented in a load flow study for more realistic investigation of grid voltage variations and thermal limits of components,
2. Load flow solver shall take into account of asymmetric layouts and mutual coupling situations of lines, cables and transformers,
3. Time-series simulation of load flow calculations is necessary for daily, monthly and yearly assessments. Therefore, the solver shall be fast enough to run load flow for one year with certain time-steps, e.g. every 15 minutes,
4. Ancillary services as given previously in Chapter 2 (*fixed cosφ*, *cosφ(P)*, *Q(U)*, and *P(U)*) shall be integrated into the load flow solver,
5. Load flow solver should be flexible to enable statistical study of electricity consumption and photovoltaic generation profiles.

Although the first three requirements can be provided by some commercial simulation packages (PowerFactory, NetBas, CYMDIST, etc.), a MATLAB® based unbalanced load flow solver will be developed through this chapter based on the various of state of the art publications from literature and will be used for the assessment of maximum PV hosting capacity of distribution networks. The aim of this chapter is to gain full

modelling and control capability on the distribution networks. Thus, any user-defined or standard ancillary services can be easily integrated into the same load flow calculations without need of a second program. A generalized functional block diagram is summarized in Fig. 3.1. Finally, *BFS* algorithm is selected as the most suitable solver among *Gauss-like* and *NR* methods by considering the primary requirements of unbalanced distribution networks.

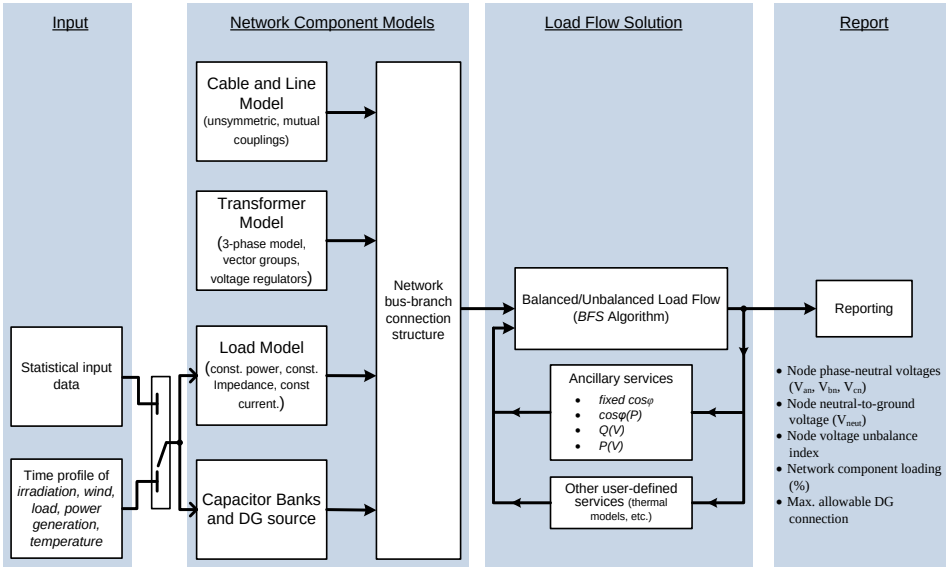

Fig. 3.1. Generalized functional block diagram of the load flow method developed in MATLAB®

3.2 Backward-Forward Sweep (BFS) Algorithm

The main difference of BFS algorithm compared to the other load flow solution algorithms is straightforward implementation of Kirchoff's current and voltage laws on the feeders. In this way, branch currents/power flows and bus voltages are updated by traversing between source and end nodes in iterative way. Specifying initial bus voltages (or flat start), backward sweep step determines the branch currents/power flows and updates the bus voltages by the summation of each load, generator and shunt

capacitor currents from end buses toward the source bus. Similarly, by following backward sweep step and starting from the specified source voltage level, forward sweep computes the voltage drop and updates branch currents/power flows along the feeder with its associated laterals. Backward and forward sweeps repeat in sequence until the bus voltages fulfil a certain convergence criteria. Several possibilities of current/power flows and voltage updates during backward-forward steps diversify the main concept of BFS algorithm in four different classes as presented in [3.21]:

1. Bus voltages as well as branch currents (*VI-VI-BFS*) or alternatively, bus voltages and branch power flows (*VS-VS-BFS*) are updated during both backward and forward steps,
2. Only bus voltages are updated during forward sweep. Backward sweep updates both bus voltages and branch currents/power flows (*V-VI-BFS* or *V-VS-BFS*),
3. Bus voltages as well as branch currents/power flows are updated during forward sweep, on the other hand only branch currents/power flows are updated during backward sweep (*VI-I-BFS* or *VS-S-BFS*),
4. In this class of BFS algorithm, bus voltages during forward sweep and branch currents/power flows during backward sweep are updated (*V-I-BFS* or *V-S-BFS*).

V-I-BFS algorithm will be considered for the rest of the dissertation due to having less computational burden compared to the other classes of BFS algorithm [3.21].

Regardless of what class of the algorithm is used, it should be noticed that BFS procedure shall follow the branch current and bus voltage updates along the branches in a proper sequence although the sequence of branches are not directly and properly provided by the user. Before adopted bus/branch numbering technique is presented in more details under the next sub-chapter 3.3, first of all, information which is required to form network bus-branch connection structure (Fig. 3.1) should be known. Therefore, solution of *V-I-BFS* algorithm on a simple two-bus system as shown in Fig. 3.2 will be summarized next.

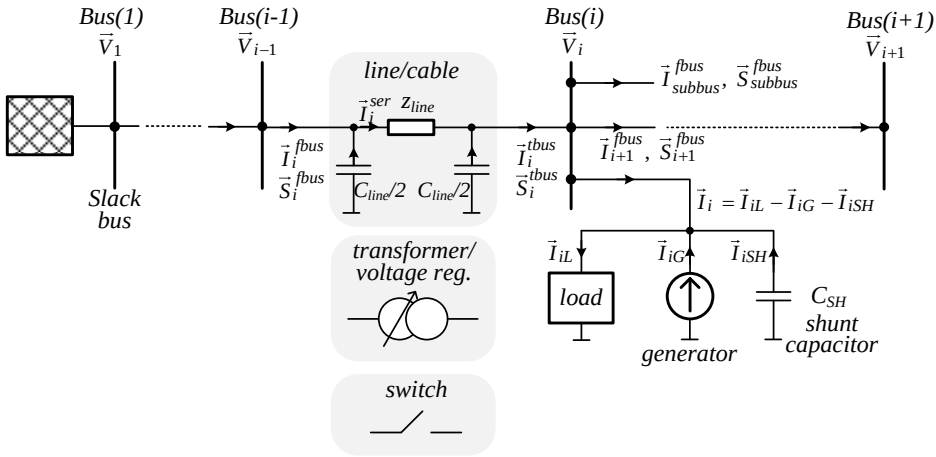

Fig. 3.2. Two-bus and single-line representation of distribution networks for the solution of *V-I-BFS* algorithm.

Backward Sweep Step:

Based on the initial bus voltages and given nominal ratings of shunt elements (loads, generators, shunt capacitors) at the i^{th} bus, corresponding shunt current injections ($\vec{I}_{iL}$, $\vec{I}_{iG}$, $\vec{I}_{iSH}$) are computed as a first step. Then, the "*incoming-to bus"* branch current ($\vec{I}_i^{tbus}$) is determined by summing up the all branched off currents at bus *i* as following:

$$\begin{bmatrix} \vec{I}_i^a \\ \vec{I}_i^b \\ \vec{I}_i^c \end{bmatrix} = \begin{bmatrix} \left\{ \left(S_{iL}^a - S_{iG}^a \right) / \vec{V}_i^a \right\}^* \\ \left\{ \left(S_{iL}^b - S_{iG}^b \right) / \vec{V}_i^b \right\}^* \\ \left\{ \left(S_{iL}^c - S_{iG}^c \right) / \vec{V}_i^c \right\}^* \end{bmatrix} - \begin{bmatrix} Y_i^a & 0 & 0 \\ 0 & Y_i^b & 0 \\ 0 & 0 & Y_i^c \end{bmatrix} \begin{bmatrix} \vec{V}_i^a \\ \vec{V}_i^b \\ \vec{V}_i^c \end{bmatrix} \tag{3.1}$$

$$\begin{bmatrix} \vec{I}_i^{tbus,a} \\ \vec{I}_i^{tbus,b} \\ \vec{I}_i^{tbus,c} \end{bmatrix} = \begin{bmatrix} \vec{I}_i^a \\ \vec{I}_i^b \\ \vec{I}_i^c \end{bmatrix} + \sum_{m \in M} \begin{bmatrix} \vec{I}_m^{fbus,a} \\ \vec{I}_m^{fbus,b} \\ \vec{I}_m^{fbus,c} \end{bmatrix} \tag{3.2}$$

where

{a,b,c} denotes the phase components,

S_{iL} and S_{iG} are the scheduled apparent power of load and generator at i^{th} bus,

$\vec{I}_i$ represents the current summation of shunt elements $\left(\vec{I}_{iL} - \vec{I}_{iG} - \vec{I}_{iSH}\right)$ at i^{th} bus,

$\vec{I}_i^{\,tbus}$ and $\vec{I}_i^{\,fbus}$ are "to bus" and "from bus" currents of the i^{th} branch (Fig. 3.2),

M is the set of sub-branches that are branched off the i^{th} bus.

Current flowing from the parent bus (incoming *"from bus"* current, $\vec{I}_i^{\,fbus}$) is updated in terms of incoming *"to bus"* current, line charging capacitors of the incoming branch, and bus voltages at two ends. If the incoming branch is cable or line that is represented in PI circuit form as shown in Fig. 3.2, then the resulting current in (3.2) can be easily reflected to current update at "*from bus"* side of the incoming branch ($\vec{I}_i^{\,fbus}$).

$$\vec{I}_i^{\,fbus} = f(\vec{I}_i^{\,tbus}, y_{C_{line}}, \vec{V}_i, \vec{V}_{i-1}) = \vec{I}_i^{\,tbus} + \frac{1}{2} y_{C_{line}} \vec{V}_i + \frac{1}{2} y_{C_{line}} \vec{V}_{i-1} \tag{3.3}$$

and in three-phase coordinates,

$$\begin{bmatrix} \vec{I}_i^{\,fbus,a} \\ \vec{I}_i^{\,fbus,b} \\ \vec{I}_i^{\,fbus,c} \end{bmatrix} = \begin{bmatrix} \vec{I}_i^{\,tbus,a} \\ \vec{I}_i^{\,tbus,b} \\ \vec{I}_i^{\,tbus,c} \end{bmatrix} + \frac{1}{2} \begin{bmatrix} y_{C_{line}}^{aa} & y_{C_{line}}^{ab} & y_{C_{line}}^{ac} \\ y_{C_{line}}^{ba} & y_{C_{line}}^{bb} & y_{C_{line}}^{bc} \\ y_{C_{line}}^{ca} & y_{C_{line}}^{cb} & y_{C_{line}}^{cc} \end{bmatrix} \begin{bmatrix} \left(\vec{V}_i^{\,a} + \vec{V}_{i-1}^{\,a}\right) \\ \left(\vec{V}_i^{\,b} + \vec{V}_{i-1}^{\,b}\right) \\ \left(\vec{V}_i^{\,c} + \vec{V}_{i-1}^{\,c}\right) \end{bmatrix}$$

More generally, the above equation can be extended for the other type of branches such as transformers, voltage regulators with three-phase and mutually coupled circuits.

$$\left[\vec{I}_i^{\,fbus}\right] = [C]\left[\vec{V}\right] + [D]\left[\vec{I}_i^{\,tbus}\right] \tag{3.4}$$

where

$$\left[\vec{I}_i^{\,tbus}\right] = \begin{bmatrix} \vec{I}_i^{\,tbus,a} & \vec{I}_i^{\,tbus,b} & \vec{I}_i^{\,tbus,c} \end{bmatrix}^T, [V] = \begin{bmatrix} \vec{V}_i^{\,a} & \vec{V}_i^{\,b} & \vec{V}_i^{\,c} & \vec{V}_{i-1}^{\,a} & \vec{V}_{i-1}^{\,b} & \vec{V}_{i-1}^{\,c} \end{bmatrix}^T,$$

[C] and [D] are coefficient matrices of the incoming branch. It should be noted that bus voltages are known from the previous forward sweep.

Forward Sweep Step:

Voltage drop along the branch is calculated in terms of the parent bus voltage ($\vec{V}_{i-1}$), "*from bus"* branch current ($\vec{I}_i^{fbus}$) obtained in the previous backward step and branch series impedance (z_{line}). Simply,

$$\vec{V}_i = \vec{V}_{i-1} - z_{line} \cdot \vec{I}_i^{ser} \tag{3.5}$$

where $\vec{I}_i^{ser}$ is the current passing through series impedance of the i^{th} branch. If $\vec{I}_i^{ser}$ is solved in connection with *"from bus"* branch current and substituted into (3.5)

$$\vec{V}_i = \vec{V}_{i-1} - z_{line} \cdot \left(\vec{I}_i^{fbus} + \frac{1}{2} y_{C_{line}} \vec{V}_{i-1} \right) = \left(1 - \frac{1}{2} \cdot z_{line} \cdot y_{C_{line}} \right) \vec{V}_{i-1} - z_{line} \cdot \vec{I}_i^{fbus} \tag{3.6}$$

Equation (3.6) can be extended to generalized three-phase and mutually coupled circuits as

$$\begin{aligned} \begin{bmatrix} \vec{V}_i^a \\ \vec{V}_i^b \\ \vec{V}_i^c \end{bmatrix} &= \left\{ \begin{bmatrix} 1 & & \\ & 1 & \\ & & 1 \end{bmatrix} - \frac{1}{2} \begin{bmatrix} z_{aa} & z_{ab} & z_{ac} \\ z_{ba} & z_{bb} & z_{bc} \\ z_{ca} & z_{cb} & z_{cc} \end{bmatrix} \begin{bmatrix} y_{C_{line}}^{aa} & y_{C_{line}}^{ab} & y_{C_{line}}^{ac} \\ y_{C_{line}}^{ba} & y_{C_{line}}^{bb} & y_{C_{line}}^{bc} \\ y_{C_{line}}^{ca} & y_{C_{line}}^{cb} & y_{C_{line}}^{cc} \end{bmatrix} \right\} \cdot \begin{bmatrix} \vec{V}_{i-1}^a \\ \vec{V}_{i-1}^b \\ \vec{V}_{i-1}^c \end{bmatrix} \\ &\quad - \begin{bmatrix} z_{aa} & z_{ab} & z_{ac} \\ z_{ba} & z_{bb} & z_{bc} \\ z_{ca} & z_{cb} & z_{cc} \end{bmatrix} \begin{bmatrix} \vec{I}_i^{fbus,a} \\ \vec{I}_i^{fbus,b} \\ \vec{I}_i^{fbus,c} \end{bmatrix} \\ &= [A] \cdot \left[\vec{V}_{i-1} \right] - [B] \cdot \left[\vec{I}_i^{fbus} \right] \end{aligned} \tag{3.7}$$

[A], [B], [C], [D] coefficient matrices of network elements in (3.4) and (3.7) which are suitable for *V-I-BFS* algorithm will be defined under the sub-chapter *3.4 Network*

Components. Only series impedance of lines or cables will be taken into account because the effect of line charging capacitors on voltage variation is negligible for short-distance distribution networks.

3.3 Data Preparation and Bus Numbering Technique

Backward-forward sweep algorithm as shown above converges to a unique and accurate solution as long as bus-branch connection structure for the whole network is provided. An *m-bus* distribution network is built by means of *(m-1) branch section*s. Each branch located between two buses (that is, *from bus* and *to bus*) is the only input data to the load flow solver. Based on [3.21] and considering *V-I-BFS* algorithm, assignment of five data types to every bus will be sufficient to form a bus-branch connection structure by traversing adjacency list of *(m-1)* branches. Table 3.1 presents the adopted bus data structure.

Table. 3.1. Bus data structure as proposed in [3.8] for the bus-branch connectivity of entire network

Bus data types	**Description**
bus(i).parent	parent bus of the i^{th} bus
bus(i).inbranch	incoming branch of the i^{th} bus
bus(i).nsubs	number of child bus(es) of the i^{th} bus
bus(i).next	the child bus located on the same lateral of the i^{th} bus
bus(i).subbus	the child bus located on the sub-lateral of the i^{th} bus

It is usual that the number of child buses may be more than two for distribution networks. Only one of them is chosen as *the next bus* to keep the backward or forward sweep running on the same lateral and the remaining child buses will be chosen as *sub-bus* which is located on the sub-lateral of their parent bus. Since selection of the next bus influences the resulting bus numbering as presented later in this section, a question comes into picture: How a lateral is identified as sub-lateral, in other words, among which child bus is considered on the same lateral with its parent? As proposed in [3.21] and by adding a new third criterion, the selection of *the next bus* among several child buses should be based on the following typical criteria for distribution networks:

1. If the parent bus branches off through a transformer, the corresponding lateral is considered as sub-lateral of the parent bus and the child bus located at the other side of the branch is classified as *subbus* class. This criterion conforms to the case of several branching off points on a MV main feeder through MV/LV transformers. Thus, any child bus located on the main MV feeder is assigned to *next* class,
2. If the number of phases at child bus is less than that of the parent bus, the corresponding child bus is added to *subbus* class,
3. Since voltage regulators are typically located on the main feeders, any child bus at the other side of voltage regulator is assigned to *next* class.

Next step will be to assign bus numbers in such a way that backward and forward sweeps can follow the sequential branches systematically between the source bus and end buses. A similar application can be also seen for the problem of finding the shortest-path between two nodes. Therefore, it allows us to adopt the same solution techniques from graph algorithms subject for the bus numbering of distribution networks. *Breadth-first* and *depth-first* search methods are the simplest graph algorithms to achieve this goal [3.23] and they are both classified under uninformed search methods. As distinct from depth-first method, breadth-first search method explores all the nodes reachable from the root node in a graph *G* (nodes are analogous to *m* buses and *G* corresponds to specified *(m-1)* branches in our case) and stops when there is no "untouched" child nodes anymore. Thus, data type assignments and numbering for every bus can be carried out within one breadth-first search over the *(m-1)* branches. Another advantage of breadth-search method is the applicability on mesh structured distribution networks because of producing inherently "breadth-first tree" form from the looped graphs.

Breadth-first search method starts from a selected root node *s*, and the algorithm assigns one of the states (or colors) such as *1*: *untouched (white)*, *2*: *in queue (gray)*, *3*: *done (black)* to child nodes in order to keep a record of progress. Initially, all nodes begin with state *1* by default, which is *untouched* condition. Besides, breadth-first

search method employs a FIFO (first-in, first-out) queue *Q* that contains only the nodes with state *2*. When a node is discovered the first time, its state is updated to *2* and the node is inserted into the first-in, first-out queue *Q*. Meanwhile, the first node of *Q* is popped out; its child nodes are explored, state number *2* is assigned to the corresponding child nodes, these new child nodes are inserted into *Q*, and state *3* is assigned to the popped out node. This progress continues until reaching to an empty *Q* or having all nodes in state *3*. Pseudo code of breadth-first search algorithm including bus data classes is presented at the next page.

An example progress of breadth-first search algorithm on a given 14-node looped graph is illustrated in Fig. 3.3. Node 1 is chosen as the root node, and it should be noticed that only nodes between *1* and *12* are reachable by the root node. By applying breadth-first search algorithm, a possible tree structure (G_1) from the given graph *G* is resulted as shown in Fig. 3.4. Generally, the output tree structure is not unique and may vary depending on the order of given adjacency list of the graph *G*. From Fig. 3.4,

$$G_1 \cap G_2 = \varnothing,\ G_1 \subset G \text{ and } G_2 \subset G$$

where G_1=BreadthFirst(G,s) and G_2={13,14}.

The property given above brings another advantage of the search algorithm before load flow calculation is initiated. It enables running load flow on multiple distribution feeders or microgrids which have individual isolated source nodes at the same time. Furthermore, breakpoints are inherently created on the looped graph and there will be no need of manually specifying breakpoints for solving weakly meshed networks.

Running time of breadth-first search algorithm is a critical property and can be determined in worst-case by knowing the number of nodes (*N*) and branches (*B*) in a graph. At initialization stage (line 1-3 in pseudo-code), all nodes are called and set to *untouched* state so that the time devoted to this stage will be *O(N)*. Besides on initialization duration, each node is enqueued and dequeued at most once during the entire search process. If single enqueuing and dequeuing operation takes *O(1)* time,

then *O(N)* will be the total time for this operation. Also, every branch in the given adjacency list of branches will be scanned two times at most (one visit by parent node and another visit by child node). Thus, the total time takes *O(B)* for this operation. As a result, the total running time of breadth-first search algorithm becomes *O(N+B)* and the operation shows time linear behaviour to the size of nodes and branches [3.23].

Pseudo code of breadth-first search algorithm:

```
Specify the graph G and root node s: BreadthFirst(G,s)
1       for each node u ∈ G-{s}
2               state(u) ← 1 (untouched)          % all nodes except s are in state 1,
3       end
4       state(s) ← 2 (in queue or gray)           % the root node s is in queue,
5       Q = []                                    % initialize an empty Q,
6       ENQUEUE(Q,s)                              % enqueue s onto Q,
7       while Q is non-empty
8               u ← DEQUEUE(Q)                    % u is the head element of Q,
9               for each node v adjacent to u     % for each child node of u,
10                      if state(v) == 1          % if v is encountered first time,
11                        state(v) ← 2            % v is in state 2,
12                        bus(v).parent ← u       % u is the parent bus of v,
13                        bus(v).inbranch ← G(v)  % find incoming branch of v from the
                                                  % specified adjacency list of branches,
14                        (bus(u).next) or (bus(u).subbus) ← v
15          bus(u).nsubs ← count(v)               % number of child bus(es),
16                        ENQUEUE(Q,v)            % enqueue v onto Q,
17                      end
18              end
19              DEQUEUE(Q)                        % pop out node u from Q,
20              state(u) ← 3                      % u is marked as 3 (done),
21      end
```

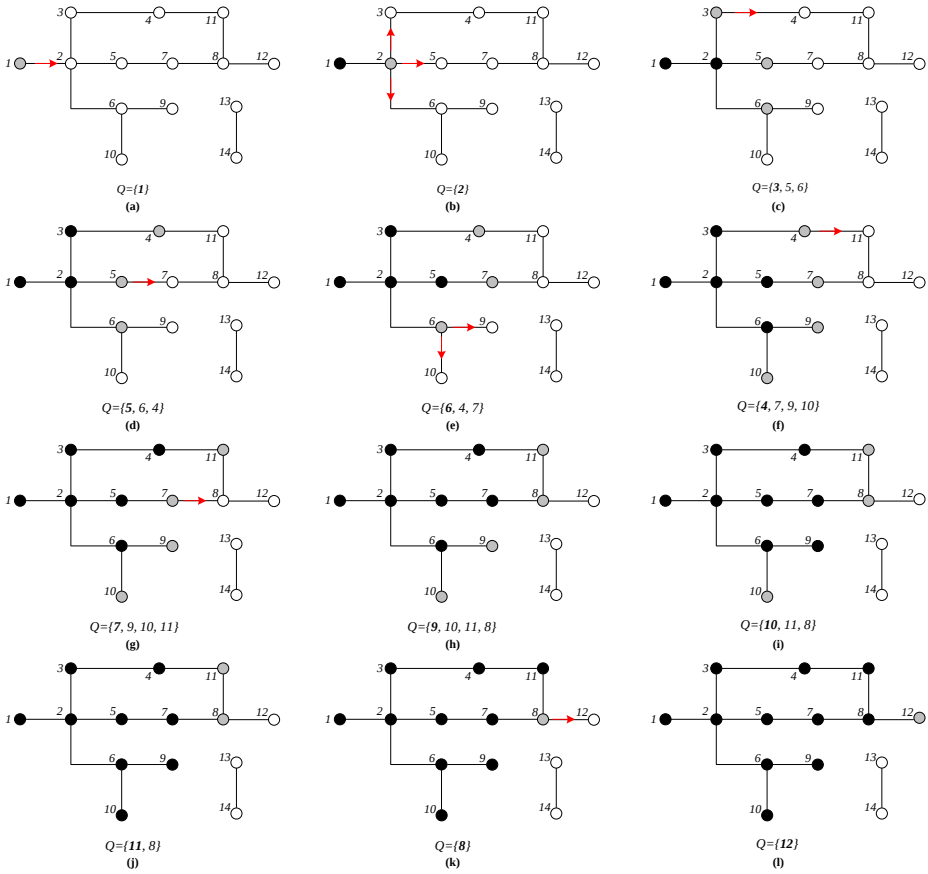

Fig. 3.3. Progress of the breadth-first search algorithm on a 14-node graph

Now, bus numbering technique can be integrated into the breadth-first search algorithm. In [3.21], a three-index scheme that assigns *lateral level* (*l*), *lateral index* (*m*), *bus index* (*n*) to each bus is systematically introduced in (*l*,*m*,*n*) order and the same scheme is also used in this dissertation. The main idea behind the bus numbering technique is that buses located on the same lateral will be identified with the same lateral level *l*, buses on the next coming sub-laterals will have level of *l+1* and so on. If multiple sub-laterals within the same level exist in the network (typical condition in distribution networks), then buses on the same level of sub-laterals can be uniquely identified by lateral index *m*. Lastly, the third index of *n* refers to n^{th} bus on the lateral (*l*,*m*). Number of lateral levels, number of laterals on the level *l* and number of buses on

lateral *(l,m)* are kept recorded in three counters *L*, *M(l)* and *N(l,m)*, respectively during the breadth-first search progress. Resulting bus numbering technique on the modified tree structure as derived previously is exemplified in Fig 3.5. Two MV/LV transformers, one voltage regulator and single-phase branches are added to the available tree structure given in Fig. 3.4 to reflect a MV main feeder and its associated LV distribution networks in a simple graph.

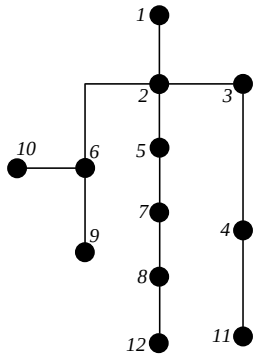

Fig. 3.4. Resulting tree structure after breadth-first search method

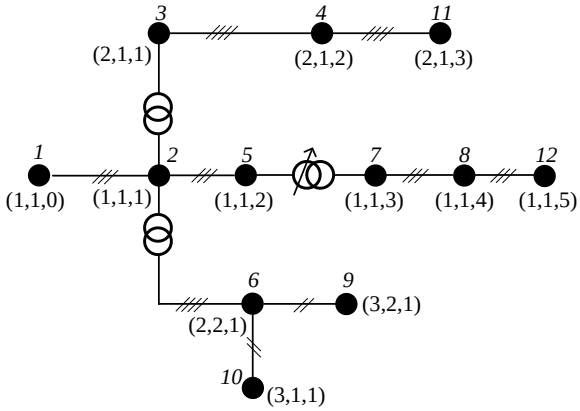

Fig. 3.5. An example of bus numbering on the modified tree structure

Ordered list of buses or laterals can be easily built to process backward and forward sweep systematically once their ordered triple indexes are established. All individual ordered triples are inserted into an empty matrix row-by-row and the rows of resulting

matrix are sorted in descending order with respect to level *l*, lateral index *m* and bus index *n*. Regarding of the modified tree structure example in Fig. 3.5, sorted buses in descending order can be presented as follows:

$$\underbrace{\{9,10,6,11,4,3,12,8,}_{\overrightarrow{backward}}\underbrace{7,5,2,1\}}_{\overleftarrow{forward}}$$

Pseudo code of bus numbering technique:

```
1       for each node u ∈ G-{s}
2               state(u) ← 1 (untouched)            % all nodes except s are in state 1,
3       end
4       state(s) ← 2 (in queue or gray)             % the root node s is in queue,
5       Q = []                                      % initialize an empty Q,
6       ENQUEUE(Q,s)                                % enqueue s onto Q,
7       while Q is non-empty
8           u ← DEQUEUE(Q)                          % u is the head element of Q,

            % Connected-components structure routine()
9               Lines between 9-20 of the previous pseudo code here

            % Bus numbering routine() proposed by R. Zimmerman [3.8]
10          if u is the root node
11              (l,m,n) ← (1,1,0) and (L,M(l),N(1,1)) ← (1,1,0)
12          else
13              bus(u).l ← bus(bus(u).parent).l     % u's level equals to its parent
                                                    % bus's level,
14              if bus(bus(u).parent).next == u     % if u lies on the same lateral as
                                                    % its parent,
15                  m ← bus(bus(u).parent).m        % m equals to lateral index of m's
                                                    % parent bus,
16              else                                % u is on a new sub-lateral,
17                  l ← l+1                         % increase the lateral level,
18                  if l > L                        % if l is first time encountered,
19                      L ← L+1                     % increase level counter L by one,
20                      M(l) ← 0                    % initialize the counter M for the
                                                    % new sub-lateral,
21                  end
22                  M(l) ← M(l)+1                   % increase counter M by 1,
23                  m ← M(l)                        % set m to counter M,
```

```
24                  N(l,m) ← 0                          % initialize counter N,
25              end
26              N(l,m) ← N(l,m)+1                       % increase counter N by 1,
27              n ← N(l,m)                              % set n to counter N,
28          end
29          bus(u).l ← l and bus(u).m ← m and bus(u).n ← n
29      end
```

Instead of using sorted buses, sorted laterals in descending order with respect to lateral's *l* and *m* is more convenient for both backward and forward sweep steps. In this case, another matrix which is composed of rows of lateral (*l, m*) is built and sorted in descending order with respect to *l* and *m*. Also, two additional columns are introduced to represent the start and end buses of every lateral (*l,m*). Finally, combining sorted laterals with bus data structures as given before in Table 3.1 will complete the first stage of the BFS method. Final stage concerns three-phase modelling of network components.

3.4 Modelling of Distribution Network Components

3.4.1 Three-phase untransposed distribution line/cable model

Unsymmetrical spacing between phase conductors without transposition is the most common property of distribution lines. It is likely to see unequal voltage drops among the phases, even though power flow is balanced along a distribution line. For this reason, unbalanced three-phase load flow solution will require accurate modelling of distribution lines for the steady-state voltage analysis. Additionally, in reality, loads and distributed generators are usually connected between line and neutral terminals for 3-phase 4-wire systems. However, most of the distribution network analysis disregards the phase to neutral voltages so that voltage unbalance is miscalculated. Therefore, neutral-to-earth voltage (NEV) at each node could be estimated here for multi-grounded neutral system. In case of unbalanced load flow condition, the return current will be divided into neutral and earth circuit. Share amount of return currents among neutral and earth circuit mainly depends on the neutral conductor and grounding electrode impedances. On account of this, unlike Kersting's phase impedance matrix

[3.26], neutral conductors can be explicitly represented here in the series impedance of lines/cables.

Since the equivalent shunt impedance of lines/cables (e.g. line charging capacitor) has negligible impact on voltage drop in distribution networks, only series impedances will be considered here.

Carson's line equations have been used to generate a series impedance matrix for the given line/cable configuration in this dissertation (*Appendix B*). Figure 3.6 illustrates typical 3-phase 4-wire overhead line and its equivalent circuit. Voltage drop along a line lateral based on the primitive impedance matrix (B.12) derived in Appendix B can be calculated as:

$$\begin{bmatrix} V_a(i) \\ V_b(i) \\ V_c(i) \\ V_n(i) \end{bmatrix} = \begin{bmatrix} V_a(i-1) \\ V_b(i-1) \\ V_c(i-1) \\ V_n(i-1) \end{bmatrix} - \underbrace{\begin{bmatrix} z_{aa} & z_{ab} & z_{ac} & z_{an} \\ z_{ba} & z_{bb} & z_{bc} & z_{bn} \\ z_{ca} & z_{cb} & z_{cc} & z_{cn} \\ z_{na} & z_{nb} & z_{nc} & z_{nn} \end{bmatrix}}_{Z_{line}} \cdot \begin{bmatrix} J_a(i) \\ J_b(i) \\ J_c(i) \\ -J_n(i) \end{bmatrix} \tag{3.8}$$

where

$V_{a,b,c,n}(i)$ are the phase and neutral voltages of the i^{th} node as referenced to their own local earth,

$J_{a,b,c,n}(i)$ are the incoming branch phase and neutral currents of the i^{th} node.

In order to solve voltage drop in (3.8), phase and neutral branch currents have to be determined accurately during backward sweep. The computation of phase branch currents J_a, J_b, J_c is unique and straightforward while the neutral branch current J_n can be computed in different ways. As already reported in [3.35], once the neutral voltages are calculated in the previous iteration, then earth leakage currents are obtained by knowing grounding electrode impedance Z_{gr} (Fig. 3.8):

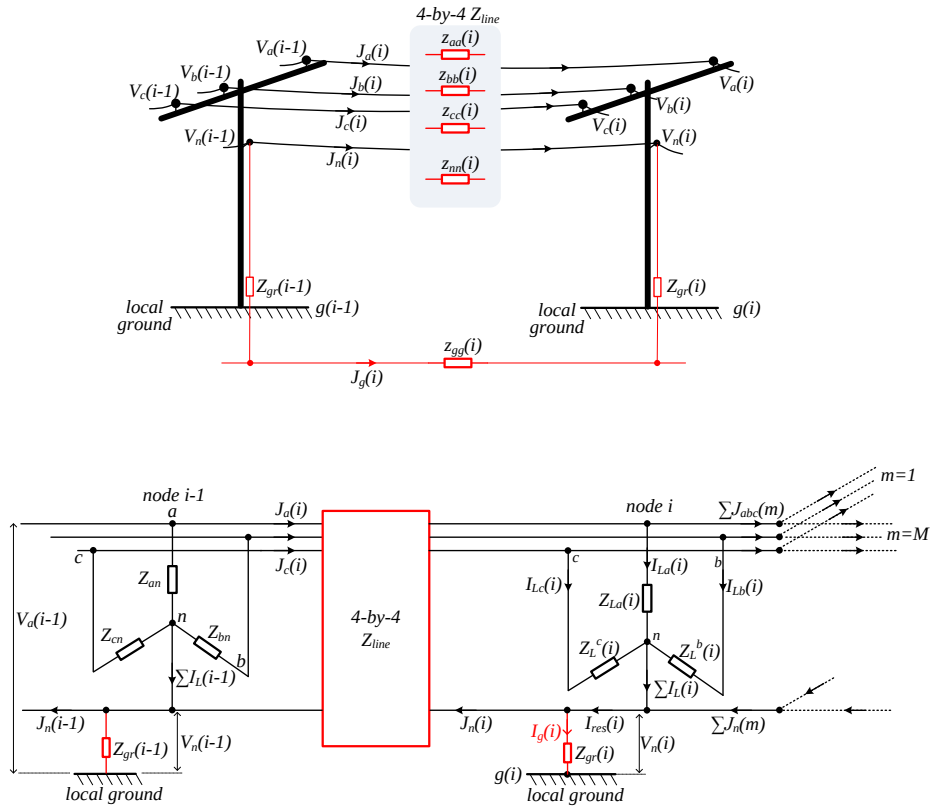

Fig. 3.6. Typical 3-phase 4-wire overhead line segment (top), and its generalized circuit representation (bottom).

$$I_g(i) = \frac{V_n(i)}{Z_{gr}(i)} \tag{3.9}$$

Neutral branch current is then found by summation of the earth leakage current I_g and the residual current I_{res}.

$$J_n(i) = I_g(i) + I_{res}(i) \tag{3.10}$$

But this method of neutral current computation in (3.9) and (3.10) tends to cause convergence problem with the load flow algorithm due to not having strong constraints. Therefore, an improved neutral current determination as adopted in [3.35] will be used

here. Accordingly, apart from (3.9) and (3.10), an additional constraint is introduced by KCL and KVL for the neutral-ground circuit as depicted in Fig. 3.7. The additional constraint is defined by the last row of (3.8) resulted from KVL:

$$\begin{aligned} V_n(i-1)-V_n(i) &= \begin{bmatrix} z_{an} & z_{bn} & z_{cn} \end{bmatrix} \cdot \begin{bmatrix} J_a \\ J_b \\ J_c \end{bmatrix} + z_{nn} \cdot J_n \\ &= \begin{bmatrix} z_{in} \end{bmatrix} \begin{bmatrix} J_{abc} \end{bmatrix} + z_{nn} \cdot J_n \end{aligned} \tag{3.11}$$

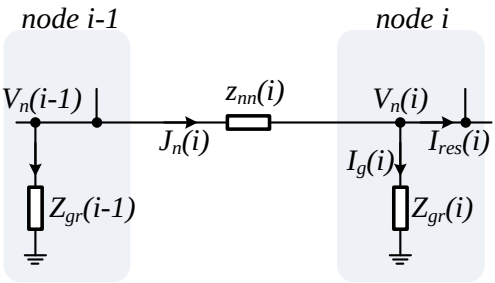

Fig. 3.7. Closer look on the neutral and grounding circuit. Current directions are matched with Carson's circuit

By combining (3.9)-(3.11), the branch neutral current is provided in terms of neutral voltage of parent node, grounding impedance of local node, incoming branch phase currents, and residual current that is calculated by summation of all sub-lateral currents. So, the branch neutral current becomes:

$$J_n(i) = \frac{V_n(i-1) - \left[z_{in}(i) \right] \cdot \left[J_{abc}(i) \right] + I_{res}(i) \cdot Z_{gr}(i)}{Z_{gr}(i) + z_{nn}(i)} \tag{3.12}$$

where I_{res} is the residual current and computed as:

$$I_{res}(i) = \sum_{k=\{a,b,c\}} I_{L,k}(i) + \sum_{k=\{a,b,c\}} I_{sh,k}(i) + \sum_{m \in M} J_n(m) \tag{3.13}$$

where

M is the set of sub-laterals that branch off the i^{th} node,

$I_L(i)$ and $I_{sh}(i)$ denote load and shunt capacitor currents in respectively, absorbed by the i^{th} node,

J_n is the branch neutral current.

Load currents in (3.13) are specified as depending on whether the load is constant power, constant current or constant impedance type. Equivalent current injections are firstly determined from these specified inputs, and then inserted to (3.13). So, determination of load currents will be summarized in the next subsection for various load types.

Grounding impedance Z_{gr} is usually distributed at certain distances on the poles. Resistivity of an electrode rod is approximated as [3.36]:

$$R_{gr} = \frac{\rho}{2\pi \cdot L}\left(\ln\frac{4 \cdot L}{r} - 1\right) \tag{3.14}$$

ρ is the soil resistivity in ohm.cm, L is length of the electrode rod in cm, and r is the radius in cm. For typical 3-m length and 15.88-mm diameter rod, the resistance R_{gr} becomes 26 Ω approximately. For this reason, if not specified, 25 Ω grounding impedance will be assigned to each pole in the simulation of example distribution networks by default. On the other hand, substation and household grounding impedances are usually designed smaller compared to pole's grounding impedance due to the requirement of limited NEV during phase-earth faults so that substation transformers are assumed to be solidly grounded in this work.

The phase currents along the branch are also determined as given in (3.15) during backward sweep and finally, the required branch currents will be completed to compute voltage drops in (3.8) preparing for forward sweep.

$$\begin{bmatrix} J_a(i) \\ J_b(i) \\ J_c(i) \end{bmatrix} = \begin{bmatrix} I_{L,a}(i) + I_{sh,a}(i) \\ I_{L,b}(i) + I_{sh,b}(i) \\ I_{L,c}(i) + I_{sh,c}(i) \end{bmatrix} - \begin{bmatrix} \left(\dfrac{S_{gen,a}}{V_a(i) - V_n(i)} \right)^* \\ \left(\dfrac{S_{gen,b}}{V_b(i) - V_n(i)} \right)^* \\ \left(\dfrac{S_{gen,c}}{V_c(i) - V_n(i)} \right)^* \end{bmatrix} + \begin{bmatrix} \sum_{m \in M} J_a(m) \\ \sum_{m \in M} J_b(m) \\ \sum_{m \in M} J_c(m) \end{bmatrix} \tag{3.15}$$

$S_{gen}(i)$ is the apparent power of *constant PQ* generator connected at i^{th} node.

In order to evaluate the effects of line impedance on steady-state phase voltage variations, realistic distribution line models should be exploited in a load flow study. Cable types and physical layouts are required information to define a complete line section. Realistic benchmark models basically developed for distribution networks in [3.28]-[3.29], [3.31] have been also used here as reference. Thus, five different reference line layouts are generated as illustrated in Fig. 3.8 and given in Table 3.2 where d_c denotes conductor diameter in the figure. Layouts of *ID 1*, *ID 2* and *ID 3* are suitable for 0.4-kV LV distribution networks whereas *ID 2*, *ID 4* and *ID 5* will be used on 10-20-kV networks. Table A1 and Table A2 in Appendix *A* summarize typical properties of LV and MV cables mostly used in European countries by extending [3.29] and by modifying a cable manufacturer's datasheet [3.30]. Other reference layouts of overhead lines which are typically used in U.S. are shown in Fig. 3.9 based on [3.32]. For example, 1/0 aluminium conductor steel reinforced (ACSR) for both 3 phases and a neutral conductor as shown in Fig. 3.8 within the 'B-A-C-N' phase order will thus result in two different series impedance matrices either in the 4-by-4 primitive impedance matrix form as presented previously or in the 3-by-3 reduced phase impedance matrix form using Kron's reduction [3.26] for *f=60 Hz*, $\rho = 100\ \Omega \cdot m$ and *2580-ft* (786.3 meters) length:

$$z_{prim} = \begin{bmatrix} 0.5205 + j0.7373 & 0.0466 + j0.4162 & 0.0466 + j0.3814 & 0.0466 + j0.3845 \\ 0.0466 + j0.4162 & 0.5205 + j0.7373 & 0.0466 + j0.3555 & 0.0466 + j0.3680 \\ 0.0466 + j0.3814 & 0.0466 + j0.3555 & 0.5205 + j0.7373 & 0.0466 + j0.3753 \\ 0.0466 + j0.3845 & 0.0466 + j0.3680 & 0.0466 + j0.3753 & 0.5205 + j0.7373 \end{bmatrix} \Omega \quad (3.16)$$

$$z_{abc} = \begin{bmatrix} 0.5812 + j0.5825 & 0.1039 + j0.2676 & 0.1054 + j0.2302 \\ 0.1039 + j0.2676 & 0.5747 + j0.5947 & 0.1021 + j0.2103 \\ 0.1054 + j0.2302 & 0.1021 + j0.2103 & 0.5775 + j0.5894 \end{bmatrix} \Omega \quad (3.17)$$

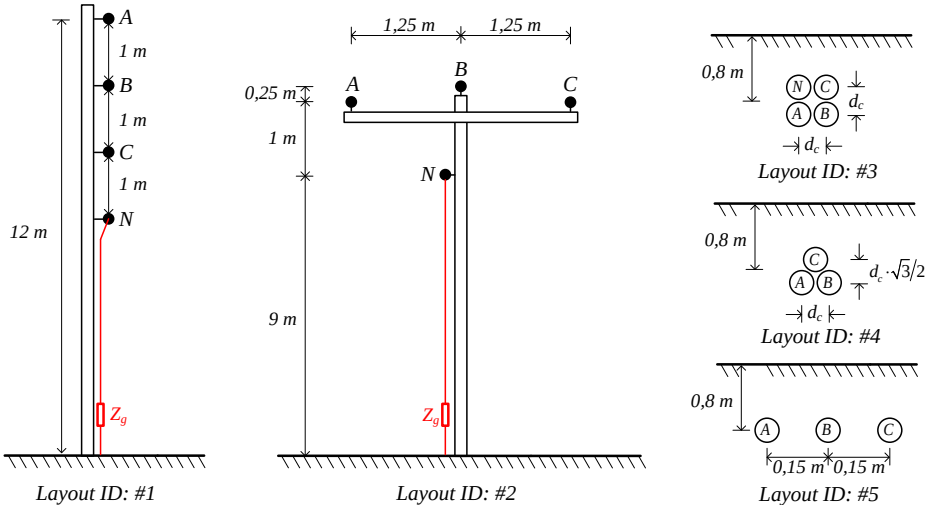

Fig. 3.8. Typical overhead and underground layouts of distribution line/cables mostly used in Europe

Table. 3.2. Typical layouts generated for MV and LV distribution networks associated with Fig. 3.8

Layout ID	Type
1	4-wire pole for LV overhead lines
2	4-wire pole for MV overhead lines
3	4-wire LV underground
4	3-wire MV underground as trefoil laid
5	3-wire MV underground as laid direct

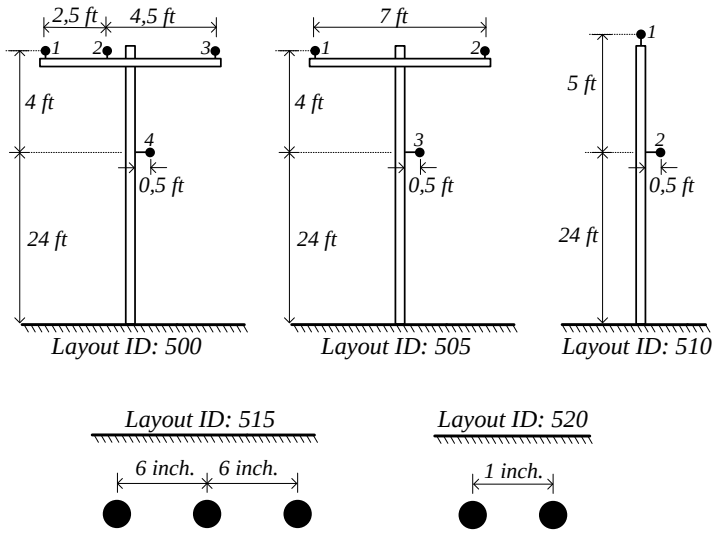

Fig. 3.9. Some pole layouts used for overhead lines and underground cables in IEEE distribution test feeders [3.32]

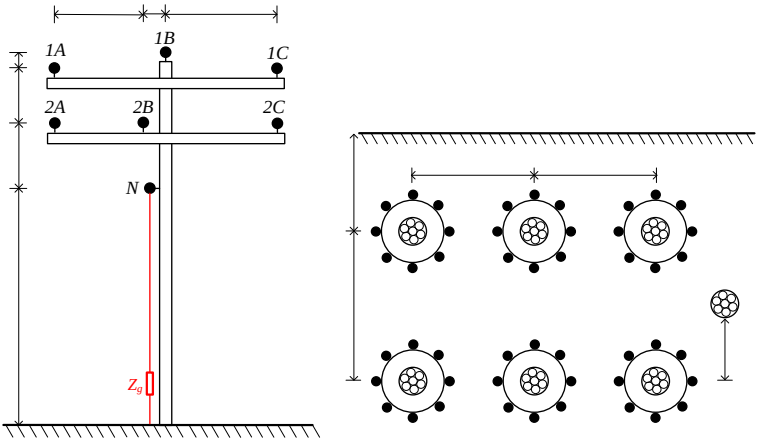

Fig. 3.10. Example of double-circuit pole layouts for overhead lines (left) and underground concentrated neutral cables (right) based on [3.28], [3.31]

It is a common practise that multiple outgoing feeders from the transformer may be carried on the same pole with a shared neutral for a certain distance (Fig. 3.10). In this case, mutual couplings among multiple circuits have to be considered and the series

impedance of double- or multi-circuits can be determined in the same way with higher number of conductors this time.

3.4.2 Generalized load model

Compared to transmission networks, various balanced and unbalanced load types exist in distribution networks according to number of load phases (single- or three-phase) and connection types (delta or star). Moreover, in the sense of electricity consumption characteristics, constant power, constant current, constant admittance or any combination must be performed for the realistic load models. If a measured load profile is available at certain time intervals, then the class of constant power can be preferred load type by assigning the measured real and reactive power as scheduled power. For some cases, only load density along a line is specified in terms of *kVA/km* and usually assumed to be uniformly distributed for the simplicity. In accordance with this, loads can be further classified into *spot* and *uniformly distributed* loads, however in this chapter, only spot loads will be considered and uniformly distributed loads will be approximated by the spot loads. Fig 3.11 illustrates wye- and delta-connected spot loads while Table 3.3 summarizes model equations where I^k, V^k represent load phase currents and voltages at k^{th} iteration, respectively.

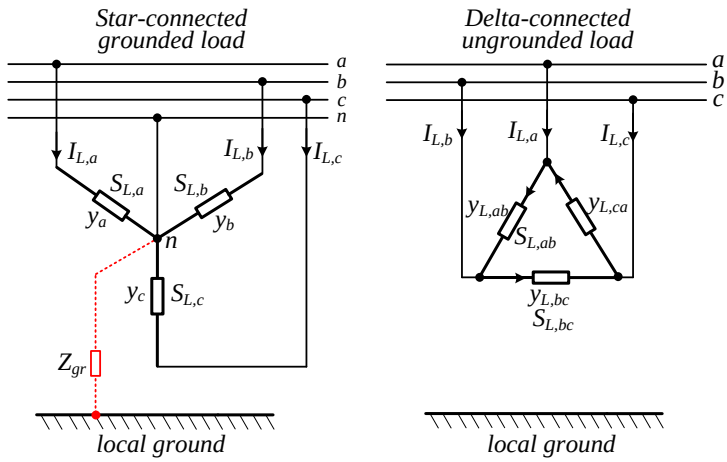

Fig. 3.11. Wye (left) and delta-connected (right) spot loads

Table. 3.3. Spot load model equations

	Constant Complex Power	*Constant Current*	*Constant Admittance (impedance)*
Grounded wye-connected load	$\begin{bmatrix} I_{L,a}^{k} \\ I_{L,b}^{k} \\ I_{L,c}^{k} \end{bmatrix} = \begin{bmatrix} \left(\frac{S_{L,a}}{V_a^{k-1} - V_n^{k-1}} \right)^* \\ \left(\frac{S_{L,b}}{V_b^{k-1} - V_n^{k-1}} \right)^* \\ \left(\frac{S_{L,c}}{V_c^{k-1} - V_n^{k-1}} \right)^* \end{bmatrix}$	$\begin{bmatrix} I_{L,a}^{k} \\ I_{L,b}^{k} \\ I_{L,c}^{k} \end{bmatrix} = \begin{bmatrix} I_{L,a}^{nom} \\ I_{L,b}^{nom} \\ I_{L,c}^{nom} \end{bmatrix}$	$\begin{bmatrix} I_{L,a}^{k} \\ I_{L,b}^{k} \\ I_{L,c}^{k} \end{bmatrix} = \begin{bmatrix} y_{L,a}^{nom} \cdot V_a^{k-1} \\ y_{L,b}^{nom} \cdot V_b^{k-1} \\ y_{L,c}^{nom} \cdot V_c^{k-1} \end{bmatrix}$
Delta-connected load	$\begin{bmatrix} I_{L,a}^{k} \\ I_{L,b}^{k} \\ I_{L,c}^{k} \end{bmatrix} = T \cdot \begin{bmatrix} \left(\frac{S_{L,ab}}{V_a^{k-1} - V_b^{k-1}} \right)^* \\ \left(\frac{S_{L,bc}}{V_b^{k-1} - V_c^{k-1}} \right)^* \\ \left(\frac{S_{L,ca}}{V_c^{k-1} - V_a^{k-1}} \right)^* \end{bmatrix}$	$\begin{bmatrix} I_{L,a}^{k} \\ I_{L,b}^{k} \\ I_{L,c}^{k} \end{bmatrix} = T \cdot \begin{bmatrix} I_{L,ab}^{nom} \\ I_{L,bc}^{nom} \\ I_{L,ca}^{nom} \end{bmatrix}$	$\begin{bmatrix} I_{L,a}^{k} \\ I_{L,b}^{k} \\ I_{L,c}^{k} \end{bmatrix} = T \cdot \begin{bmatrix} y_{L,ab}^{nom} \cdot \left(V_a^{k-1} - V_b^{k-1} \right) \\ y_{L,bc}^{nom} \cdot \left(V_b^{k-1} - V_c^{k-1} \right) \\ y_{L,ca}^{nom} \cdot \left(V_c^{k-1} - V_a^{k-1} \right) \end{bmatrix}$

From the specified rated power (S_L) and rated voltage levels (V^{rated}) of loads, the nominal current (I^{nom}) and nominal admittance (y^{nom}) values per phase are determined as:

$$I_{L,a}^{nom} = \left(\frac{S_{L,a}}{V_a^{rated}} \right)^*, \quad y_{L,a}^{nom} = \frac{\left(S_{L,a} \right)^*}{\left| V_a^{rated} \right|^2} \rightarrow \text{ for grounded wye-connected loads}$$
$$I_{L,ab}^{nom} = \left(\frac{S_{L,ab}}{V_a^{rated} - V_b^{rated}} \right)^*, \quad y_{L,ab}^{nom} = \frac{\left(S_{L,ab} \right)^*}{\left| V_a^{rated} - V_b^{rated} \right|^2} \rightarrow \text{ for delta-connected loads} \tag{3.18}$$

Matrix T used in Table 3.3 maps the phase currents into line currents which are eventually necessary to compute branch currents. By applying KCL in Fig. 3.11 for delta connection in such a way that three current equations are exploited (e.g., $I_{L,a}=I_{L,ab} - I_{L,ca}$), the transformation matrix is then obtained as:

$$T = \begin{bmatrix} 1 & 0 & -1 \\ -1 & 1 & 0 \\ 0 & -1 & 1 \end{bmatrix} \tag{3.19}$$

Without loss of generality, generator models considered here will be equivalent to negative constant power loads. Since most of the generators connected to MV and LV distribution networks operate in constant power mode, development of PV-type generators which regulate their terminal voltage will be studied in future for the load flow analysis.

3.4.3 Shunt capacitor model

Shunt capacitors are located on the distribution networks in order to help regulating voltage levels and compensate reactive power demand. From the modelling point of view, their implementation in load flow simulation is similar to the constant admittance load model. Thus, for the given rated reactive power and rated voltage, current injections can be calculated as:

$$\begin{bmatrix} y_{sh,a}^{nom} \\ y_{sh,b}^{nom} \\ y_{sh,c}^{nom} \end{bmatrix} = \begin{bmatrix} Q_{sh,a}^{rated} \Big/ \left|V_a^{rated}\right|^2 \\ Q_{sh,b}^{rated} \Big/ \left|V_b^{rated}\right|^2 \\ Q_{sh,c}^{rated} \Big/ \left|V_c^{rated}\right|^2 \end{bmatrix} \quad \text{and} \quad \begin{bmatrix} y_{sh,ab}^{nom} \\ y_{sh,bc}^{nom} \\ y_{sh,ca}^{nom} \end{bmatrix} = \begin{bmatrix} Q_{sh,ab}^{rated} \Big/ \left|V_{ab}^{rated}\right|^2 \\ Q_{sh,bc}^{rated} \Big/ \left|V_{bc}^{rated}\right|^2 \\ Q_{sh,ca}^{rated} \Big/ \left|V_{ca}^{rated}\right|^2 \end{bmatrix}$$ in siemens and current

injections of star- and delta-connected shunt capacitor banks become, in respectively:

$$\begin{bmatrix} I_{sh,a} \\ I_{sh,b} \\ I_{sh,c} \end{bmatrix} = \begin{bmatrix} j \cdot y_{sh,a}^{nom} \\ j \cdot y_{sh,b}^{nom} \\ j \cdot y_{sh,c}^{nom} \end{bmatrix} .* \begin{bmatrix} V_a \\ V_b \\ V_c \end{bmatrix} \text{ and } \begin{bmatrix} I_{sh,ab} \\ I_{sh,bc} \\ I_{sh,ca} \end{bmatrix} = \begin{bmatrix} j \cdot y_{sh,ab}^{nom} \\ j \cdot y_{sh,bc}^{nom} \\ j \cdot y_{sh,ca}^{nom} \end{bmatrix} .* \begin{bmatrix} V_{ab} \\ V_{bc} \\ V_{ca} \end{bmatrix}$$

3.4.4 Three-phase two-winding transformer model

Regarding of European distribution networks, 20-kV or 10-kV MV distribution networks are commonly engaged to 60-kV or 110-kV sub-transmission networks through the substations that usually contain delta-delta (*D-D*) connection type of transformers with on-load tap changers. On the other hand, 400-V 3-phase 4-wire secondary distribution feeders branch off MV feeders along delta - grounded wye (*D-Yg*) transformers with off-load tap changers.

Modelling of three-phase distribution transformers in phase coordinates requires more attention due to having possibility of ill-conditioned matrices for certain type of transformers. Basically, two modelling approaches exist in the literature. Direct approach is based on application of Kirchoff's voltage and current loops for both primary and secondary circuit of the transformer [3.31]. This transformer modelling approach is developed only for *BFS* load flow algorithm. The other method generates nodal admittance matrices that represent 3-phase transformer configurations [3.37]-[3.40]. The operability of nodal admittance matrix-based modelling approach is more extensive and it is able to support any load flow algorithm. However, matrix singularity problem of some transformer configurations leads to limited implementation of nodal admittance matrix approach.

In this work, nodal admittance matrix-based transformer modelling tailored for *BFS* load flow algorithm has been developed. Matrix singularity problem is stressed and then fixed by means of introducing additional constraints on the node admittance matrix of transformer. Modelling of *D-Yg* and *D-D* connection types of step-down transformers will be presented here and the same modelling methodology can be further applied to the other connection types of two-winding transformers.

It will be assumed that the secondary side line-to-line voltages are lagging the primary side line-to-line voltages by 30º which represents the prevalent class of transformers (*D-Yg1*) in Europe. In this respect, secondary side terminal currents will be also lagging the primary side terminal currents by 30º. As another assumption, magnetizing impedance of the transformer is sufficiently high to be neglected as compared to leakage impedance. Furthermore, each primary-secondary phase windings are assumed to be formed by separate and identical single-phase transformers (this is why it is also called as 3-phase transformer bank). This makes cross couplings between the primary and secondary windings zero (e.g. primary *phase a* to secondary *phase b*) and simplifies mathematical modelling of the transformers with tolerable errors. Additionally, mutual admittance (m) between each phase will be assumed to equal to winding leakage admittances ($y=m$).

As a first step of computation of node admittance matrix, primitive admittance matrix (Y_{prim}) that represents relationship between phase voltages and currents at primary and secondary circuits is formed as given in (3.20). Then, connection matrices (C and D) transforms the phase quantities into the node quantities, thus, the resulted node voltages and currents can be directly used in load flow solution.

$$I_{ph} = Y_{prim} \cdot V_{ph} \tag{3.20}$$

$$V_{ph} = C \cdot V_{node} \tag{3.21}$$

$$I_{node} = D \cdot I_{ph} \tag{3.22}$$

When (3.21) and (3.22) are inserted into (3.20), transformer node admittance matrix becomes as:

$$\underbrace{C^T \cdot I_{ph}}_{I_{node}} = \underbrace{D \cdot Y_{prim} \cdot C}_{Y_{node}} \cdot V_{node} \tag{3.23}$$

Each transformer configuration will have its own primitive admittance and connection matrices. For this reason, it will be necessary to store the resulting node admittance matrices for various transformer configurations in load flow solution tool.

"D-Yg1 transformer":

30º phase shift of voltage and current between primary-secondary circuits is realized by proper connection of single-phase transformers. Fig. 3.12 shows the transformer equivalent circuit and its related current phasors. Thus, primitive admittance matrix of *D-Yg1* transformer can be written as following:

$$\begin{bmatrix} i_{CA} \\ i_{AB} \\ i_{BC} \\ \hline i_{as} \\ i_{bs} \\ i_{cs} \\ \hline i_{ns} \end{bmatrix} = \underbrace{\left[\begin{array}{ccc|ccc|c} y & & & -m & & & 0 \\ & y & & & -m & & 0 \\ & & y & & & -m & 0 \\ \hline -m & & & y & & & 0 \\ & -m & & & y & & 0 \\ & & -m & & & y & 0 \\ \hline 0 & 0 & 0 & 0 & 0 & 0 & y_{ns} \end{array}\right]}_{Y_{prim}} \begin{bmatrix} V_{CA} \\ V_{AB} \\ V_{BC} \\ \hline V_{an} \\ V_{bn} \\ V_{cn} \\ \hline V_{ns} \end{bmatrix} \tag{3.24}$$

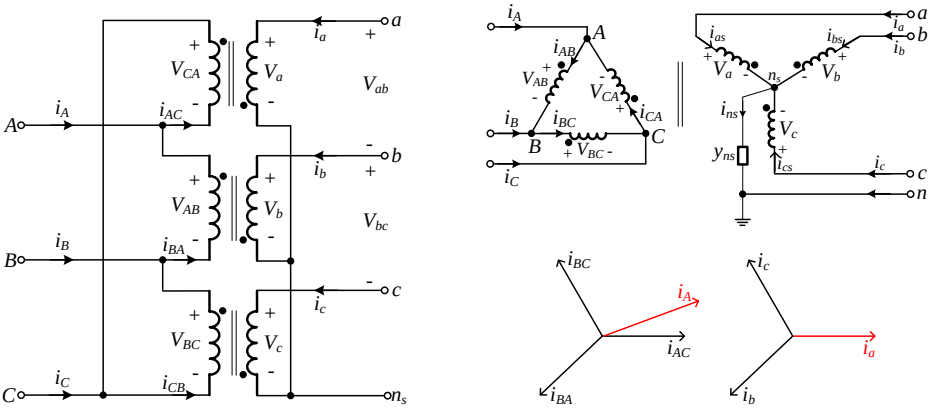

Fig. 3.12. *D-Yg1* transformer bank connection and its positive-sequence current phasor diagram based on [3.31]

where subscripts in big letters denote primary side phase quantities and subscripts in small letters represent the quantities in secondary circuit. y_{ns} refers neutral grounding admittance. Accordingly, the connection matrix *C* and *D* are:

$$\begin{bmatrix} V_{CA} \\ V_{AB} \\ V_{BC} \\ \hline V_{an} \\ V_{bn} \\ V_{cn} \\ \hline V_{ng} \end{bmatrix} = \underbrace{\left[\begin{array}{ccc|ccc|c} 0 & 0 & 1 & & & & 0 \\ 1 & 0 & 0 & & 0 & & 0 \\ 0 & 1 & 0 & & & & 0 \\ \hline & & & -1 & & & 1 \\ & 0 & & & -1 & & 1 \\ & & & & & -1 & 1 \\ \hline 0 & 0 & 0 & 0 & 0 & 0 & 1 \end{array}\right]}_{C} \begin{bmatrix} V_{AB} \\ V_{BC} \\ V_{CA} \\ \hline V_{ag} \\ V_{bg} \\ V_{cg} \\ \hline V_{ng} \end{bmatrix} \tag{3.25}$$

$$\begin{bmatrix} i_A \\ i_B \\ i_C \\ \hline i_a \\ i_b \\ i_c \\ \hline i_n \end{bmatrix} = \underbrace{\left[\begin{array}{ccc|ccc|c} -1 & 1 & 0 & & & & 0 \\ 0 & -1 & 1 & & 0 & & 0 \\ 1 & 0 & -1 & & & & 0 \\ \hline & & & 1 & & & 0 \\ & 0 & & & 1 & & 0 \\ & & & & & 1 & 0 \\ \hline & 0 & & -1 & -1 & -1 & 1 \end{array}\right]}_{D} \begin{bmatrix} i_{CA} \\ i_{AB} \\ i_{BC} \\ \hline i_{as} \\ i_{bs} \\ i_{cs} \\ \hline i_{ns} \end{bmatrix} \tag{3.26}$$

and, 7-by-7 node admittance matrix becomes:

$$Y_{node} = \left[\begin{array}{ccc|ccc|c} y & 0 & -y & -y & y & 0 & 0 \\ -y & y & 0 & 0 & -y & y & 0 \\ 0 & -y & y & y & 0 & -y & 0 \\ \hline 0 & 0 & -y & -y & & & y \\ -y & 0 & 0 & & -y & & y \\ 0 & -y & 0 & & & -y & y \\ \hline y & y & y & y & y & y & y_{ns} - 3y \end{array}\right] = \left[\begin{array}{c|c|c} Y_{pp} & Y_{ps} & Y_{pn} \\ \hline Y_{sp} & Y_{ss} & Y_{sn} \\ \hline Y_{np} & Y_{ns} & Y_{nn} \end{array}\right] \tag{3.27}$$

It should be noticed that delta side terminal voltages are represented as line-to-line voltage while wye side terminal voltages are given in terms of line-to-ground voltages. Further reduction can be applied on (3.27) since current entering into the internal neutral node (n_s) is only supplied by the internal sum of phase currents and there is no

external current injection to the internal neutral node. Therefore, last row of Y_{node} matrix can be revised as:

$$\left[\begin{array}{c} \\ \hline i_n = 0 \end{array}\right] = \left[\begin{array}{c|c|c} & & \\ \hline Y_{np} & Y_{ns} & Y_{nn} \end{array}\right] \left[\begin{array}{c} V_p \\ \hline V_s \\ \hline V_n \end{array}\right] \tag{3.28}$$

$$V_n = -Y_{nn}^{-1}\left(Y_{np}V_p - Y_{ns}V_s\right) \tag{3.29}$$

V_p denotes the primary 3-phase line-to-line voltages as $\left[V_{AB} \quad V_{BC} \quad V_{CA}\right]^T$ and V_s is the secondary 3-phase line-to-ground voltages $\left[V_{ag} \quad V_{bg} \quad V_{cg}\right]^T$. If (3.29) is inserted to the top row of Y_{node} for primary current in (3.27):

$$\begin{aligned} I_p &= Y_{pp}V_p + Y_{ps}V_s + Y_{pn}V_n \\ &= \underbrace{\left(Y_{pp} - Y_{pn}Y_{nn}^{-1}Y_{np}\right)}_{Y11}\cdot V_p + \underbrace{\left(Y_{ps} - Y_{pn}Y_{nn}^{-1}Y_{ns}\right)}_{Y12}\cdot V_s \end{aligned} \tag{3.30}$$

and if the same is applied to the secondary currents as well, then generalized 6-by-6 reduced node admittance matrix can be provided in partitioned form as:

$$\begin{aligned} Y_{node} = \left[\begin{array}{c|c} Y11 & Y12 \\ \hline Y21 & Y22 \end{array}\right] &= \left[\begin{array}{c|c} Y_{pp} - Y_{pn}Y_{nn}^{-1}Y_{np} & Y_{ps} - Y_{pn}Y_{nn}^{-1}Y_{ns} \\ \hline Y_{sp} - Y_{sn}Y_{nn}^{-1}Y_{np} & Y_{ss} - Y_{sn}Y_{nn}^{-1}Y_{ns} \end{array}\right] \\ &= \left[\begin{array}{ccc|ccc} y & 0 & -y & -y & y & 0 \\ -y & y & 0 & 0 & -y & y \\ 0 & -y & y & y & 0 & -y \\ \hline m & m & n & n & m & m \\ n & m & m & m & n & m \\ m & n & m & m & m & n \end{array}\right] \end{aligned} \tag{3.31}$$

where $m = \frac{y^2}{3y - y_{ns}}$ and $n = \frac{y^2}{3y - y_{ns}} - y$. For solidly grounded *D-Yg1* transformer ($y_{ns} \to \infty$), node admittance matrix becomes:

$$\lim_{y_{ns}\to\infty} Y_{node} = \left[\begin{array}{ccc|ccc} y & 0 & -y & -y & y & 0 \\ -y & y & 0 & 0 & -y & y \\ 0 & -y & y & y & 0 & -y \\ \hline 0 & 0 & -y & -y & & \\ -y & 0 & 0 & & -y & \\ 0 & -y & 0 & & & -y \end{array}\right] = \left[\begin{array}{c|c} \bar{Y}_{pp} & \bar{Y}_{ps} \\ \hline \bar{Y}_{sp} & \bar{Y}_{ss} \end{array}\right] \tag{3.32}$$

Concerning the *V-I-BFS* load flow algorithm, phase currents at primary side are computed in terms of secondary side currents and voltages during backward step. Similarly, secondary side terminal voltages are expressed in terms of the primary side voltages and currents during forward step. This is summarized in Table 3.4 based on (3.32).

Table. 3.4. Transformer model valid for all configurations: Current and voltage computation for *BFS* steps

Backward step	Forward step
Step 1. $V_p = \left(\bar{Y}_{sp}\right)^{-1} \cdot \left(I_s - \bar{Y}_{ss} V_s\right)$	Step 1. $V_s = \left(\bar{Y}_{ps}\right)^{-1} \cdot \left(I_p - \bar{Y}_{pp} V_p\right)$
Step 2. $I_p = \bar{Y}_{pp} \bar{V}_p + \bar{Y}_{ps} \bar{V}_s$	

However, it can be investigated from (3.32) that sub-matrices of $\bar{Y}_{pp}$ and $\bar{Y}_{ps}$ are not invertible and only two of the three equations in these sub-matrices are linearly independent. For this reason, additional constraints must be introduced in such a way that singularities of $\bar{Y}_{pp}^{-1}$ and $\bar{Y}_{ps}^{-1}$ are avoided.

The first constraint is introduced by non-existence of zero sequence voltage at delta side of the transformer so that the sum of primary side line-to-line voltages will be zero. The other constraint comes with a relationship between the currents and voltages at grounded-wye side of the transformer using (3.32). Thus, as referred to (3.32), if secondary currents are sum up:

$$\sum I_s = i_a + i_b + i_c = -y\left(V_{AB} + V_{BC} + V_{CA}\right) - y\left(V_{ag} + V_{bg} + V_{cg}\right) \tag{3.33}$$

then the forward step equation in Table 3.4 is updated by imposing (3.33) into the its third row as:

$$\underbrace{\begin{bmatrix} \cdots & \cdots & \cdots \\ y & y & y \end{bmatrix}}_{\bar{Y}_{ps}} \underbrace{\begin{bmatrix} V_{ag} \\ V_{bg} \\ V_{cg} \end{bmatrix}}_{V_s} = \underbrace{\begin{bmatrix} \cdots \\ -\sum i_s \end{bmatrix}}_{I_p} - \underbrace{\begin{bmatrix} \cdots & \cdots & \cdots \\ 0 & 0 & 0 \end{bmatrix}}_{\bar{Y}_{pp}} \cdot V_p \tag{3.34}$$

and new updated $\bar{Y}_{ps}$ becomes invertible matrix. On the other hand, regarding of the backward step $\bar{Y}_{sp}$ is already invertible so there is no need of introducing constraints for the backward sweep.

"D-D transformer":

D-D transformers located at MV substations with integrated on-load tap changers have the same configuration at both terminal sides therefore phase shift will not occur between primary and secondary windings if it is connected as in Fig. 3.13. Derivation of its node admittance matrix follows the same methodology of previous *D-Yg1* type transformers.

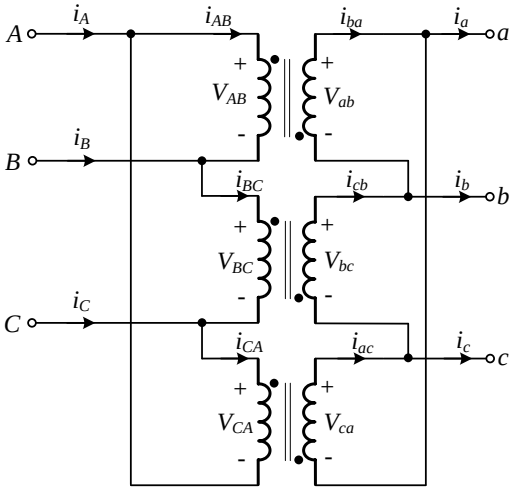

Fig. 3.13. *D-D* transformer bank composed of single-phase transformers

The primitive admittance matrix of a *D-D* transformer can be obtained by (3.35) based on Fig. 3.13:

$$\begin{bmatrix} i_{AB} \\ i_{BC} \\ i_{CA} \\ \hline i_{ab} \\ i_{bc} \\ i_{ca} \end{bmatrix} = \underbrace{\left[\begin{array}{ccc|ccc} y & & & -m & & \\ & y & & & -m & \\ & & y & & & -m \\ \hline -m & & & y & & \\ & -m & & & y & \\ & & -m & & & y \end{array}\right]}_{Y_{prim}} \begin{bmatrix} V_{AB} \\ V_{BC} \\ V_{CA} \\ \hline V_{ab} \\ V_{bc} \\ V_{ca} \end{bmatrix} \tag{3.35}$$

Connection matrices *C* and *D* are determined as:

$$C = \left[\begin{array}{ccc|ccc} 1 & & & & & \\ & 1 & & & 0 & \\ & & 1 & & & \\ \hline & & & 1 & & \\ 0 & & & & 1 & \\ & & & & & 1 \end{array}\right] \quad \text{and} \quad D = \left[\begin{array}{ccc|ccc} 1 & 0 & -1 & & & \\ -1 & 1 & 0 & & 0 & \\ 0 & -1 & 1 & & & \\ \hline & & & 1 & 0 & -1 \\ & 0 & & -1 & 1 & 0 \\ & & & 0 & -1 & 1 \end{array}\right] \tag{3.36}$$

and, eventually Y_{node} admittance matrix of *D-D* type transformer can be calculated by using (3.23):

$$\begin{bmatrix} i_A \\ i_B \\ i_C \\ \hline i_a \\ i_b \\ i_c \end{bmatrix} = \underbrace{\left[\begin{array}{ccc|ccc} y & 0 & -y & -y & 0 & y \\ -y & y & 0 & y & -y & 0 \\ 0 & -y & y & 0 & y & -y \\ \hline -y & 0 & y & y & 0 & -y \\ y & -y & 0 & -y & y & 0 \\ 0 & y & -y & 0 & -y & y \end{array}\right]}_{Y_{node}} \begin{bmatrix} V_{AB} \\ V_{BC} \\ V_{CA} \\ \hline V_{ab} \\ V_{bc} \\ V_{ca} \end{bmatrix} \tag{3.37}$$

$$\rightarrow \begin{bmatrix} i_p \\ \hline i_s \end{bmatrix} = \left[\begin{array}{c|c} \bar{Y}_{pp} & \bar{Y}_{ps} \\ \hline \bar{Y}_{sp} & \bar{Y}_{ss} \end{array}\right] \begin{bmatrix} V_p \\ \hline V_s \end{bmatrix}$$

All sub-matrices of Y_{node} are non-invertible and imposing additional constraints will be necessary in order to use Y_{node} for *BFS* algorithm. Since zero sequence voltages at both sides are zero, primary side voltages can be calculated as following:

$$\underbrace{\left[\begin{array}{ccc} 1 & 1 & 1 \end{array}\right]}_{\bar{Y}_{sp}} \underbrace{\begin{bmatrix} V_{AB} \\ V_{BC} \\ V_{CA} \end{bmatrix}}_{V_p} = \underbrace{\left[\begin{array}{c} 0 \end{array}\right]}_{I_s} - \underbrace{\left[\begin{array}{ccc} 0 & 0 & 0 \end{array}\right]}_{\bar{Y}_{ss}} \cdot V_s \tag{3.38}$$

Sum of the line-to-line voltages are also zero at secondary side, and $\bar{Y}_{ps}$ can be similarly updated as in (3.38) for the forward step.

Transformer rated power (S_{tr}), nominal voltages of the primary and secondary circuits (U_{HV}, U_{LV}), leakage impedance of windings in p.u. ($z=r+jx$), overall system base power (S_{base}) are required input data provided by user or operator to the load flow algorithm. So, leakage admittance of windings in p.u. (y) can be determined from the specified transformer data by (3.39).

$$y = \frac{1}{\left(r + j \cdot x\right)\frac{S_{base}}{S_{tr}}} \tag{3.39}$$

Y_{node} admittance matrices are formed in per unit value. For this reason, primary and secondary voltage-current quantities are first converted into per unit values. Once backward or forward step is completed for the transformer, then per unit values are converted back to real voltages and currents.

Additionally, off-load tap changing mechanism located at the high voltage side of MV/LV transformers can be simply modelled by scaling the nominal primary winding voltages up or down levels. Typical ranges of this tap mechanism varies between +5% and -5% of the nominal voltage. However, on-load tap changer utilized in HV/MV substations has more complex modelling details as opposed to off-load tap changers therefore it is expressed in the next subsection which presents operation and modelling of step-type voltage regulators.

In summary, modelling of two mostly used transformer configurations has been presented here but the modelling approach can be further implemented to the other configurations such as *Yg-Yg*, *Yg-D*, *Y-Y*. The sum of line-to-line voltages at ungrounded side and the relationship between currents and voltages at grounded side are two general constraints that can be applicable to any type of transformer configuration in order to prevent matrix singularity problem. The model validation is provided at the end of chapter.

3.4.5 Modelling of voltage regulators

Step-type voltage regulators (SVR) are extensively used at HV/MV substations and MV feeders together with other voltage supporting elements such as capacitor banks in order to continuously regulate three-phase voltages at predetermined locations. Nominal voltage ratings of SVRs are available from 6.6 kV to 33 kV levels and the preferred power ratings as given in [3.20] vary between 33-900 kVA for the single-

phase SVRs and 500-2500 kVA for the three-phase SVRs. In reality, two classes of SVR operation exist depending on the location of voltage regulation. If the objective is to regulate only local terminal bus voltage, then SVR or more conveniently load tap changer (LTC) will accommodate an autotransformer which typically has 32 taps spanning from -10% to +10% range of nominal voltage. Because of this, a single-tap operation will cause a 5/8-% or 0.00625-p.u. voltage change so that local terminal voltage can be adjusted to the set value within a certain bandwidth. In the case of voltage regulation of a remote point, additional compensator circuit that estimates the required amount of voltage correction along a line is employed in the autotransformer. This class of SVR operation is called as integrated load tap changer and line drop compensation (LTC+LDC) arrangement. It is also important to stress that sizing of a SVR is based on how much power will be transformed in the ±10-% voltage window. Since all the line current flows through the series winding of autotransformer, voltage drop or rise on the series winding will determine the required rated power of the SVR. Typically, the rated power of autotransformer is 10% of the rated line power [3.31].

As defined in IEEE C57.15-2009 standard [3.33], SVRs are designed in two different types of autotransformer construction: *Type A* and *Type B* (Fig. 3.14). In *Type A* step-type voltage regulator, the shunt winding is directly connected across the primary circuit and the series winding is connected to the secondary circuit (regulated circuit) via taps. In this situation, core excitation will not remain constant due to the fact that unregulated primary circuit will be appeared on the shunt winding. On the other hand, in *Type B* voltage regulators as shown in Fig. 3.14, the shunt winding is directly connected to the regulated secondary circuit thus the core excitation becomes constant. *Type B* is the most common used SVR in distribution networks. Since the shunt and series winding impedances are small enough, they will be ignored in the model [3.31]. Moreover, voltage regulation in “boost” or “buck” modes of SVR is achieved by means of reversing switch positioned at the terminal of the series winding.

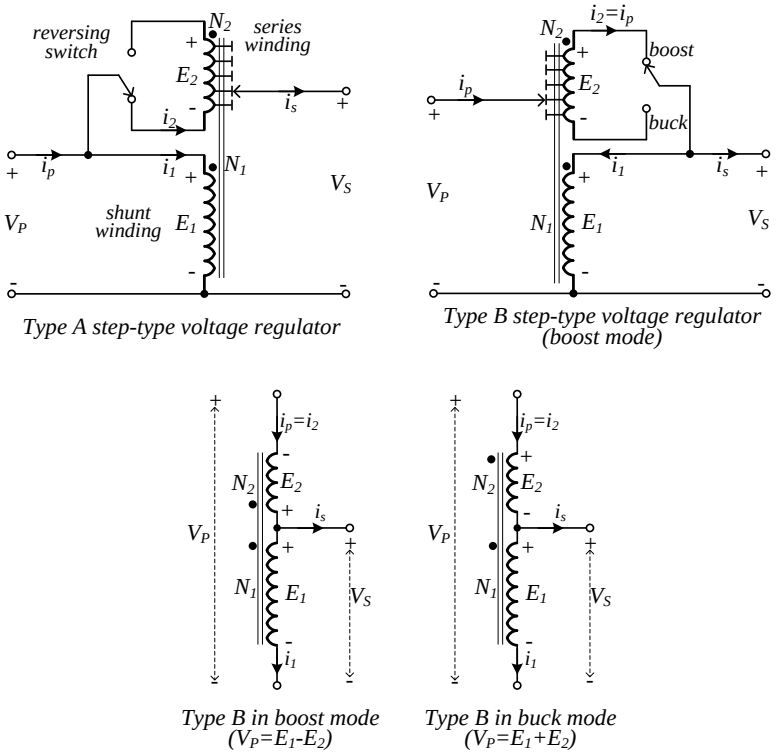

Fig. 3.14. Construction types of a load tap changer (LTC) acc. to IEEE C57.15-2009. Shunt and series winding impedances are neglected. Adapted from [3.31]

A LTC+LDC arrangement of single-phase SVR as depicted in Fig. 3.15 accommodates a control circuit for performing voltage regulation at a predetermined remote point. The main idea is to estimate the amount of voltage drop in terms of line current and effective line impedance and eventually correct the secondary terminal voltages via the taps. For doing this, the selected remote point is reflected into the smaller-scaled compensator circuit through the current and voltage measuring transformers. Four parameter settings as given below are necessary for the proper operation of LDC part [3.31], [3.34]:

1) *Voltage setting (V_{SET})*: This is the desired voltage level for the remote bus in p.u. or volt.

2) *Voltage bandwidth (BW)*: Bandwidth value introduces certain amount of tolerance to the V_{SET}. Accordingly, tap change is executed only when the measured voltage is less than V_{SET}-$BW/2$ or higher than V_{SET}+$BW/2$. Minimum recommended bandwidth setting is two times the volt per tap.
3) *Time delay (TD)*: Time delay introduces a waiting time right after the moment that measured voltage is detected outside of the tolerance. It prevents unwanted frequent tap change and provides coordination with other voltage supporting elements in the neighbourhood such as switched capacitor banks or distributed generators. Typical time delay for SVR is set in the range of 10-120 seconds.
4) *Compensation impedance settings in volt (R_{comp} and X_{comp})*: R_{comp} and X_{comp} represent the effective line impedance between the SVR and regulated remote point in volt. If any lateral branches off the feeder between the SVR and regulated remote point, then assigning accurate R_{comp} and X_{comp} set values becomes more complicated.

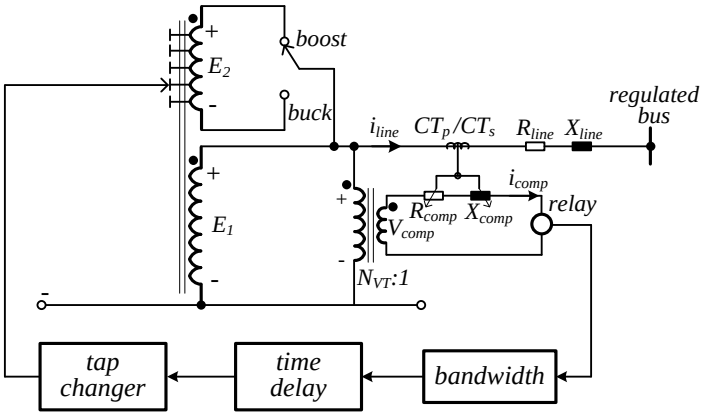

Fig. 3.15. Line drop compensation (LDC) of single-phase SVR: LTC+LDC

Based on Fig. 3.14, the current and voltage relationship among primary and secondary circuits for *Type B* tap changer can be simply determined by applying KVL and KCL as following:

$$V_S = \frac{1}{1-0.00625 \cdot n_{tap}} \cdot V_P \text{ and } i_P = \frac{1}{1-0.00625 \cdot n_{tap}} \cdot i_S \tag{3.40}$$

if the reversing switch is enabled for the *boost* mode. In case of *buck* mode operation:

$$V_S = \frac{1}{1+0.00625 \cdot n_{tap}} \cdot V_P \text{ and } i_P = \frac{1}{1+0.00625 \cdot n_{tap}} \cdot i_S \tag{3.41}$$

where n_{tap} specifies the tap level and determined by LDC. If R_{comp} and X_{comp} parameters are set to zero, then LDC will be equivalent to LTC. Assuming that impedance of the line section between SVR and remote point is given and there is no lateral which branches off the line section, then voltage drop along the line referred to Fig. 3.15 is simply obtained as:

$$V_{drop} = Z_{line} \cdot I_{line} = \left(R_{line} + j \cdot X_{line}\right) \cdot I_{line} \tag{3.42}$$

Multiplying both sides of (3.42) by $1/N_{VT}$ and writing the line current in terms of the compensation circuit current (I_{comp}), then $R_{comp,\Omega}$ and $X_{comp,\,\Omega}$ in ohm are computed by:

$$\frac{1}{N_{VT}} V_{drop} = \frac{1}{N_{VT}} \cdot \left(R_{line} + j \cdot X_{line}\right) \cdot \underbrace{\frac{CT_P}{CT_S} I_{comp}}_{I_{line}} \tag{3.43}$$

$$\begin{aligned} V_{comp} &= \underbrace{\frac{CT_P}{N_{VT} \cdot CT_S} \cdot \left(R_{line} + j \cdot X_{line}\right)}_{Z_{comp,\Omega}} \cdot I_{comp} \\ \rightarrow Z_{comp,\Omega} &= \frac{CT_P}{N_{VT} \cdot CT_S} \cdot \left(R_{line} + j \cdot X_{line}\right) \text{ in } \Omega \end{aligned} \tag{3.44}$$

where N_{VT} is turns ratio of the voltage measurement transformer, CT_P and CT_S refer to current ratings of primary and secondary windings of the current measurement transformer. So, $R_{comp,V}$ and $X_{comp,V}$ in volts can be determined from (3.44) as:

$$Z_{comp,V} = CT_s \cdot Z_{comp,\Omega} = \frac{CT_P}{N_{VT}} \cdot \left(R_{comp,\Omega} + j \cdot X_{comp,\Omega}\right) \text{ in volts} \tag{3.45}$$

From the steady-state modelling of view, operation steps of LDC will have briefly the following steps in Fig. 3.16.

As shown in Fig. 3.17, three-phase SVR can be formed by three separate LTC+LDC connected in wye or delta configurations. Similarly, open-delta SVR will be also constructed with two separate LTC+LDC. It should be noted that the closed delta-connected SVR provides higher overall range of regulation (±15%) when the regulators on each phase are set to the extreme tap positions (±10%). Since any tap change on a single phase will affect the voltage and current levels of the adjacent phases in closed delta configuration, it may also be necessary to update the tap positions of the other phases in order to maintain desired three-phase voltages. For this reason, specified bandwidth is usually set to wider values compared to that of wye-connected SVR.

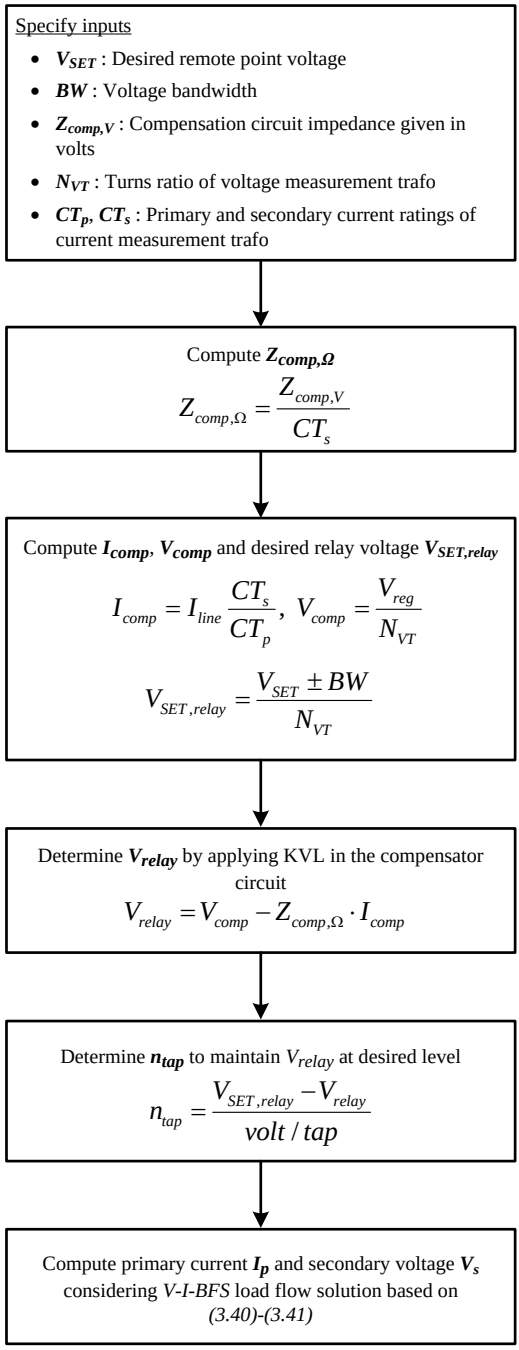

Fig. 3.16. Operation flowchart of LDC+LTC

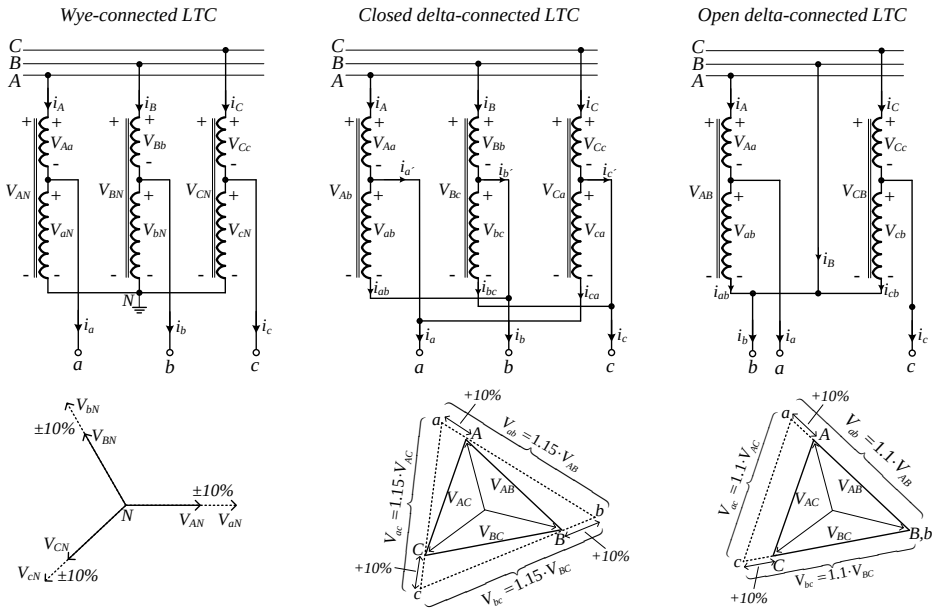

Fig. 3.17. Simplified single-line diagram of the VSC-grid connection

Applying KVL and KCL in Fig. 3.17 and based on [3.31], terminal voltage and current relationships for the three connection types are resulted below as long as the series and shunt winding impedances are neglected. For wye-connected SVR:

$$\begin{bmatrix} V_{aN} \\ V_{bN} \\ V_{cN} \end{bmatrix} = \begin{bmatrix} t_a & 0 & 0 \\ 0 & t_b & 0 \\ 0 & 0 & t_c \end{bmatrix} \begin{bmatrix} V_A \\ V_B \\ V_C \end{bmatrix}$$
$$\begin{bmatrix} I_A \\ I_B \\ I_C \end{bmatrix} = \begin{bmatrix} 1/t_a & 0 & 0 \\ 0 & 1/t_b & 0 \\ 0 & 0 & 1/t_c \end{bmatrix} \begin{bmatrix} I_a \\ I_b \\ I_c \end{bmatrix} \quad (3.46)$$

for closed delta-connected SVR:

$$\begin{bmatrix} V_{ab} \\ V_{bc} \\ V_{ca} \end{bmatrix} = \left(\begin{bmatrix} t_{ab} & 1-t_{bc} & 0 \\ 0 & t_{bc} & 1-t_{ca} \\ 1-t_{ab} & 0 & t_{ca} \end{bmatrix} \right)^{-1} \begin{bmatrix} V_{AB} \\ V_{BC} \\ V_{CA} \end{bmatrix}$$
$$\begin{bmatrix} I_A \\ I_B \\ I_C \end{bmatrix} = \left(\begin{bmatrix} t_{ab} & 0 & 1-t_{ca} \\ 1-t_{ab} & t_{bc} & 0 \\ 0 & 1-t_{bc} & t_{ca} \end{bmatrix} \right)^{-1} \begin{bmatrix} I_a \\ I_b \\ I_c \end{bmatrix} \quad (3.47)$$

and, for open delta-connected SVR in case that the regulators are connected between phases A-B and between phases C-B:

$$\begin{bmatrix} V_{ab} \\ V_{bc} \\ V_{ca} \end{bmatrix} = \begin{bmatrix} 1/t_{ab} & 0 & 0 \\ 0 & 1/t_{bc} & 0 \\ -1/t_{ab} & -1/t_{bc} & 0 \end{bmatrix} \begin{bmatrix} V_{AB} \\ V_{BC} \\ V_{CA} \end{bmatrix}$$
$$\begin{bmatrix} I_A \\ I_B \\ I_C \end{bmatrix} = \begin{bmatrix} 1/t_{ab} & 0 & 0 \\ -1/t_{ab} & 0 & -1/t_{bc} \\ 0 & 0 & 1/t_{bc} \end{bmatrix} \begin{bmatrix} I_a \\ I_b \\ I_c \end{bmatrix} \quad (3.48)$$

where t_{ij} represents single-phase effective ratio of the regulator connected between phases *i-j* and is defined as

$$t_{ij} = 1 \pm 0.00625 \cdot n_{tap_{ij}} \quad (3.49)$$

3.5 Computation of Network Power Losses

Regardless of what computation method is used, total branch losses of distribution networks can be calculated once bus voltages and branch currents all over the network are obtained accurately after running a load flow simulation. Although branch impedance can be used to estimate active power losses based on I^2R calculation, this method gives rise to inaccurate solution due to phase mutual couplings in 3-phase systems. In general, the loss dissipated along a branch is equivalent to the difference between branch entering and branch outgoing power.

$$S_{loss,k} = S_{fbus,k} - S_{tbus,k} = \begin{bmatrix} V^{a}_{fbus,k} \cdot \left(I^{a}_{fbus,k}\right)^{*} \\ V^{b}_{fbus,k} \cdot \left(I^{b}_{fbus,k}\right)^{*} \\ V^{c}_{fbus,k} \cdot \left(I^{c}_{fbus,k}\right)^{*} \end{bmatrix} - \begin{bmatrix} V^{a}_{tbus,k} \cdot \left(I^{a}_{tbus,k}\right)^{*} \\ V^{b}_{tbus,k} \cdot \left(I^{b}_{tbus,k}\right)^{*} \\ V^{c}_{tbus,k} \cdot \left(I^{c}_{tbus,k}\right)^{*} \end{bmatrix} \tag{3.50}$$

where $S_{fbus,k}$ denotes apparent power entering into the k_{th} branch and $S_{tbus,k}$ refers to the apparent power leaving the k^{th} branch.

3.6 Validation of the Developed Load Flow Solution Tool

After specifying network structure with certain bus-branch numbers by the user, these branches are re-numbered and sorted in radial sequence, and then node equations of network components are introduced. At the end, the distribution network is solved by *V-I-BFS* algorithm. In order to validate accuracy of resulted solutions, reference case studies will be necessary for the comparison. The most important considered performance criterion is the three-phase bus voltages here. If maximum difference of bus voltages resulted by the developed tool and by reference tool is below certain tolerable error, then the other outputs from the developed tool such as branch power flow and network losses will be assumed reliable.

On account of this, two IEEE test networks are used as base cases [3.41]. IEEE 4-bus test network is the simplest one but it has good purpose to evaluate 3-phase transformer models with various vector groups. A load group located at bus 4 (end of feeder) is supplied through the overhead lines at primary and secondary side of step-down transformer as depicted in Fig. 3.18. Conductor types and pole configurations are same with [3.41]. Load flow result in unbalanced case is presented in Table 3.5. Maximum voltage mismatches are resulted less than **0.2%** and it can be reduced further if the number of iterations is increased.

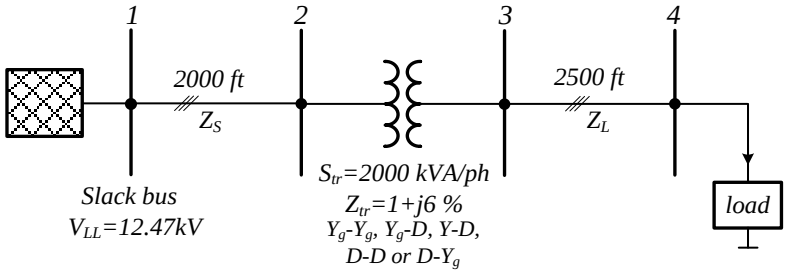

Fig. 3.18. IEEE 4-bus test feeder [3.27]

Table. 3.5. Transformer model valid for all configurations: Current and voltage computation for *BFS* steps

		D-Yg1					*D-D*				
Bus	V (volts)	IEEE 4-bus	New	θ (deg.)	IEEE 4-bus	New	IEEE 4-bus	New	θ (deg.)	IEEE 4-bus	New
1	V_a	12470.0	12470.0	θ_a	30.0	30.00	12470.0	12470.0	θ_a	30.0	30.00
	V_b	12470.0	12470.0	θ_b	-90.0	-90.00	12470.0	12470.0	θ_b	-90.0	-90.00
	V_c	12470.0	12470.0	θ_c	150.0	150.00	12470.0	12470.0	θ_c	150.0	150.00
2	V_a	12350.0	12350.3	θ_a	29.6	29.61	12341.0	12341.0	θ_a	29.8	29.81
	V_b	12314.0	12315.8	θ_b	-90.4	-90.39	12370.0	12370.3	θ_b	-90.5	-90.48
	V_c	12333.0	12333.2	θ_c	149.8	149.75	12302.0	12301.8	θ_c	149.5	149.55
3	V_a	2290.0	2289.1	θ_a	-32.4	-32.42	3902.0	3901.7	θ_a	27.2	27.2
	V_b	2261.0	2259.6	θ_b	-153.8	-153.79	3972.0	3972.4	θ_b	-93.9	-93.91
	V_c	2214.0	2215.1	θ_c	85.2	85.21	3871.0	3871.4	θ_c	145.7	145.74
4	V_a	2157.0	2154.7	θ_a	-34.2	-34.23	3431.0	3430.6	θ_a	24.3	24.28
	V_b	1936.0	1932.3	θ_b	-157.0	-157.06	3647.0	3647.3	θ_b	-100.4	-100.36
	V_c	1849.0	1854.6	θ_c	73.4	73.48	3294.0	3293.6	θ_c	138.6	138.62
		Number of iterations: 8					Number of iterations: 7				

On the other hand, IEEE 13-bus test network is used to examine modelling performance of various components such as cables and lines with diverse configurations, all kind of load types, shunt capacitors, voltage regulator and transformers. Fig 3.19 illustrates the 13-bus test network. Minor modifications have been applied on the original test network as following:

- Delta-connected, constant power (*Y-PQ*) uniformly distributed load situated between nodes 2 and 3 has been removed from the original network. Since most of the distributed load had been connected to phase *c*, the developed load flow running on the modified test network will overestimate phase *c* voltage.
- In the original test network, a switch and an additional node exist between node 3 and 11. Since load flow results published by IEEE consider only "*on*" state of the switch, it doesn't make sense to include it in this work.

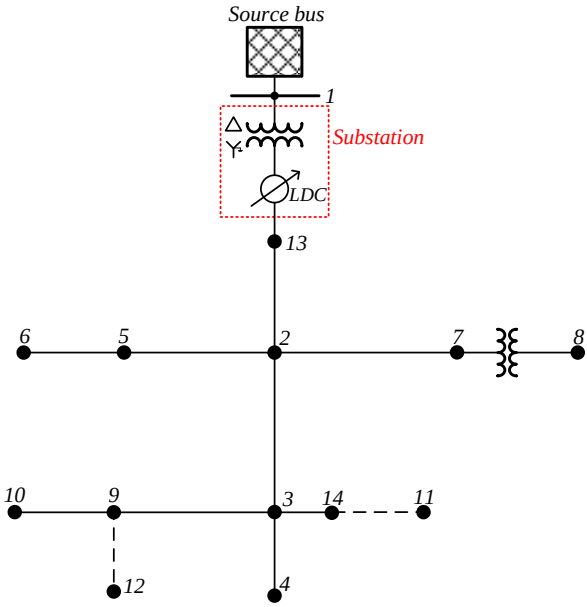

Fig. 3.19. IEEE 13-bus network [3.41]. Solid lines represent overhead lines; dashed lines refer to underground cables

Modelling data including above modifications to IEEE 13-bus test network is provided in Appendix C. It is usual that these minor modifications should not essentially affect the resulted bus voltages.

When line drop compensator (LDC) is initially disabled, phase voltages at remote nodes can drop to inadmissible levels in such that shunt capacitors located at *node 10*

and *11* will not be sufficient alone for supporting the voltage profile. Fig. 3.20 presents the bus voltages without LDC, and satisfied results (less than 1% mismatches) have been achieved as compared with the results obtained by Radial Distribution Analysis Package (RDAP) [3.42]. Phase *a* and *c* were subjected to high amount of voltage drops (less than 0.95 p.u.) so that LDC operation becomes necessary to maintain all phase voltages in acceptable ranges. On the other hand, interestingly, phase *b* experiences a voltage rise although a distributed generation does not exist. This is mainly caused by the mutual coupling between lightly loaded phase *b* and heavily loaded phases *a*, *c*. Shunt capacitors located at node 10 and 11 have also slightly boosting effect on the voltage. This result may be a good example to show that why running 3-phase unbalanced load flow is necessary for the voltage analysis of distribution networks.

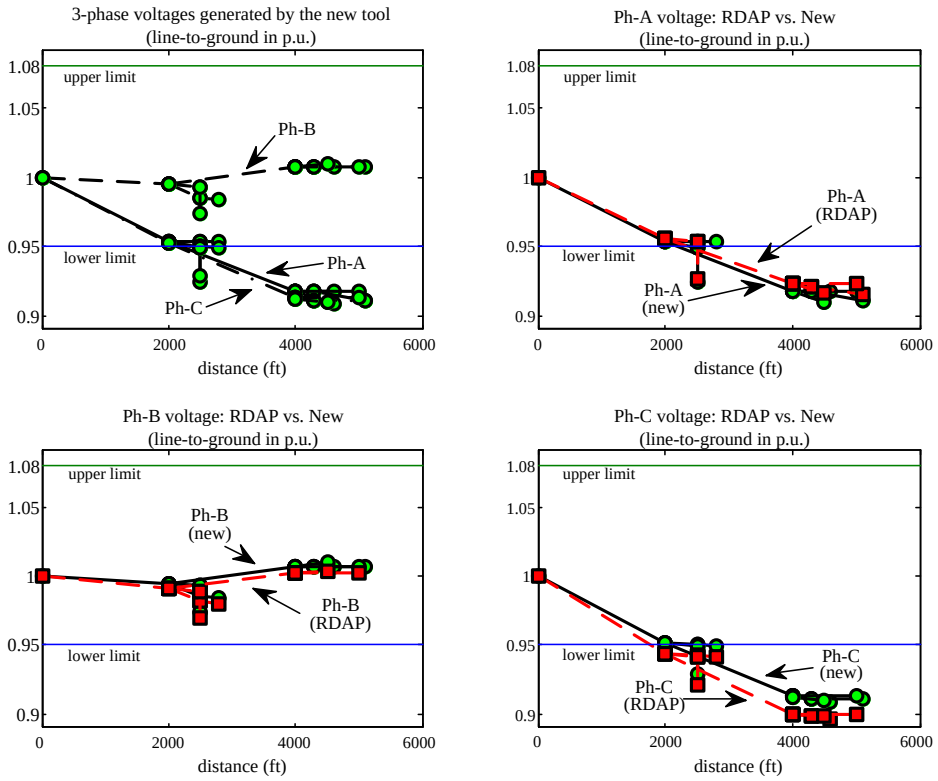

Fig. 3.20. Voltage profile of *IEEE 13-bus test network* without LDC

When the LDC taps are positioned at [10 8 11] for phase *a*, *b*, *c* respectively, minimum measured voltages in the network moves into the acceptable range. Fig. 3.21 shows the 3-phase line-to-ground voltage profile of the network provided by the developed load flow solution. However, in this case, the nearest nodes to LDC will experience more severe voltage boosting. Therefore, increasing tap positions further levels cannot be accepted although maximum tap position of the LDC is 16 for each phase. Therefore, connecting shunt capacitors at far end nodes can help mitigating this problem for long distribution feeders. The results obtained by the developed load flow simulation have been validated with IEEE test network result in Fig. 3.21. Phase *c* voltages from both results (without and with LDC operation) are overestimated due to removal of the uniformly distributed load in the modified network. Overall voltage mismatches take place in the acceptable level of 0.1-2 % as referenced to IEEE and RDAP simulation results.

After verification of the developed load flow solution in terms of line-to-ground voltages, 4-by-4 line impedance matrices have been utilized to solve neutral voltages at each node. Thus, line-to-neutral voltages where each loads, shunt capacitors and distributed generators are actually connected at can be computed. Fig. 3.22 illustrates comparison of resulting node voltages as line-to-ground and line-to-neutral together. If line-to-neutral node voltages are considered, then lightly loaded phase *b* moves to emergency condition and relevant tap setting of LDC or the rating of shunt capacitors connected to phase *b* must be re-adjusted to prevent this overvoltage situation. Another point is the effect of grounding impedance on the neutral voltage. As depicted in Fig. 3.23, neutral voltages do not vary substantially as grounding impedance is increased to 100 ohms. It is obvious that slightly shifting of neutral voltages up is observed due to the fact that higher grounding impedance forces more return currents to flow through the neutral conductor.

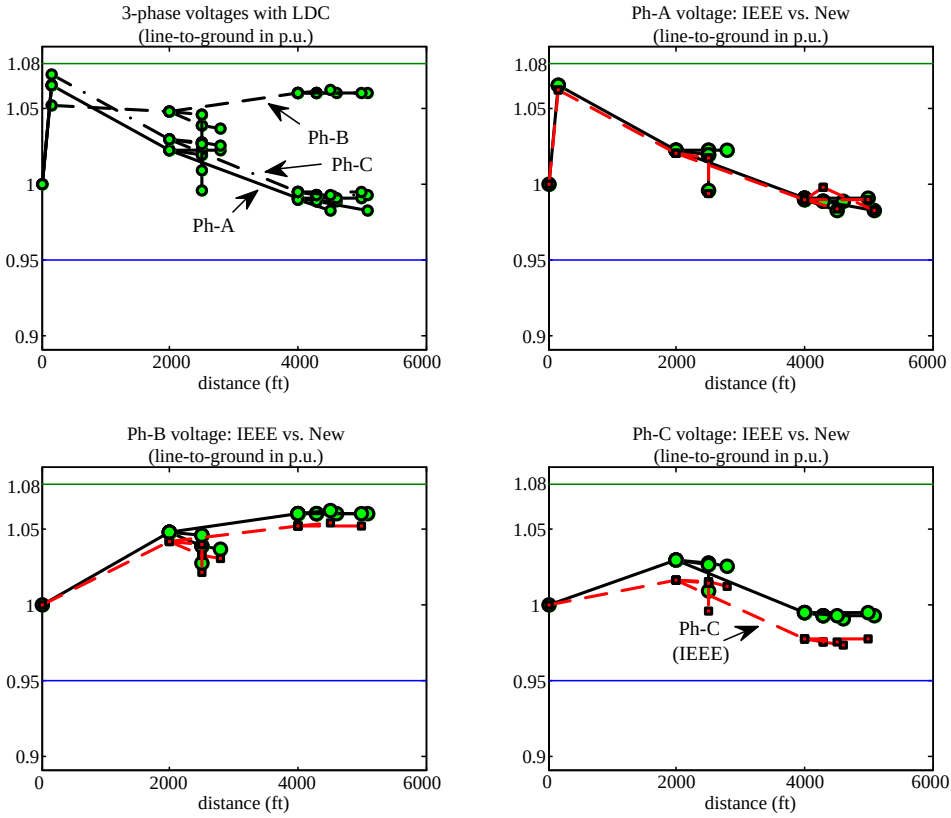

Fig. 3.21. Line-to-ground voltage profile of *IEEE 13-bus test network* with LDC

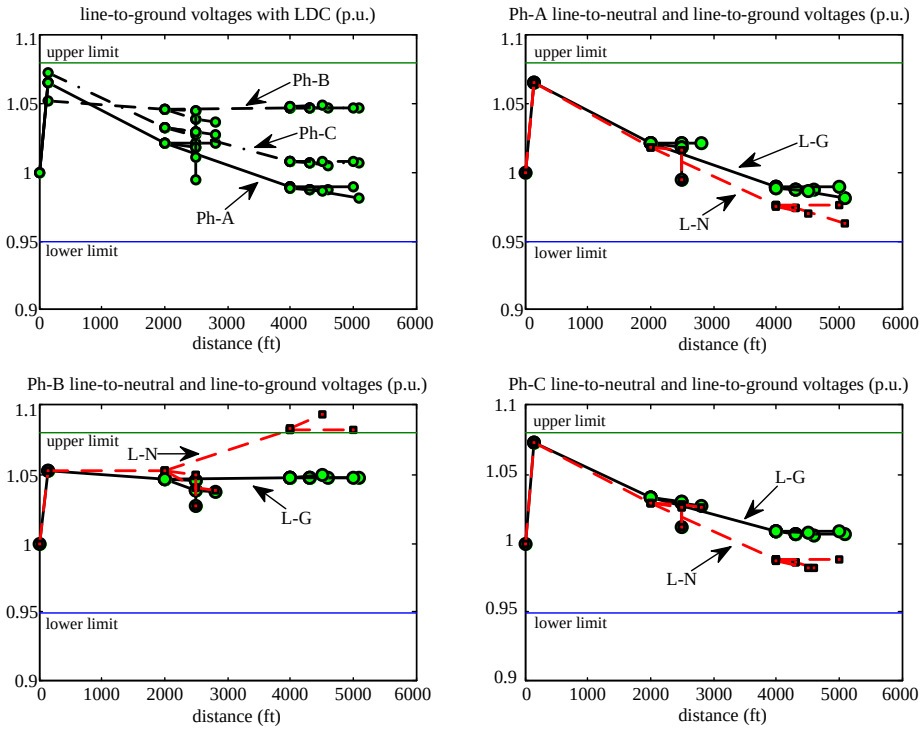

Fig. 3.22. Line-to-ground and line-to-neutral voltage profile of *IEEE 13-bus test network* with LDC

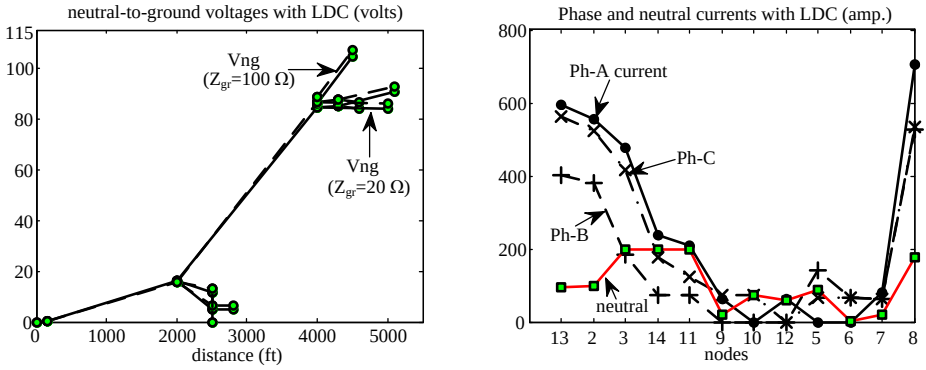

Fig. 3.23. Neutral-to-ground voltages and branch currents

3.7 Bibliography for Chapter 3

[3.1] H.E. Brown, G.K. Carter, H.H. Happ, and C.E. Person, "Power flow solution by impedance matrix iterative method," *IEEE Transactions on Power Apparatus and Systems*, vol. PAS-82, no. 65, pp. 1-10, April 1963.

[3.2] T.H. Chen, M.S. Chen, K.J. Hwang, P. Kotas, and E.A. Chebli, "Distribution system power flow analysis-A rigid approach," *IEEE Transactions on Power Delivery*, vol. 6, no. 3, pp. 1146-1152, July 1991.

[3.3] J.C.M. Vieira, W. Freitas, and A. Morelato, "Phase decoupled method for three phase power flow analysis of unbalanced distribution system," *IEE Proceedings of Generation, Transmission and Distribution*, vol. 151, no. 5, pp. 568-574, September 2004.

[3.4] K.P. Schneider, D. Chassin, Y. Chen, and J.C. Fuller, "Distribution power flow for smart grid technologies," *IEEE Power Systems Conference and Exposition*, pp. 1-7, Seattle, March 2009.

[3.5] J.E. Van Ness, "Iteration methods for digital load flow studies," *IEEE Transactions on Power Apparatus and Systems*, vol. 78, pp. 583-588, August 1959.

[3.6] W.F. Tinney and C.E. Hart, "Power flow solution by Newton's method," *IEEE Transactions on Power Apparatus and Systems*, vol. PAS-86, pp. 1449-1456, November 1967.

[3.7] W.F. Tinney and J.W. Walker, "Direct solutions of sparse network equations by optimally ordered triangular factorization," *Proc. of IEEE*, vol. 55, no. 11, pp. 1801-1809, November 1967.

[3.8] B. Stott, "Decoupled Newton load flow," *IEEE Transactions Power Apparatus and Systems*, vol. PAS-91, no. 5, pp. 1955-1959, September 1972.

[3.9] B. Stott and O. Alsac, "Fast decoupled load flow," *IEEE Transactions on Power Apparatus and Systems*, vol. PAS-93, no. 3, pp. 859-869, May 1974.

[3.10] R.D. Zimmerman and H.D. Chiang, "Fast decoupled power flow for unbalanced radial distribution systems," *IEEE Transactions on Power Systems*, vol. 10, no. 4, pp. 2045-2052, November 1995.

[3.11] V.M. da Costa, N. Martins, and J.L.R. Pereira, "Developments in the Newton Raphson power flow formulation based on current injections," *IEEE Transactions on Power Systems*, vol. 14, no. 4, pp. 1320-1326, November 1999.

[3.12] P.A.N. Garcia, J.L.R. Pereira, S. Carnerio, V.M. da Costa, and N. Martins, "Three-phase power calculations using the current injection method," *IEEE Transactions on Power Systems*, vol. 15, no. 2, pp. 508-514, May 2000.

[3.13] A. Abur, H. Singh, H. Liu, and W.N. Klingensmith, "Three phase power flow for distribution systems with dispersed generation," *14th Power Systems Computation Conference (PSCC)*, Sevilla, June 2002.

[3.14] R. Berg, E.S. Hawkins, and W.W. Pleines, "Mechanized calculation of unbalanced load flow on radial distribution circuits," *IEEE Transactions on Power Apparatus and Systems*, vol. 86, No. 4, pp. 415-421, April 1967.

[3.15] W.H. Kersting and D.L. Mendive, "An application of ladder network theory to the solution of three-phase radial load flow problems," *IEEE PES General Winter Meeting*, January 1976.

[3.16] D. Shirmohammadi, H.W. Hong, A. Semlyen, and G.X. Luo, "A compensation based power flow method for weakly meshed distribution networks," *IEEE Transactions on Power Systems*, vol. 3, no. 2, pp. 753-762, May 1988.

[3.17] G.X. Luo and A. Semlyen, "Efficient load flow for large weakly meshed networks," *IEEE Transactions on Power Systems*, vol. 5, no. 4, pp. 1309-1316, November 1990.

[3.18] C.S. Cheng and D. Shirmohammadi, "A three phase power flow method for real time distribution system analysis," *IEEE Transactions on Power Systems*, vol. 10, no. 2, pp. 671-679, May 1995.

[3.19] J.H. Teng, "A direct approach for distribution system load flow solutions," *IEEE Transactions on Power Delivery*, vol. 18, no. 3, July 2003.

[3.20] M.F. AlHajri and M.E. El-Hawary, "Exploiting the radial distribution structure in developing a fast and flexible radial power flow for unbalanced three-phase networks," *IEEE Transactions on Power Delivery*, vol. 25, no. 1, pp. 378-389, January 2010.

[3.21] R.D. Zimmerman, "Comprehensive distribution power flow: Modeling, formulation, solution algorithms and analysis," Ph.D. dissertation, Cornell University, January 1995.

[3.22] W.H. Kersting, *Distribution System Modeling and Analysis*. CRC, Boca Raton, FL, 2002.

[3.23] T. H. Cormen, *Introduction to Algorithms*, MIT Press, 2001.

[3.24] J.J. Grainger and W.D. Stevenson, *Power System Analysis*, McGraw-Hill, 1994.

[3.25] J. R. Carson, "Wave propagation in overhead wires with ground return," *Bell System Technical Journal*, pp. 539-554, 1926.

[3.26] W.H. Kersting and R.K. Green, "The application of Carson's equation to the steady-state analysis of distribution feeders," *IEEE Power Systems Conference and Exposition (PSCE)*, Phoenix, March 2011.

[3.27] R.M. Ciric, A.P.Feltrin and L.F. Ochoa, "Power flow in four-wire distribution networks-General approach," *IEEE Transactions on Power Systems*, vol. 18, no. 4, pp. 1283-1290, November 2003.

[3.28] R. Dugan, S. Carneiro, L.R. Araujo and D. Penido, "Neutral-to-Earth voltage (NEV) test case," *IEEE PES Distribution System analysis Subcommittee*, 2010.

[3.29] *Benchmark Systems for Network Integration of Renewable and Distributed Energy Resources (draft)*, CIGRE Task Force C6.04.02, version 7 March 2011.

[3.30] Nexans Power Cables 1-30 kV datasheet, edition 2004.

[3.31] W.H. Kersting, *Distribution System Modeling and Analysis*, CRC Press, 2007.

[3.32] W.H. Kersting, "Radial distribution test feeders," *IEEE Power Engineering Society Winter Meeting*, pp. 908-912, 2001.

[3.33] *IEEE Standard Requirements, Terminology, and Test Code for Step-Voltage Regulators*, IEEE Std C57.15-2009.

[3.34] T. Gonen, *Electric Power Distribution System Engineering*, 2nd edition, CRC Press, 2007.

[3.35] E.R. Collins, J. Jiang, "Analysis of elevated neutral-to-earth voltage in distribution systems with harmonic distortion," *IEEE Transactions on Power Delivery*, vol. 24, no. 3, pp. 1696-1702, July 2009.

[3.36] *IEEE Recommended Practice for Grounding of Industrial and Commercial Power Systems*, IEEE Std. 142-1992.

[3.37] T.H. Chen, M.S. Chen, T. Inoue, P. Kotas, E.A. Chebli, "Three-phase cogenerator and transformer models for distribution system analysis," *IEEE Transactions on Power Delivery*, vol. 6, no. 4, pp. 1671-1681, October 1991.

[3.38] S.S. Moorthy, D. Hoadley, "A new phase-coordinate transformer model for Ybus analysis," *IEEE Transactions on Power Systems*, vol. 17, no. 4, pp. 951-956, November 2002.

[3.39] P. Xiao, D.C. Yu, W. Yan, "A unified three-phase transformer model for distribution load flow calculations," *IEEE Transactions on Power Systems*, vol. 21, no. 1, pp. 153-159, February 2006.

[3.40] M.R. Irving, A.K.Al-Othman, "Admittance matrix models of three-phase transformers with various neutral grounding configurations," *IEEE Transactions on Power Systems*, vol. 18, no. 3, pp. 1210-1212, August 2003.

[3.41] http://ewh.ieee.org/soc/pes/dsacom/testfeeders/index.html

[3.42] RDAP User Manual, WH Power Consultants, Las Cruces, NM. http://www.zianet.com/whpower

Chapter 4
Low Voltage (LV) Distribution Networks and Estimation of Their Maximum PV Hosting Capacity

This chapter mainly presents a methodology for the estimation of photovoltaic (PV) hosting capacity of low voltage (LV) distribution networks. General considerations on network planning procedure and network structures are given in the following subsections. Steady-state voltage variations and thermal loading of transformers as two main limitations are addressed. Since distribution network characteristics are not unique, critical reference LV networks have been built and used to estimate the amount of maximum allowable PV connections under the assumption of balanced load flow.

4.1 Background

Grid-connected PV installations are implemented as either large-scale PV parks or small-scale distributed PV systems. Rated power of PV park installations is usually realized in MW-peak ranges and connected to medium voltage (MV) or sub-transmission power networks. Hosting capacity of these networks is higher as compared to that of LV distribution networks. The PV capacity limit in MV and HV networks will not become a big issue for large-scale PV parks. Some reasons for it can be listed as following:

- Overhead lines employed in MV and transmission networks show inductive behaviour so that voltage sensitivity to reactive power will be high, thus voltage support based on reactive power control of PV installations becomes more feasible.
- Compared to LV networks, connection points of PV parks are both physically and electrically closer to on-load tap changers and automatic voltage regulators. Therefore, the grid seen by the PV parks exhibits strong behaviour.
- MV and sub-transmission networks are usually built as meshed-loop structures. This strengthens voltage profile and network loading with high PV penetration.

In the case of small-scale distributed PVs, mostly residential and commercial buildings occupy their rooftops and/or facades with PV installations. PV potential depends on the surface area so that individual PV systems connected to public LV networks are usually rated between 1-30 kWp. Although rated power of each distributed PV system is not much, higher impedance (or less short-circuit power) seen by the grid connection points in LV networks can create risk of overvoltages. Furthermore, equivalent impedance seen by the small-scale PV systems shows more resistive characteristics due to short underground cables. Thus, reactive power control by PV inverters becomes less efficient on the voltage variation and it requires higher reactive power flow in radial LV networks to impact the voltage profile adequately. On the other hand, regarding of thermal loading of MV/LV transformers and cables, this additional reactive power flow generated by distributed PV inverters has to be limited.

The challenge here is to increase PV capacity of electricity networks as much as possible with minimum network reinforcements. Due to the fact that increasing PV penetration level has more stringent limitations on public LV networks, the dissertation only focuses on small-scale distributed PV systems.

4.2 Planning and Operational Considerations of Distribution Networks

The main goal of electrical power system is to supply electrical energy to its customers

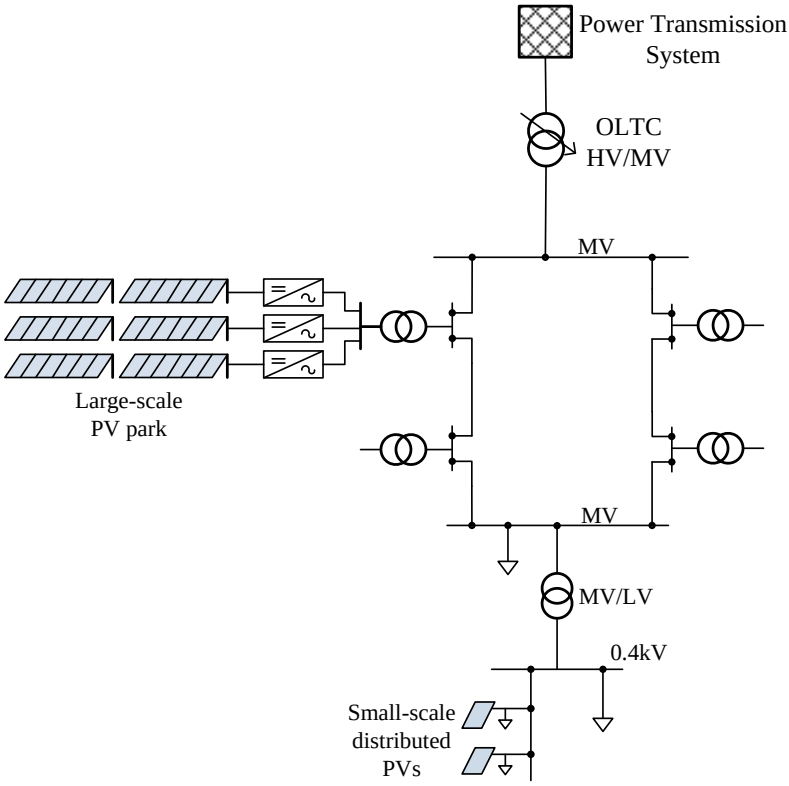

Fig. 4.1. Grid connection of large-scale PV parks and small-scale distributed PV systems

with certain level of power quality in reliable and economical manner. For this purpose, network planning in *generation*, *transmission* and *distribution* levels may have distinct and specific technical/economical requirements in such a way that overall cost of electrical energy is minimized (Fig. 4.2). Because of this, electrical power produced by centralized power plants is transferred to transmission lines through step-up transformers in order to reduce losses along long overhead lines. After that, voltage level is decreased by step-down transformers near load centres that form MV and LV

distribution networks. Depending on the load density (kW/km^2) served to a geographical area, cross sections of lines/cables and nominal voltages of distribution network from internationally recommended voltages are determined without violating technical requirements of relevant grid standards. Peak load ratings and geographical information of the region will be necessary inputs to evaluate maximum voltage drops along lines/cables. Once selected network components fulfil the requirements imposed by grid standards, then an economical evaluation on the candidate components are performed. For example, an oversized line can result in lower losses and less voltage drop however cost of an oversized line will be predominant limit in this case. Fig. 4.2 summarizes a distribution network planning procedure. Detailed principles on the network planning procedures can be found in [4.2]-[4.4].

Typical AC voltage levels according to IEC 60038 are given in Table 4.1 [4.1]-[4.2]. As an example, 60 kV is commonly used voltage level in HV subtransmission system while 20 kV and 10 kV are preferred voltage levels in MV distribution networks for Denmark. On-load tap changers (OLTCs) are utilized at 60/20 or 60/10 kV substations. During operation of distribution networks, network operator has to maintain certain level of voltage quality for the customers. An overvoltage, undervoltage, intolerable unbalanced voltage and harmonics, voltage dips/swells can trig malfunctioning of electrical equipment and tripping distributed generators in industrial, commercial or residential zones. Therefore, international or national grid standards predetermine normal and abnormal operation ranges. European voltage standard EN 50160 [4.5] sets a ±10% band of nominal steady-state voltages in MV and LV networks for 95% of a week measured as 10-minute average. For LV networks, 100% of the 10-minute average values measured during 1 week of period shall not be outside the +10%/-15% of the nominal voltage. It should be noticed that voltages measured in several minutes can be outside of the specified band. At least, this gap is filled by the other grid standards that are directly relevant to distributed generators (e.g., automatic disconnection from the grid in seconds). However some countries such as France, Spain, Norway, Netherlands, Portugal and Hungary impose more strict rules on the voltage characteristics [4.7]. In Norway, for instance, 100% of the 1-min average RMS

(root-mean-square) voltages shall be within ±10% of the nominal voltage [4.7]. It should be noticed that all these limits are operational constraints to evaluate the voltage quality. In reality, network operators put additional margins below these limits during planning stage of the networks so that risks and unforeseen results in operation of the networks can be alleviated. As an example, 1.06 p.u. is recommended as maximum steady-state voltage by EDF in France [4.11]. On the other hand, the stricter voltage limitations may unnecessarily reduce the allowable PV capacity.

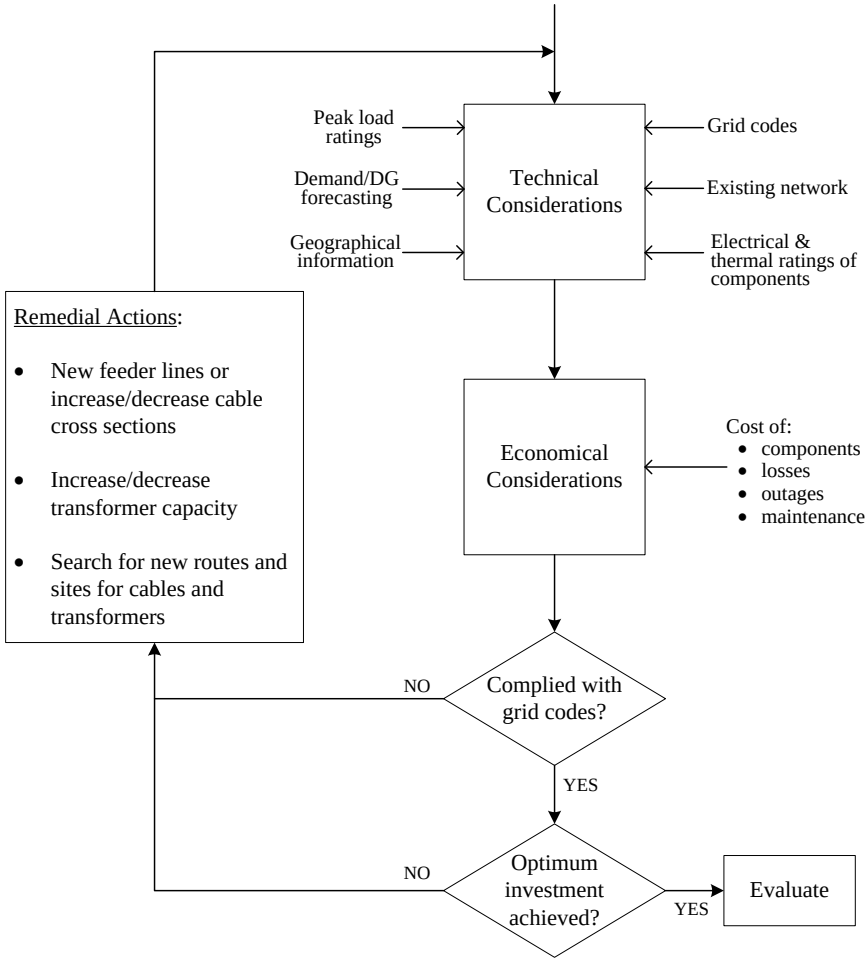

Fig. 4.2. Electricity distribution network planning procedure

Table. 4.1. Standard voltages according to IEC 60038

	Nominal line-to-line voltage (kV)	*Remarks*		*Nominal line-to-line voltage (kV)*	*Remarks*
EHV	1200		*MV*	33	
	765			22	
	525			11	
	420			6.6	Not for public systems
	363	Not recommended for new installations		3.3	Not for public systems
	300	Not recommended for new installations	*LV*	1	
HV	220			0.69	
	150	Not recommended for new installations		0.48	
	132			0.4	
	110				
	66				
	45	Not recommended for new installations			

Grid standards such as EN 50160 do not deal completely with distributed generators. Additional grid standards from distributed generators side are also imposed by the operators. Recently published European standard for the connection of micro-generators in parallel with public low-voltage distribution networks EN 50438 [4.8] requires an interface protection system for every grid-connected distributed generators in order to guarantee safety and reliable operation of electricity networks. Fig. 4.3 presents interface protection setting for distributed generators accepted in Denmark together with its clearance time. In this case, if the grid voltage is in abnormal state, distributed generators shall cease energizing the network and by this way, negative effects owing to the generators can be eliminated. In addition to this interface protection mechanism and EN 50160 standard, voltage rise caused by distributed generators is limited by some other grid standards such as [4.9]-[4.10] in Germany. For example, maximum allowable voltage rise is 3% for LV and 2% for MV networks caused by all distributed generators. Thus, network operators are responsible for the calculation of total voltage rise from the knowledge of the rated power of generators

and their locations along feeder. Based on Fig. 4.4, voltage rise can be simply estimated as following for balanced power flow (imaginary part of the voltage rise has been neglected):

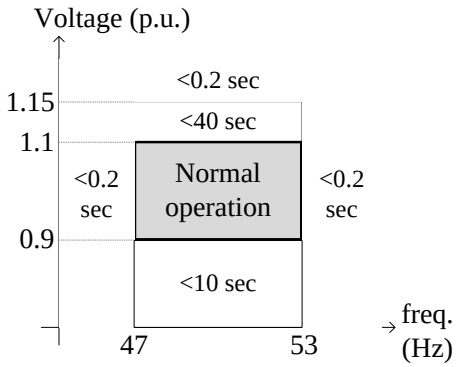

Fig. 4.3. Interface protection settings of micro-generators for Denmark according to DS/EN 50438

$$\begin{aligned}\Delta U_{LL} &\cong \sqrt{3}\cdot\left(R\cdot\vec{I}\cdot\cos\varphi + X\cdot\vec{I}\cdot\sin\varphi\right)\\ &= \sqrt{3}\cdot\left(R\cdot\frac{P_{net}}{\sqrt{3}U_{LL}} + X\cdot\frac{Q_{net}}{\sqrt{3}U_{LL}}\right) = \frac{R\cdot P_{net} + X\cdot Q_{net}}{U_{LL}}\end{aligned} \tag{4.1}$$

For single phase connection:

$$\begin{aligned}\Delta U_{LN} &\cong \left(R_{ph} + R_{neutral}\right)\cdot I\cdot\cos\varphi + \left(X_{ph} + X_{neutral}\right)\cdot I\cdot\sin\varphi\\ &= \frac{\left(R_{ph} + R_{neutral}\right)\cdot P + \left(X_{ph} + X_{neutral}\right)\cdot Q}{U_{LN}}\end{aligned}$$

where R and X denote equivalent impedances seen from the connection point. U_{LL} is the line-to-line voltage measured before the generator is connected. P_{net} and Q_{net} are the net power combined with consumption and production at the connection point. Positive sign of real and reactive power corresponds to power injection into the grid.

By reasoning (4.1), in order to estimate maximum allowable generator connection based on 3% or 2% voltage rise limitations, network operator has to know equivalent

impedances seen by the generators. This can be automatized by running successive load flows on the network if the network structure is already introduced to the simulation tool. The relevant flowchart for estimation of maximum allowable PV connection is depicted in Fig. 4.5.

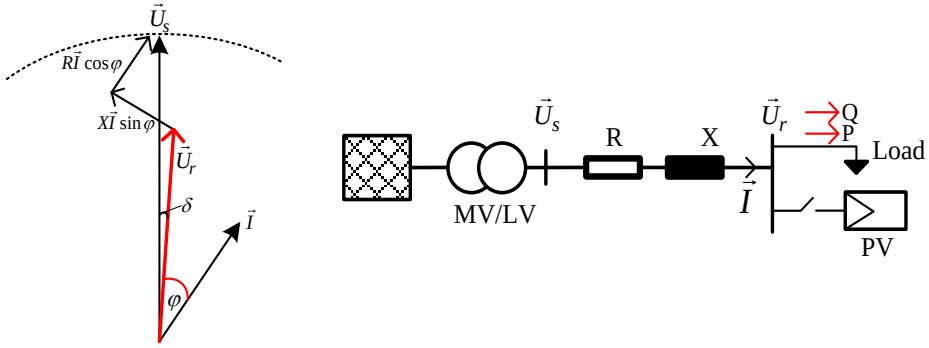

Fig. 4.4. Phasor and circuit representation of voltage rise/drop

It is obvious that VDE-AR-N 4105 standard [4.9] in Germany is stricter than EN 50168 and it may lead to less utilization of PV capacity. Another comment is that voltage rise criteria in VDE-AR-N 4105 concerns allowable generator connections in network planning stage, while EN 50160 defines certain limitations for the network operation stage after connecting the generators to grid. By employing information technologies (IT) in the near future, distribution networks can be always guaranteed to operate in admissible voltage variations by controlling generator's real and reactive power, tap-changing mechanisms of substations, and so on. Therefore, any constraints imposed during network planning stage may not be necessary at all in the near future.

A typical voltage profile from HV/MV substation to the furthest LV consumer under the maximum load and no generation condition is illustrated in Fig. 4.6. According to [4.12], total voltage drop in a properly designed distribution network is mostly divided as: 5% drop on MV feeder, 3% drop along MV/LV transformer, 5% drop along LV feeder including service cables, and 1% for a margin. If the minimum operation voltage is 90% (0.9 p.u.) of the nominal voltage at the furthest LV consumer (EN 50160), then

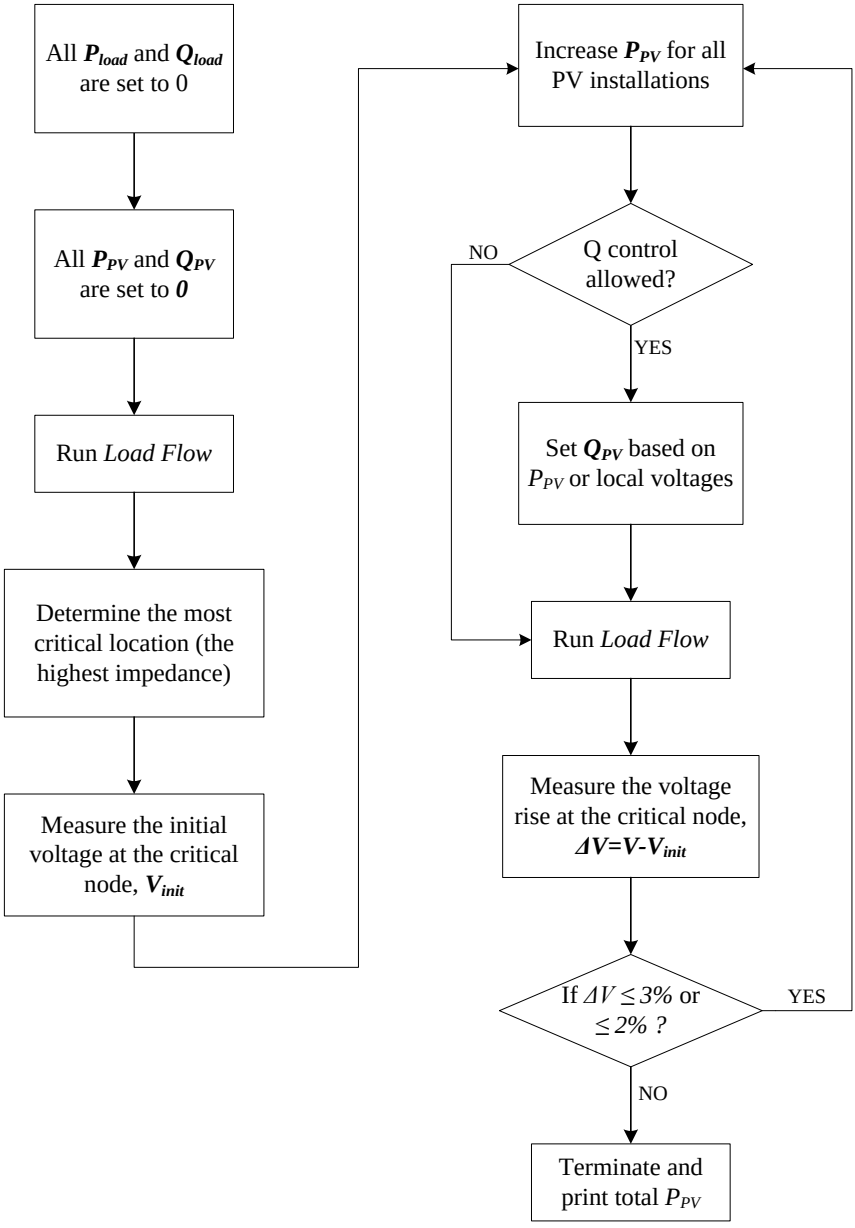

Fig. 4.5. Flowchart for maximum allowable PV connection based on voltage rise limitation

secondary side of HV/MV substation should be maintained around 1.04 p.u. voltage level by means of tap changers.

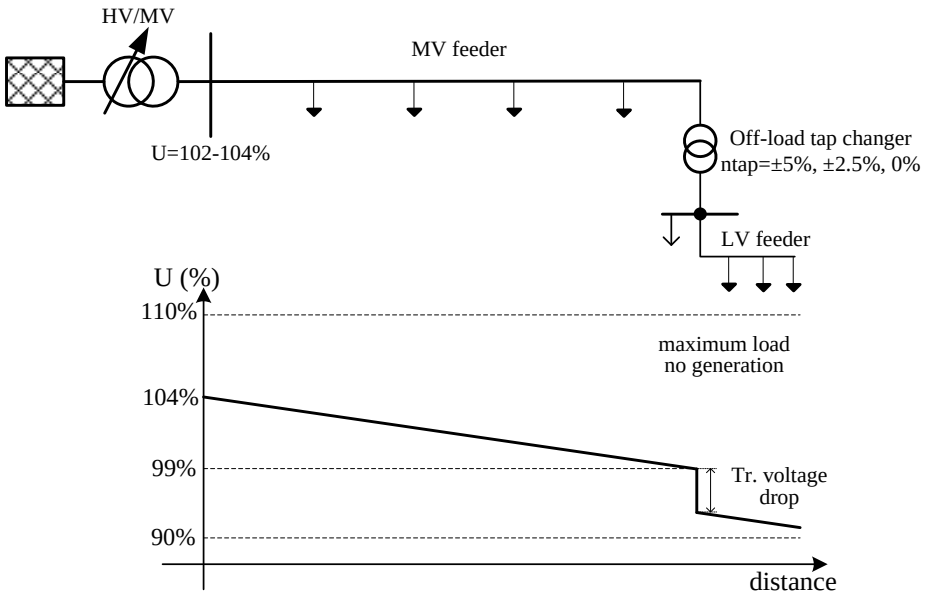

Fig. 4.6. Typical voltage profile from MV to LV customers under the maximum load and no generation

In case of no load and maximum generation condition for LV feeder with the same MV network, real power will be exported from the LV feeder towards the MV feeder and eventually voltage profile will be changed as shown in Fig. 4.7. Voltage drops (rise) are typically divided as: 2% rise along MV feeder, 3% rise along MV/LV transformer and LV feeder, 1% for margin [4.12]. At first glance, PV connection capacity can be increased further by reducing the HV/MV substation voltage below 1.04 p.u. but it is possible that multiple MV/LV transformers associated with LV customers can be connected to the same substation. For example, when two LV networks given in Fig. 4.6 and 4.7 are connected to the same substation, then the tap settings cannot be adjusted flexibly due to the existence of undervoltage and overvoltage limits at both feeders.

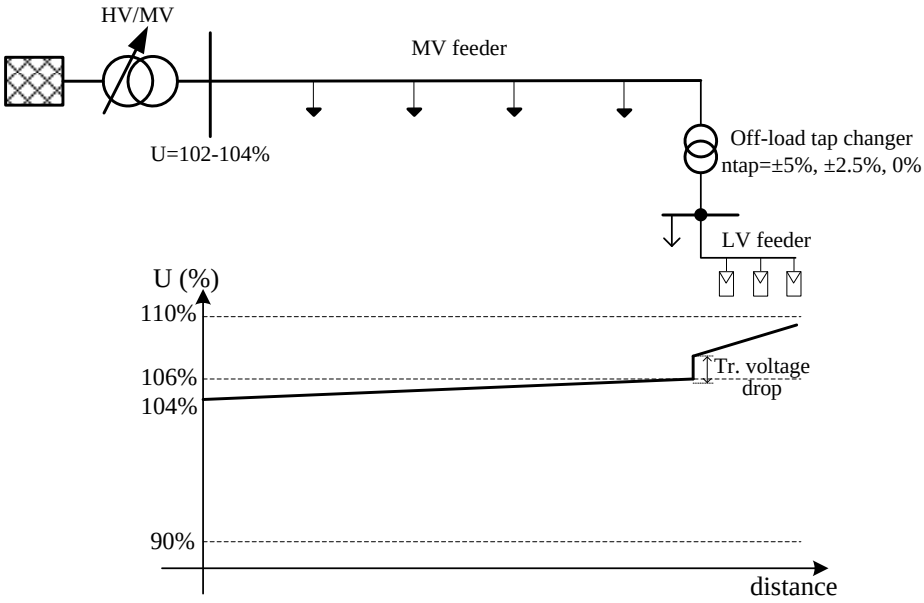

Fig. 4.7. Typical voltage profile from MV to LV customers under the no load and maximum generation in LV feeder

Apart from the steady-state voltage limitations, the other important constraint is the maximum thermal loading of network components such as transformers and conductors. From the network reinforcement point of view, investment on transformers costs higher as compared to lines and cables. Therefore, only thermal loading of transformers will be considered in this chapter. Hot-spot temperature measured at the windings inside oil tank will be the limiter criterion for power transformers while nominal currents provided by manufacturers will be taken into consideration as the maximum permissible limit of lines/cables.

4.3 Transformer Thermal Model

More precise estimation of PV hosting capacity can be achieved if transformer thermal model is included to calculation of the maximum overloading level. Power flow through transformer is mainly limited due to the ageing of insulation materials and deterioration of oil thermal conductance with increasing temperature levels. Since

transformer windings are the main heat source, the maximum measured temperature will be simply located in the winding sections. This maximum level is called hot-spot temperature of a transformer. Regarding of the mostly used oil-immersed transformers, Montsinger's law reveals that transformer lifetime reduces in double at each 8°C increments of hot-spot above 90°C [4.2]. Thanks to the years of experiences on the oil-immersed transformers, lifetime estimation is well established, so approximately 25-year lifetime is expected under continuous 98°C hot-spot operation condition [4.2].

The oil-immersed transformer thermal model used in this work is inherited from IEC 60076-7 [4.13]. It is assumed that air temperature of the region matches to the ambient temperature of the transformer for outdoor installations. By this way, transformer discrete thermal model and load flow calculations have been carried out together in Matlab®.

The difference equations are employed as following in (4.2)-(4.7) [4.13]. The hot-spot temperature at n^{th} step ($\theta_{h(n)}$) is the sum of the top-oil temperature ($\theta_{o(n)}$) and the hot-spot temperature rise ($\Delta\theta_{h(n)}$) as given in (4.2).

$$\theta_{h(n)} = \theta_{o(n)} + \Delta\theta_{h(n)} \tag{4.2}$$

The top-oil temperature at each time step is estimated for given ambient temperature (τ_a) and transformer load factor $K = S/S_{rated}$ as:

$$\theta_{o(n)} = \theta_{o(n-1)} + D\theta_{o(n)} \tag{4.3}$$

$$D\theta_o = \frac{Dt}{k_{11}\tau_0} \cdot \left[\left(\frac{1+K^2R}{1+R} \right)^x \cdot \Delta\theta_{or} - \left(\theta_o - \theta_a \right) \right] \tag{4.4}$$

where "*D*" operator denotes the simulation time step (e.g., 15 minutes). The other distribution transformer-specific parameters in reasonable accuracy are provided in Table 4.2 (Annex E, Table E.1 in [4.13]) which is valid only for the transformers

having rated power below 2.5 MVA. The hot-spot temperature rise ($\Delta\theta_{h(n)}$) is estimated in (4.5)-(4.7) and inserted into (4.2).

$$\Delta\theta_{h(n)} = \Delta\theta_{h1(n)} - \Delta\theta_{h2(n)} \tag{4.5}$$

$$D\Delta\theta_{h1} = \frac{Dt}{k_{22}\cdot\tau_{\omega}}\cdot\left[k_{21}\cdot\Delta\theta_{hr}\cdot K^{y} - \Delta\theta_{h1}\right] \tag{4.6}$$

$$D\Delta\theta_{h2} = \frac{Dt}{\left(1/k_{22}\right)\cdot\tau_{o}}\cdot\left[\left(k_{21}-1\right)\cdot\Delta\theta_{hr}\cdot K^{y} - \Delta\theta_{h2}\right] \tag{4.7}$$

Table. 4.2. A characteristic data for power transformer [4.13]

Symbol	*Meaning*	*Value*
x	Exponential power of total losses versus top-oil temperature rise (oil exponent)	0.8
y	Exponential power of current versus winding temperature rise (winding exponent)	1.6
R	Ratio of load losses at rated current to no-load losses	5
H	Hot-spot factor	1.1
τ_o	Average oil time constant	180 min
τ_w	Winding time constant	4 min
$\Delta\theta_{hr}$	Hot-spot-to-top-oil gradient at rated current	23 K
$\Delta\theta_{or}$	Top-oil temperature rise in steady state at rated losses (no-load losses+load losses)	55 K
k_{11}	Thermal model constant	1.0
k_{21}	Thermal model constant	1.0
k_{22}	Thermal model constant	2.0
Dt	Simulation time step	3 min
S_{rated}	Transformer nominal power	400 kVA

Equation (4.7) represents the oil viscosity that is not negligible for the transformers with natural cooling and non-directed-flow pumped-oil cooling mechanisms [4.13].

The rate of ageing (V) referred to the hot-spot temperature is estimated as:

$$V = 2^{(\theta_h - 98)/6} \tag{4.8}$$

when thermally upgraded insulation paper is not used. If thermally upgraded insulation paper is used, the rate of ageing becomes as:

$$V = e^{\left(\frac{15000}{110+273} - \frac{15000}{\theta_h+273}\right)} \tag{4.9}$$

Unity ageing rate implies the transformer operation with the hot-spot temperature of 98°C for non-thermally upgraded paper and 110°C for thermally upgraded paper. Eventually, the loss of life (L) is calculated over a certain period of time as following:

$$L = \sum_{n=1}^{N} \left(V_n \cdot t_n\right) \tag{4.10}$$

Fig. 4.8 shows that the hot-spot temperature increases with load level and the ambient temperature. Utilization of thermally upgraded insulation paper will considerably strength the lifetime. Therefore, regarding of the 98°C hot-spot limit, PV hosting capacity can be further increased by means of cooler ambient temperatures and thermally upgraded paper.

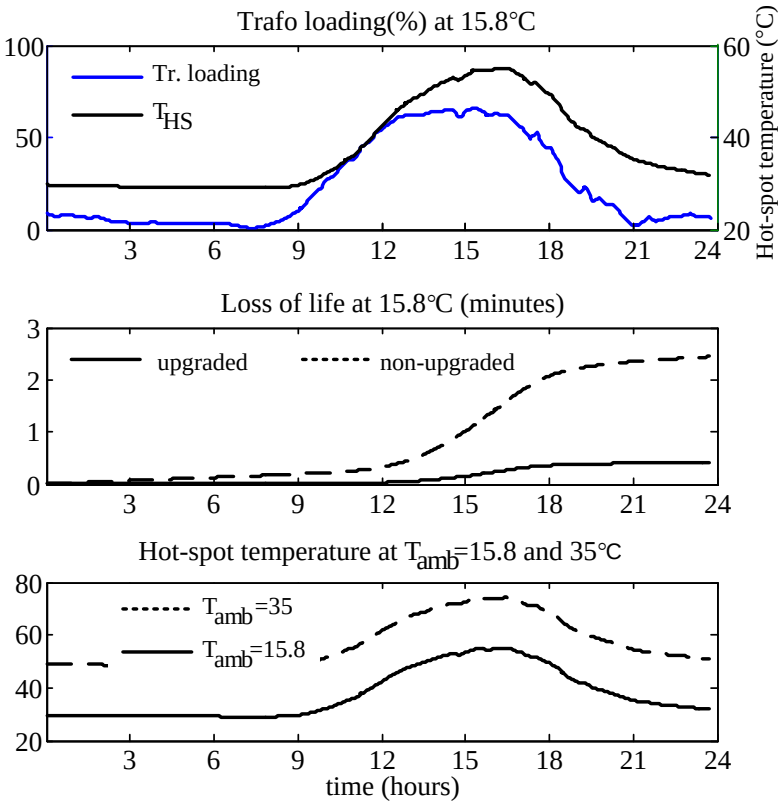

Fig. 4.8. Transformer hot-spot temperature variation and loss of life for the specified power flow and ambient temperature

4.4 Reference LV Network Models

Reference LV grid models are mainly required for two reasons. First, it should be clearly determined that what constraints against to higher PV penetration are more influential on the different network types. Second, in order to increase PV hosting capacity, the most effective static reactive power methods that cause minimum grid losses and maximum voltage support should be suggested for all types of networks. For these purposes, all LV grid structures are grouped into four types for the simplicity: urban, suburban, rural and farm networks [4.14]. Urban networks mostly accommodate high-rise, small-distant buildings and several apartments share the same rooftop for PV installation. This limited amount of PV potential and high density power demand in the

neighbourhood make the urban networks less critical for high PV penetration study. Therefore, urban networks will be ignored in this work.

Short circuit power ($S_{sc,MV}$) and R/X impedance ratio at the primary side of MV/LV transformer, nominal voltage of MV network (U_{MV}), nominal apparent power of transformer (S_{tr}), number of LV feeders departing from the transformer and their associated average lengths, distance between neighbour nodes are the basic parameters to define reference LV grids [4.14]. Table 4.3 gives necessary parameters and their average values for the suburban, rural, farm networks summarized from [4.14]-[4.17].

Table. 4.3. Parameters of the reference LV networks

	Critical Networks		
	Suburban	Rural	Farm
U_{MV} (kV)	10	20	20
S_{sc} (MVA)	150	80	40
R/X	0.6	0.55	0.5
S_{tr} (kVA)	630	400	100
Number of feeders	5	3	1
Length of feeders (m)	300	400	900
Distance between neighbors (m)	17	32	54
Length of service lines (m)	10	10	10
Number of consumer connection points	85 (17 per feeder)	36 (12 per feeder)	10
Feeder cable type	Al 150 mm2 underground	Al 120 mm2 OHL	Al 95 mm2 OHL
Service cable type	Al 50 mm2 underground	Al 25 mm2 OHL	Al 25 mm2 OHL

For the sake of simplicity, suburban and farm network models will be sufficient to cover reactive power control aspects of solar inverters. So, the resulting single-line diagram of the network models is depicted as in Fig. 4.9.

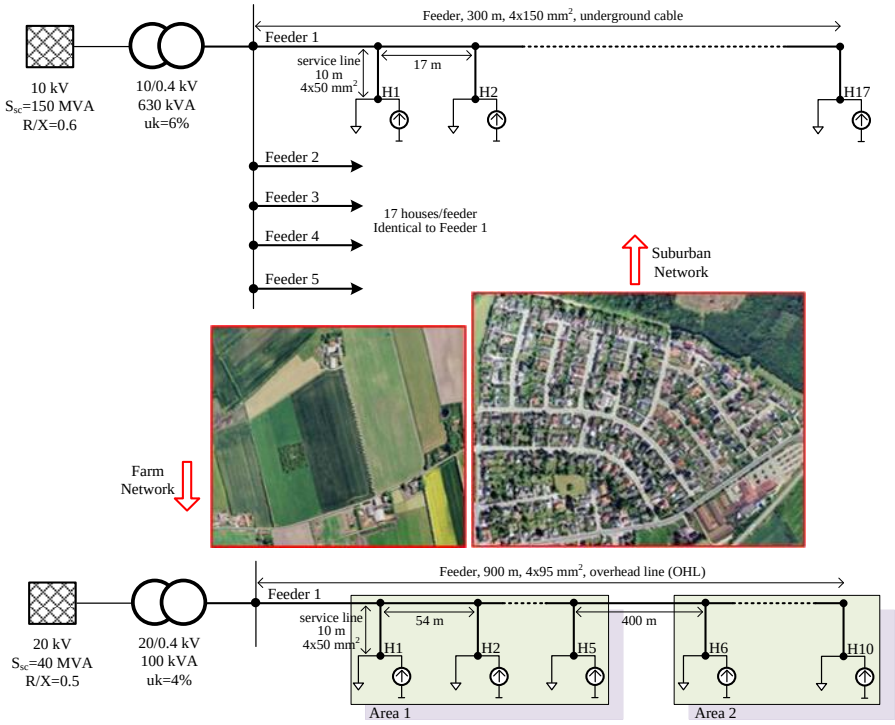

Fig. 4.9. Reference LV network models: Suburban (upper), farm (bottom)

It should be noted that farm networks are typically coupled to weak MV networks through the transformer. Furthermore, the short circuit power level decreases drastically at the end of their associated feeders due to long distance between the transformer and last consumer. Sensitivity analysis in the next subsection outlines the voltage sensitivity differences at suburban and farm networks in terms of the real and reactive power variations in the grid.

4.5 Voltage Sensitivity Analysis

Voltage sensitivity analysis can determine the effective network locations and the required amount of real-reactive power variations at these locations to control the grid voltage at desirable levels. In closed form, voltage sensitivity matrix (S_V) is computed by linearizing and solving two nonlinear power flow equations (4.11)-(4.12) in the vicinity of operation point. System Jacobian matrix (J) is updated at each iteration until

that certain convergence tolerance is satisfied. At the end, the Jacobian matrix is inverted to derive S_V matrix [4.18]. Figure 4.10 depicts two-bus power flow notations. U, δ, Y and θ denote phasor bus voltage, voltage angle, line admittance and impedance angle, in respectively.

$$P_i = |U_i| \cdot \sum_{j=1}^{n} |U_j| |Y_{ij}| \cos\left(\theta_{ij} - \delta_i + \delta_j\right) \tag{4.11}$$

$$Q_i = -|U_i| \cdot \sum_{j=1}^{n} |U_j| |Y_{ij}| \sin\left(\theta_{ij} - \delta_i + \delta_j\right) \tag{4.12}$$

$$\begin{bmatrix} \Delta\theta \\ \Delta U \end{bmatrix} = \begin{bmatrix} S_{\theta P} & S_{\theta Q} \\ S_{UP} & S_{UQ} \end{bmatrix} \begin{bmatrix} \Delta P \\ \Delta Q \end{bmatrix} \tag{4.13}$$

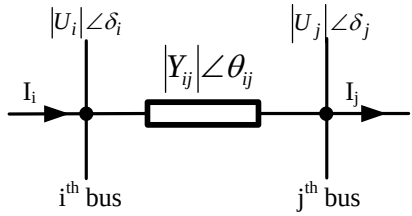

Fig. 4.10. Two-bus power flow representation

The diagonal terms of S_{UP} and S_{UQ} voltage sensitivity matrices are plotted in Fig. 4.11 for the suburban and farm network models under balanced power flow conditions. End of feeders of both networks are more resistive so, real power variation will give higher impact on the grid voltage level. On the other hand, PV connection points which are closer to the transformer (H1-H4) shows inductive dominant characteristics in farm networks due to the low R/X of the MV grid and transformer. Accordingly, the same amount of reactive power absorption by the inverters will cause higher voltage drops in farm networks (Fig. 4.11 bottom right).

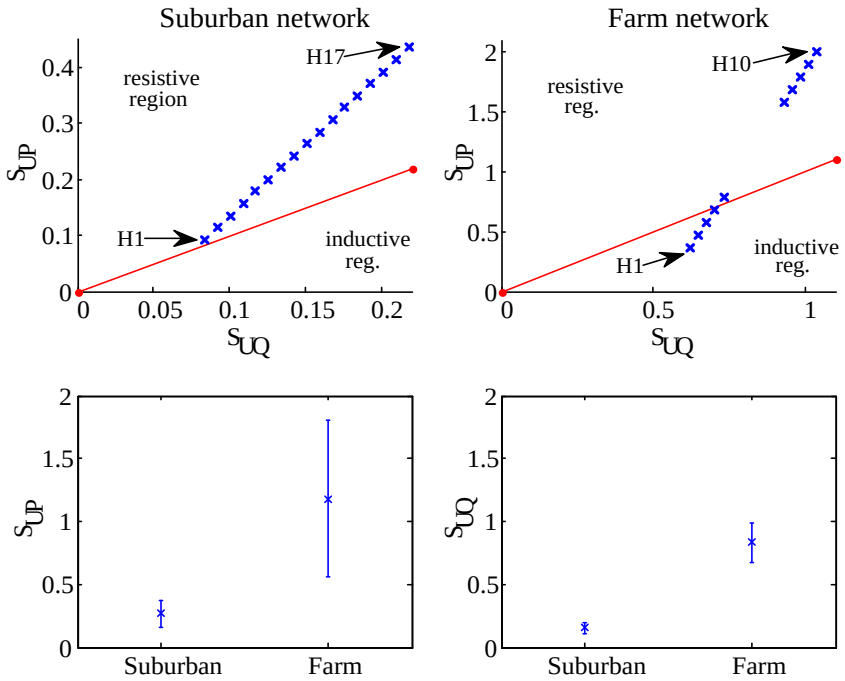

Fig. 4.11. Voltage sensitivity to real and reactive power variations for suburban and farm reference networks

4.6 Estimation of PV Hosting Capacity of LV Networks

PV hosting capacity implies the maximum amount of PV system connection to power networks without degradation of power quality. Even though grid voltage unbalance, network resonance, harmonic-flicker emissions and fault current contribution can limit connection of more PV system into the grid, steady-state overvoltage and thermal loading of MV/LV transformers and cables as the most emergency conditions will be taken into consideration here. Therefore, PV hosting capacity is estimated in such a way that real power output of each inverter is increased identically in 100-W steps as long as the network constraints are satisfied (Fig. 4.5). The worst-case hosting capacity is performed by neglecting power demand from the consumers in the networks under investigation. As shown from Table 4.4 and Fig. 4.12, PV hosting capacity at the farm reference network is considerably limited by the grid overvoltage condition due to having longer feeders but, higher voltage sensitivity to reactive power will enable more

effective voltage support compared to the suburban reference network. In suburban networks, since the transformer loading is a critical limitation, minimum amount of reactive power should be absorbed by the inverters during voltage support operation. Since PV capacity can only be increased by means of the transformer over sizing, it can be recommended that PV inverters connected to suburban networks should not utilize Q methods. Additionally, it is observed that line loading is not a considerable limiting factor for the both networks. In the next chapter, transformer thermal model will be also merged into the load flow simulation to estimate PV hosting capacity.

Table. 4.4. Maximum allowable PV connection per house (no reactive power)

	Suburban	Farm
Max. P_{PV} (kW/house)	7.7	6.9
Critical voltage(p.u.)	1.06	**1.1**
Trafo loading (%)	**101.8**	67.65
Line loading (%)	68.6	54
Limiting factor	Tr. overloading	Line overvoltage

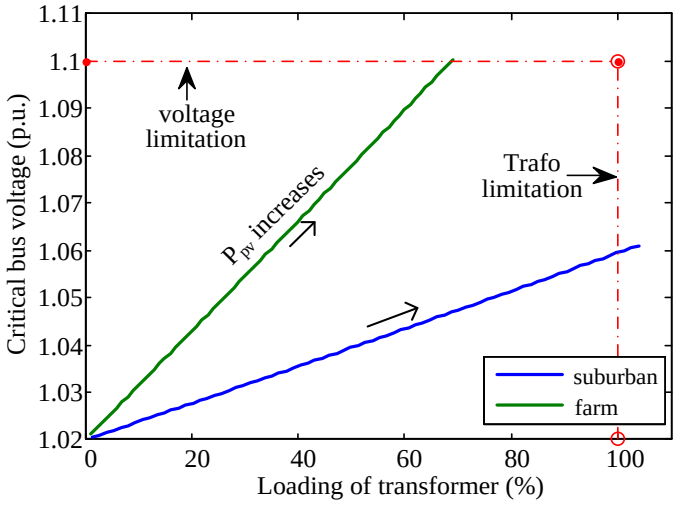

Fig. 4.12. Estimation of PV hosting capacity for the reference LV networks

4.7 Bibliography for Chapter 4

[4.1] *IEC Standard for Standard Voltages*, IEC 60038:2009.

[4.2] J. Schlabbach, K. H. Rofalski, *Power System Engineering: Planning, Design, and Operation of Power Systems and Equipments*, Wiley-VCH Verlag GmbH, 2008, ISBN 978-3-527-40759-0.

[4.3] E. Lakervi, E.J. Holmes, *Electricity Distribution Network Design*, 2nd Edition, IEE Power Series, 2007, ISBN 978-0-86341-309-4.

[4.4] A.A. Sallam, O.P. Malik, *Electric Distribution Systems*, IEEE Press Series on Power Engineering, 2010, ISBN 978-0-470-27682-2.

[4.5] *Voltage Characteristics of Electricity Supplied by Public Distribution Networks*, EN 50160 Standard, 2009.

[4.6] M.H.J. Bollen, F. Hassan, *Integration of Distributed Generation in the Power System*, IEEE Press Series on Power engineering, 2011, ISBN 978-0-470-64337-2.

[4.7] *4th Benchmarking report on quality of electricity supply*, Council of European Energy Regulators, 2008.

[4.8] *Requirements for the connection of micro-generators in parallel with public low-voltage distribution networks*, DS/EN 50438-2008.

[4.9] *Erzeugungsanlagen am Niederspannungsnetz - Technische Mindestanforderungen fur Anschluss und Parallelbetrieb von Erzeugungsanlagen am Niederspannungsnetz (Generators connected to the low-voltage distribution network - Technical requirements for the connection to and parallel operation with low-voltage distribution networks)*, VDE-AR-N 4105, Aug. 2011.

[4.10] *Technical Guideline on Power Generation Systems on Medium Voltage Networks—Guideline for Connection and Parallel Operation of Generating Plants to Medium Voltage Network*, Bundesverband der Energie- und Wasserwirtschaft e.V., Berlin, Germany, 2008.

[4.11] P. Bousseau, E. Monnot, G. Malarange, O. Gonbeau, "Distributed generation contribution to voltage control," *International Conference on Electricity Distribution (CIRED)*, Vienna, May 2007.

[4.12] G. Kerber, "Empfehlung zur Richtlinie zum Anschluss von Erzeugungs-anlagen an das Niederspannungsnetz (Recommendation on the policy for the capacity of generators connected to the low voltage networks)," Technical Report, Technical University of Munich, May 2009.

[4.13] *Loading Guide for Oil-immersed Power Transformers*, IEC 60076-7 Standard, 2005.

[4.14] J. Scheffler, "Bestimmung der maximal zulassigen Netzanschlussleistung photovoltaischer Energiewandlungsanlagen in Wohnsiedlungsgebieten," *Technische Universitat Chemnitz*, 2002.

[4.15] G. Kerber, R. Witzmann, "Statistische Analyse von NS-Verteilungsnetzen und Modellierung von Referenznetzen (Statistical distribution grid analysis and reference network generation)," *Jg. 107 (2008)*, Heft 6, S. 22-26.

[4.16] G. Kerber, R. Witzmann, H. Sappl, "Voltage limitation by autonomous reactive power control of grid connected photovoltaic inverters," in *Conference on Compatibility and Power Electronics*, pp. 129-133, May 20-22, 2009.

[4.17] M. Braun, K. Büdenbender, T. Stetz, U. Thomas, "Activation of energy management in households – The novel local consumption tariff for PV-systems and its influence on low voltage distribution grids," *International ETG Congress – Intelligent Grids*, Düsseldorf, October 2009.

[4.18] H. Saadet, *Power System Analysis*, McGraw-Hill, 1999.

Chapter 5
Increasing PV Hosting Capacity of LV Distribution Networks by means of New Reactive Power Control Methods

Maximum PV hosting capacity may be lower than the available solar potential of geographic area due to the network related limitations even though all rooftops can be fully occupied with PV modules. Therefore, it becomes more of an issue to know what exactly limits higher PV penetration level and which solutions should be engaged efficiently such as oversizing distribution transformer or using PV inverters with new grid support features. This chapter presents and examines the static reactive power ancillary services of PV inverters which are connected to LV distribution networks by giving attention to the grid voltage support and grid losses. Two reference LV networks as described in the previous chapter have been used to evaluate reactive power methods in order to increase PV hosting capacity and the most predominant limitations of connecting more PV inverters are emphasized for each network type. Certain part of a real LV distribution network of Braedstrup suburban area in Denmark is also used in simulation as a case study model. Thermal model of transformer is employed in this case study. Regarding of the MV/LV transformer overloading and grid overvoltage limitations, new local grid voltage support methods (*cosϕ(P,U)* and *Q(U,P)*) have been proposed. Resulting maximum allowable PV penetration levels with various reactive power methods are compared by load flow simulation.

5.1 Background

As the penetration of LV grid-connected renewable energy sources increases, possible integration problems such as voltage rise, overloading of network components, short-circuit capacity of networks, harmonic emissions, network resonance, proper operation of islanding detection methods and coordination of network protection relays come into question. The first two problems are more urgent issues to be solved. Once solar potential of region is fully utilized and connected to grid without overvoltage and component thermal limit violations, then the other remaining interaction problems can be focused to improve the network power quality by high penetration of PV systems.

In practise, potential solutions covering the network limitations can be summarized as following:

- Oversizing MV/LV transformers or replacing by a transformer having higher rated power,
- Increasing cross sections of overhead lines and/or underground cables, or adding new parallel lines/cables besides existing ones,
- Creating mesh topology in networks,
- Adopting step voltage regulators (tap changers) from HV/MV substations to the MV/LV transformers,
- Enforcing PV inverters to support grid voltage by means of their ancillary services such as reactive power control and real power limitation,
- Employing storage systems

In practise, network operators can prevent reverse power flow in the grid by limiting the number of PV inverter connections, allowing reactive power absorption, as well as requiring certain protection relay mechanisms from the inverters as briefly presented in the previous chapter regarding the voltage abnormal changes. Storage system usage and demand-side management are the other ways to further increase the penetration level, but only system owners can decide to put them into practise considering their individual economic benefit.

It is reasonable to benefit first from the available PV inverters that are connected to the grid for increasing their penetration level more. Reactive power capability of an inverter is mainly limited by the current carrying capacity of semiconductor switches. When the real power injection is less than the inverter rated power, remaining capacity can be utilized for the reactive power supply/absorption within predetermined power factor (*PF*) limits. New generation PV inverters are already oversized such that 0.9 *PF* can be preserved at the nominal real power injection for grid ancillary services.

As the grid voltage rises due to the reverse power flow in LV feeders, grid losses and power flow on the MV/LV transformer also tend to increase because distributed PV inverters throughout the network will start absorbing extra reactive power from the grid in order to reduce the grid voltage. Taking account of this, it is always desired to minimize total reactive power consumption without violating the overvoltage limit.

Various reactive power control methods without requiring communication infrastructures have been proposed so far in the literature. Droop control that is already employed in conventional power plants for power sharing and frequency support as primary control duty can remedy the grid voltage support mechanism of PV inverters [5.1]-[5.4]. The static reactive power droop curves are defined as piecewise linear equations in terms of either measured local voltage in 10-min average or measured output real power, and fixed droop settings are usually assigned to all inverters in the neighbourhood. Instead of applying the same droop settings for all inverters, a location-dependent adaptive *Q(U)* method is proposed in [5.4] for achieving higher voltage drop at the end of feeder. However, the inverter location information is obtained through the short-circuit impedance measurement at the connection point. A similar approach without impedance measurement has been proposed here such that only local variables, i.e., voltage and output real power, are utilized and processed.

The objective of this chapter is to propose a reactive power control strategy that is able to provide mainly the following targets to a feasible extent. First, the inverters should have certain level of coordination among each other to operate in the admissible grid voltage without a communication infrastructure by means of only measurable local

variables. Next, total reactive power absorption by the PV inverters should stay in minimum levels provided that the most critical bus voltage can be maintained inside the normal operation range. Finally, all the inverters belonging to the same feeder should participate on the voltage support mechanism when the critical bus voltage is above the limit value.

5.2 Standard Static Voltage Support Strategies with Reactive Power Control of PV Inverters

Standard reactive power strategies regarding 10-min average voltage variations can be mainly grouped as fixed reactive power (*fixed Q*), fixed PF (*fixed cos*φ), PF in terms of injected real power *cos*φ*(P)*, and local grid voltage dependent reactive power *Q(U)* [5.1]-[5.3]. Each of these methods is defined by using either a constant line and/or first-order piecewise equations that can be easily implemented in the inverter controllers and be modified remotely.

Fixed Q method will not be examined here because it requires a priori information of power flow variation profiles in time to estimate voltage rise for a known facility. General droop functions of the standard reactive power methods are illustrated in Fig. 5.1. x-axis shows the distance of PV installations along a feeder to the local transformer.

Compared with the *fixed Q* method, the generated reactive power is proportional to the real power for the *fixed cos*φ method (5.1), and it inherently starts controlling reactive power as long as the real power is produced. Accordingly, during the low irradiance level, the generated reactive power will also be as low as the real power by maintaining the proportionality equal:

$$\tan\varphi = \frac{Q}{P} = C1 \rightarrow Q = C1 \cdot P \tag{5.1}$$

where *C1* is a constant parameter. When the real power production is low, the potential risk of the grid overvoltage becomes smaller as well, since all produced real power then can be consumed locally without exporting excessive power to the MV network. In this

case, the reactive power control will unnecessarily create additional network losses. The *cosφ(P)* method can improve this drawback of the previous method by introducing two different power factor levels: *C1* and *C2* (Fig. 5.1-middle graph).

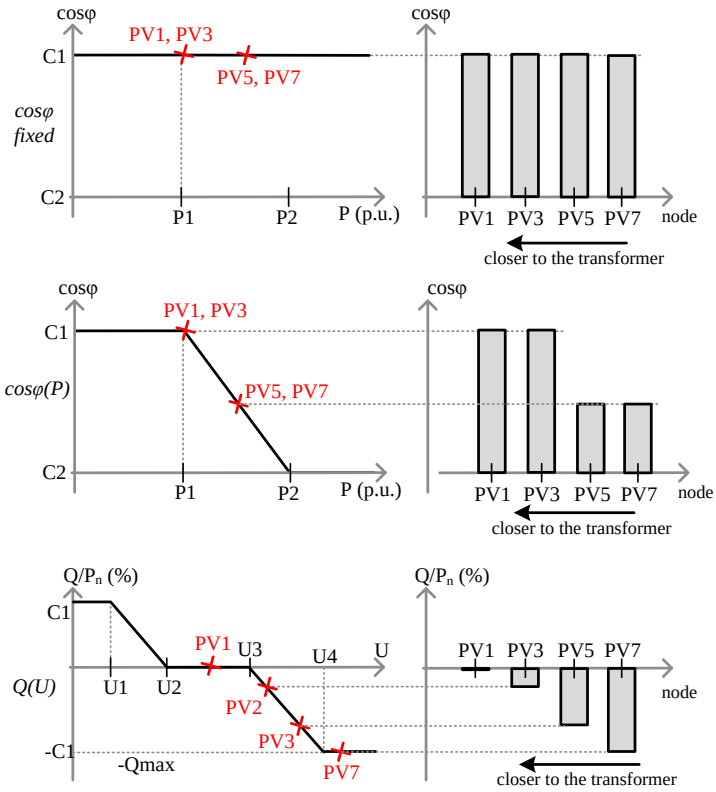

Fig. 5.1. Standard reactive power methods. (Upper) Fixed *cosφ*. (Middle) *cosφ(P)*. (Bottom) *Q(U)*

$$\cos\varphi = \begin{cases} C1, & P < P1 \\ \dfrac{C1-C2}{P1-P2}\cdot(P-P1)+C1, & P1 \le P \le P2 \\ C2, & P > P2 \end{cases} \tag{5.2}$$

The grid voltage is supported indirectly with the methods given so far by employing only local real power measurement as input. In all these methods, it is basically assumed that the grid voltage level increases with the produced real power from the PV

inverters, regardless of load variation. Nevertheless, when the high irradiance level coincides with the peak power demand, then simply the voltage rise may not reach to the critical value. The *Q(U)* method directly uses local voltage information that is a consequence of the power production and consumption in the neighbourhood as presented by (5.3).

$$Q=\begin{cases} Q_{\max}, & U<U1 \\ \dfrac{Q_{\max}}{U1-U2}\cdot(U-U1)+Q_{\max}, & U1\le U\le U2 \\ 0, & U2<U\le U3 \\ \dfrac{Q_{\max}}{U3-U4}\cdot(U+U3), & U3<U\le U4 \\ -Q_{\max}, & U>U4 \end{cases} \tag{5.3}$$

Hence, total reactive power absorption by the inverters can be considerably reduced within the cost of weaker voltage support compared with the *fixed cos*φ and *cos*φ*(P)* methods. In this context, weak voltage support or weak voltage coordination implies that reactive power contribution from the PV inverters that are nearest to the transformer will be negligible since the measured voltage levels at these inverters will be lower. There is a possibility to see no reactive power absorption from these inverters, although the voltage level at the end of feeder is above the limit value (see PV1 and PV7 on the bottom of Fig. 5.1). These advantages and drawbacks of the methods will be demonstrated with simulation of the reference LV farm network and a real network model in the following subsection.

5.3 Network Simulation and Performance Comparison of Standard Voltage Support Methods

Output real power of all 10 inverters located in the farm network (bottom of Fig. 4.9) is incremented with 100-watts steps and reference reactive power values are generated depending on the selected Q method. New PV hosting capacities with maximum 100% transformer loading level under different standard Q methods (*cos*φ*(P)* and *Q(U)*) are

eventually estimated and given in Table 5.1. The relevant static droop settings for this simulation are summarized as P_n*=10kW* (nominal power of the inverters), *P1=0.5 p.u., P2=1.0 p.u., C1=1.0, C2=0.9, Q1=1.0, U1=1.05 p.u., U2=1.1 p.u.*

Table. 5.1. PV hosting capacity of the farm network with maximum 100% transformer loading under different standard Q methods

	No Q	*cosφ(P)*	*Q(U)*
Max. Ppv (kW/house)	6.78	11.5	9.9
Transf. loading (%)	56.4	100	78.8

cosφ(P) method results in higher PV penetration level and transformer overloading becomes the main network limitation due to importing more reactive power as compared to *Q(U)*. Any voltage control actions on the upstream network such as tap changing at MV or LV substations cannot be identified by the PV inverters and they may continue importing reactive power unnecessarily. Another problem with *cosφ(P)* method is the load variation of the network. In some cases, real power produced by PV inverters may be consumed along the LV feeder without exporting it toward MV network. So, as a result of less severe reverse power flow, voltage rise will not be critical at all. As described in the voltage sensitivity subsection of Chapter 4, the inverters nearest to the transformer should absorb as much as lower reactive power due to less impact on the grid voltage. In this sense, *Q(U)* method inherently complies with minimum reactive flow and losses. However, maximum real power per house is limited at 9.9 kW although there is adequate room for the transformer loading. This can be explained by insufficient voltage support of the PV inverters nearest to the transformer although the critical node voltage violates voltage limitation.

A real suburban type LV distribution network has been also used to investigate different reactive power methods by simulating a sample day in 15-minute steps. Example LV grid, as shown in Fig. 5.2, is located in Braedstrup; a village in the region of Østyjylland, Denmark. Only one of the eight MV/LV transformers with its associated branches in the area has been modelled. The grid is radially operated but it has loop structure through normally open circuit breakers. A 400-kVA 10/0.4 kV Dyn1

oil-immersed power transformer is used to supply 60 residential consumers. The rest of the other grid parameters are summarized in Table 5.2. Currently, around 27 rooftops have already been occupied by different sizes of PV modules, but this PV penetration level is extended further in simulation; therefore, as a near future case, it is expected that all houses will have PV installations at the same rated power on their rooftops.

Table. 5.2. Summary of the grid characteristics

Grid characteristics	
Type of network	suburban
Type of settlement	residential
Number of houses	60
Type of houses	detached
Transformer rated power	400 kVA
Grid topology	Radially operated
Average distance between transformer and houses	415.5 m
Feeder cable types	Al 3x240, Al 3x150, Al 3x95 mm^2 underground
Service cable types (between houses and feeder connection points)	Al 50mm2 underground

Power production and consumption profiles measured during 2007 have been provided from another PV project named as Sol-300 that was initiated in 1998 [5.5]. Approximately 300 rooftop PV plants spreading to 8 geographical communities throughout Denmark were set up with total power capacity of 750 kWp in the project. Installed PV power capacity per unit is ranging between 0.9 and 6 kWp. Each unit was equipped with two separate energy meters for the monitoring of electricity production and consumption. Typical 15-min average power demand and production profiles that were required for the simulation of the suburban LV grid were obtained by averaging the arbitrarily chosen 100 houses. Fig. 5.3 shows the final average power profiles for two extreme months in 2007.

Fig. 5.2. Single transformer and its associated downstream connections of Braedstrup grid

In this thesis, PV penetration level (PL) is defined as ratio of annual energy production and annual energy consumption:

$$PL(\%) = \frac{\text{Annual total PV production (kWh)}}{\text{Annual total load consumption (kWh)}} \cdot 100 \qquad (5.4)$$

Average annual electricity consumption of approximately 100 family houses is calculated as 3748 kWh for the year of 2007. A similar amount (3358 kWh/year/household) has been also reported in EUROCO project [5.6] for the annual electricity consumption in Denmark. On the other hand, as a design consideration of PV system sizing experienced for Danish weather conditions, average 850 kWh/kWp electricity production for optimally inclined and oriented monocrystalline PV modules is expected to be injected from inverter [5.7]. Therefore, by using the previously discussed average power production profile data, 2140 kWh annual electricity has been

produced in 2007 that corresponds to 2.5 kWp installed PV capacity per household and finally it results in 57% PV penetration level for each household. In order to simulate more than 100% PV penetration scenario in the example grid, the original production profile data has been scaled up by the factor of 2.5. In this case, maximum produced peak real power injected to the grid reaches to 5 kW.

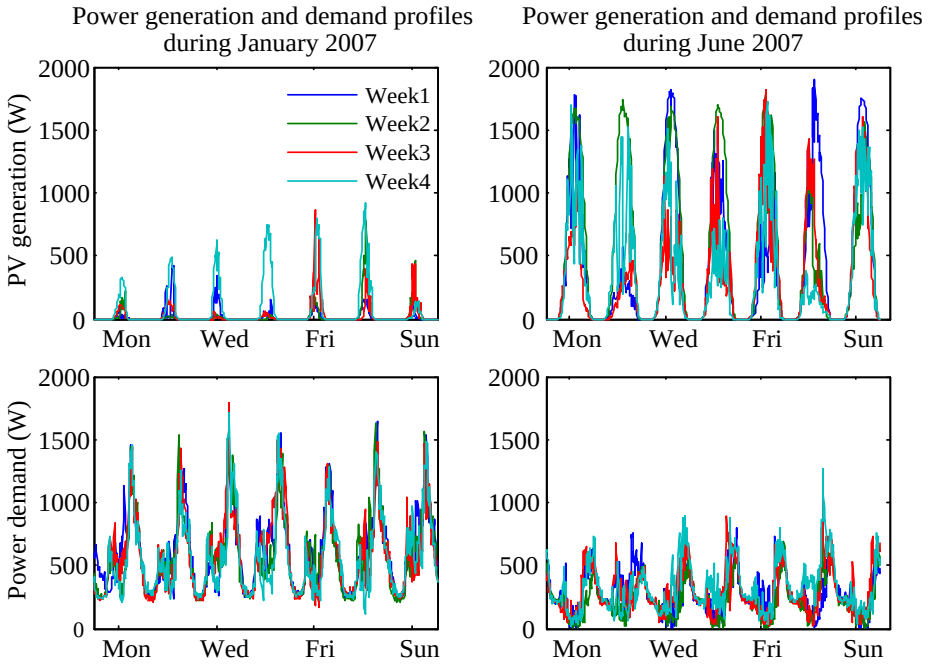

Fig. 5.3. Typical power demand and production profiles during January (left column) and June (right column) in 15-min time steps throughout Denmark

Afterwards, this typical power profile has been identically applied to each house in the grid model. Regarding the steady-state voltage variations and transformer overloading, the following assumptions were made:

1) Loads operate at unity PF.
2) All loads and inverters are constant PQ sources and are three-phase connected.
3) Balanced power flow at fundamental frequency (50 Hz) is considered.

A flowchart for the load flow script was developed as shown in Fig. 5.4. Rate of change limiter was also required to numerically damp *Q* oscillations among the inverters.

Reactive power generation on the 3rd of June in 2007 that is associated with *cosφ=0.9*, *cosφ(P)*, *Q(U)* methods at two different locations PV1 (next to the transformer), PV60 (the furthest away node) and the corresponding voltage variation of PV60 are depicted in Figs. 5.5 and 5.6, respectively. The main difference between *Q(U)* and the other methods is that *cosφ=0.9* and *cosφ(P)* methods generate location-free reactive power references. The same amount of reactive power is absorbed by PV1 and PV60, and therefore, better voltage support has been achieved with these methods. One superior performance of *cosφ(P)* over *cosϕ=0.9* method is that less reactive energy is consumed by the inverters (see Fig. 5.5). On the other hand, when all inverters are employed with *Q(U)* method, then PV1 does not participate on the voltage support due to its low local voltage. Accordingly, total reactive power consumption is considerably reduced but this time the voltage at PV60 approaches to the 1.1 p.u.

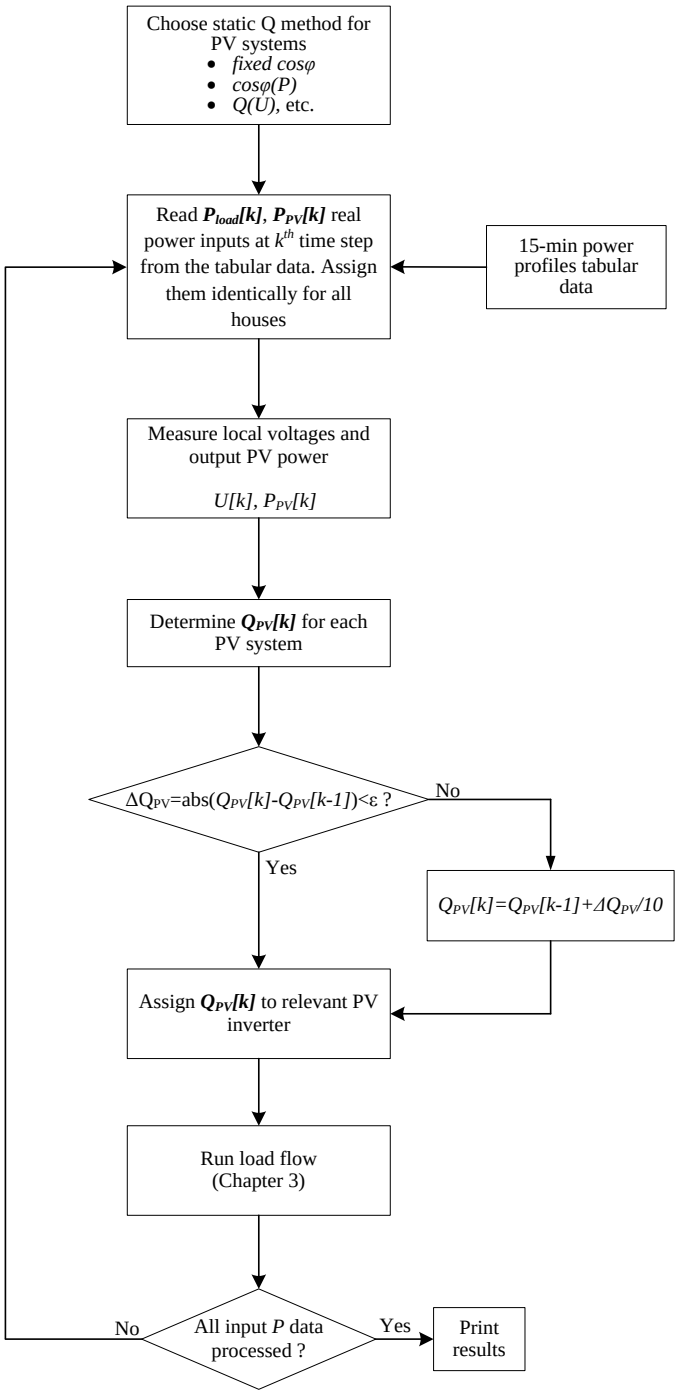

Fig. 5.4. Flowchart of load flow including reactive power services from PV inverters

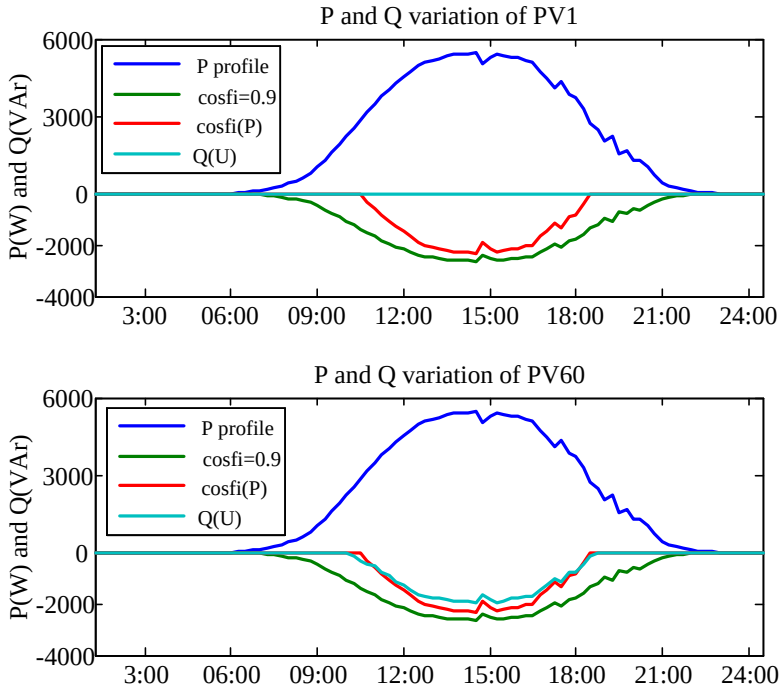

Fig. 5.5. Reactive power generation at PV1 and PV60 by different reactive power methods during June 3, 2007

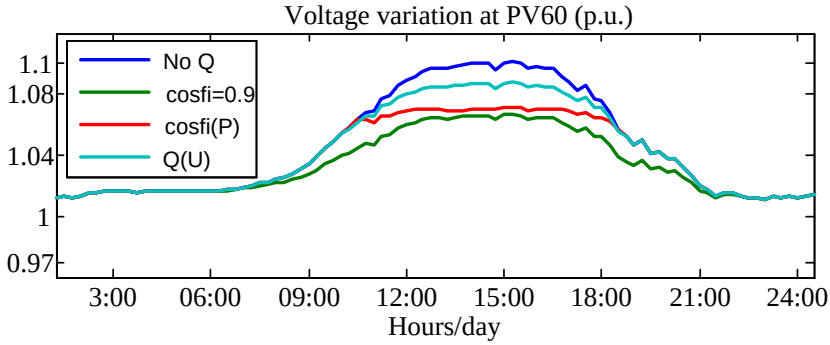

Fig. 5.6. Voltage variations at PV60 with different reactive power methods during June 3, 2007

5.4 New Reactive Power Methods and Performance Comparison with the Standard Methods

As discussed previously, *fixed* cosφ and *cosφ(P)* methods indirectly support the grid voltage in such a way that grid voltage will increase due to the real power injections from the inverters; accordingly, higher reactive power absorption should be exploited to compensate the voltage rise. However, this statement is certainly valid only when power demand from the consumers is neglected. If local power demand is compensated partly by the PV inverters, then all produced real power by the inverters does not flow towards the upstream network or severe grid voltage rise may not exist in the feeders. Therefore, voltage variation is actually coupled to the consumer load profiles. Main drawbacks of real power dependent *Q* methods such as *fixed* cosφ and *cosφ(P)* are:

- Unnecessarily absorbing reactive power when the produced real power is consumed locally and, as a result, the grid voltage is in admissible range.
- Voltage sensitivities are not taken into consideration. The inverters with the least voltage sensitivity and with the highest voltage sensitivity may utilize the same amount of reactive power (Fig. 5.7).

On the other hand, since the voltage dependent *Q* method, *Q(U)*, directly uses local voltage information, the amount of reactive power from the PV inverters will be proportional to the voltages measured at the local points as shown at the bottom of Fig. 5.7. In this case, the inverters closer to the transformer may not react to the overvoltage emergency condition that is occurred at the end of feeders.

Regarding these drawbacks of the standard Q methods, following modifications are proposed:

- Power factor level of the nearest inverters to the transformer should be increased at certain amounts for *fixed* cosφ and *cosφ(P)* methods,
- Reactive power amount of the inverters nearest to the transformer should be increased for *Q(U)* method.

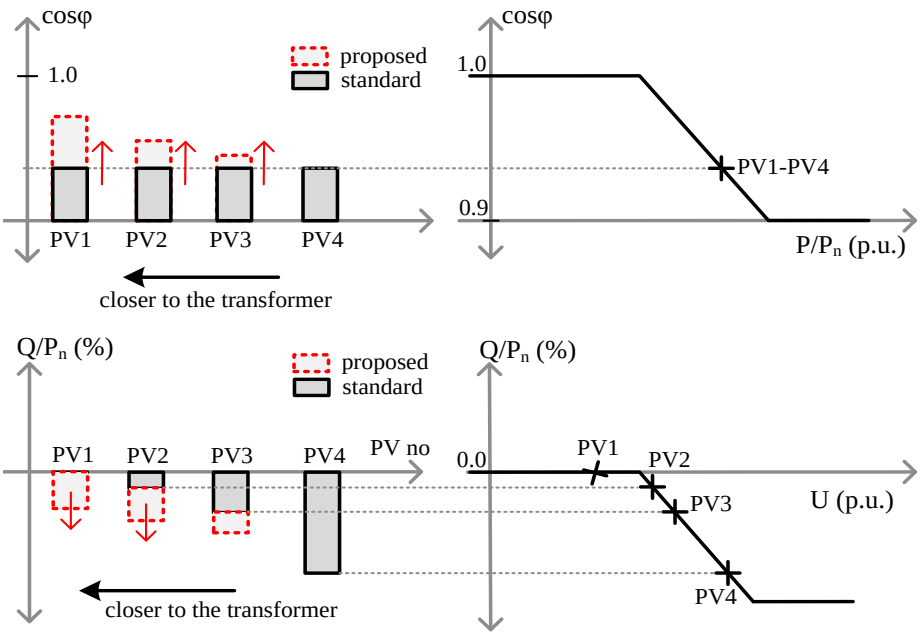

Fig. 5.7. Static droop curves of different reactive power methods: *cosφ(P)* (upper), *Q(U)* (bottom) for a radial feeder. PV1 is the inverter nearest to the transformer

Fig. 5.8 illustrates the associated two static curves of the proposed *Q(U,P)* method which can be integrated on the inverters with identical parameters. Q starting voltage *U1* is deviated in a predetermined limited band in terms of the measured output real power (*U1(P)*) by maintaining the slope parameter constant.

Fig. 5.9 and Table 5.3 depict the load flow simulation results with new reactive power methods applied to the reference LV farm network developed in Chapter 4. Relevant droop parameters used in the simulation are as following: $U1_{min}=1.02$ p.u., $U1_{max}=1.05$ p.u., $U2=1.1$ p.u. and $PF_{lim}=0.9$ (minimum power factor).

Compared to the *Q(U)* method, *Q(U,P)* achieves more PV hosting capacity. If *P* dependent Q method such as *cosφ(P)* is utilized, the proposed *cosφ(P,U)* method can

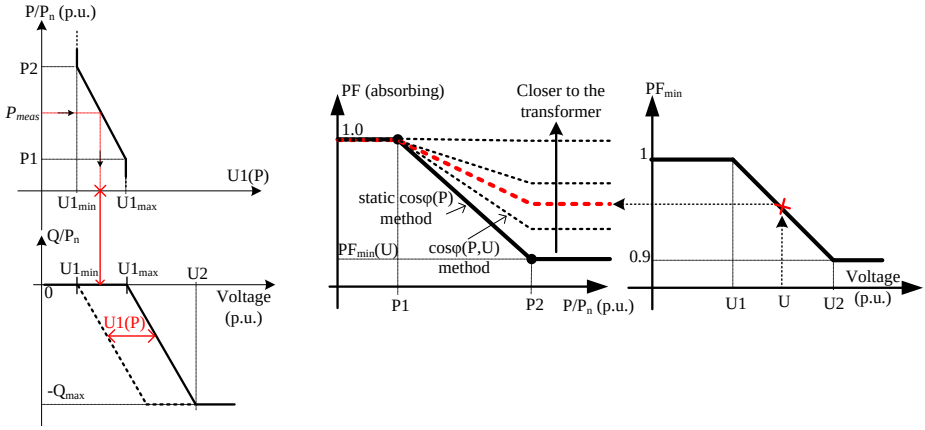

Fig. 5.8. Proposed Q methods: *Q(U,P)* (left), *cosφ(P,U)* (right) for a radial feeder. PV1 is the inverter nearest to the transformer

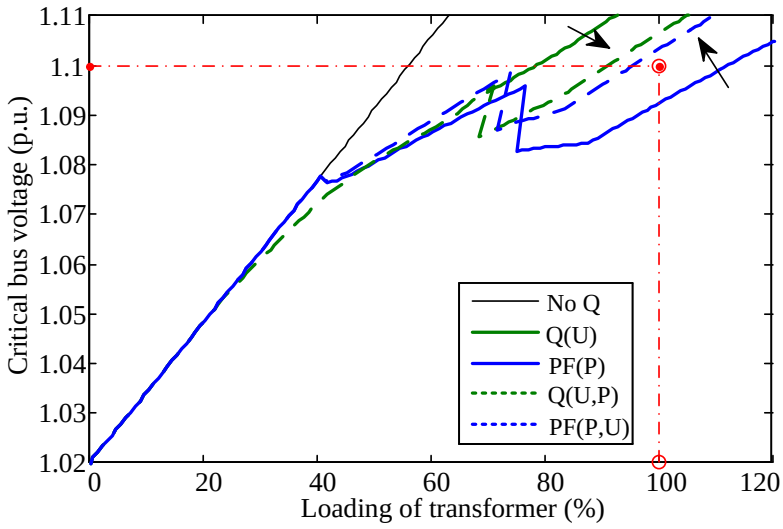

Fig. 5.9. Network constraints of the farm network under different Q methods

ensure less reactive power absorption from the MV grid. It also results in less transformer loading and thus, allows increasing the PV hosting capacity more in the network.

Table. 5.3. PV hosting capacity of the farm network with maximum 100% transformer loading under different standard Q methods including the proposed ones

	No Q	*Q(U)*	*Q(U,P)*	*cosφ(P)*	*cosφ(P,U)*
Max. P_{pv} (kW/house)	6.78	9.9	11.1	11.5	11.5
Tr. Loading (%)	56.4	78.8	91.4	100	95.9

In addition to the reference LV farm network, the proposed *cosφ(P,U)* method is also implemented in the Braedstrup suburban network. This time, transformer thermal model is integrated into the load flow simulation. Table 5.4 presents total grid losses and transformer loss of life with average ambient temperature of 15.8ºC. By this way, estimated PV hosting capacities with two results considering the nominal power and maximum hot-spot temperature (98ºC) as the two transformer overloading limits are given in Table 5.5 and 5.6.

Table. 5.4. Monthly analysis result from 1 to 30 of June 2007 for Braedstrup network

	Network active power losses (MWh/June)	*Trafo Loss of Life (minutes) for non-upgraded insulation paper*	*Trafo Loss of Life (minutes) for thermally upgraded insulation paper*
No Q	1.861	33.8	4.3
cosφ=0.9	2.164	47.9	7.4
cosφ(P)	1.979	40.4	5.8
cosφ(P,U)	1.932	36.6	4.9

Table. 5.5. PV hosting capacity of Braedstrup network under different reactive power methods without transformer thermal model

	Max. Ppv (kW/house)	Trafo loading (%)	Critical bus voltage (p.u.)
No Q	5.2	74.6	**1.1**
cosφ=0.9	6.3	**101**	1.074
cosφ(P)	6.5	**101**	1.079
cosφ(P,U)	6.8	**101**	1.086

Table. 5.6. PV hosting capacity vs. transformer hot-spot temperature for 25°C ambient temperature

	Max. Ppv (kW/house)	Max. hot-spot temp. (°C)	Trafo loading (%)	Critical bus voltage (p.u.)
No Q	5.2	61.4	74.6	**1.1**
cosφ=0.9	8.25	**98.1**	130	1.087
cosφ(P)	8.3	**98.1**	131	1.087
cosφ(P,U)	8.75	**98**	130	1.098

It can be concluded that, by utilizing transformer hot-spot temperature model adopted from IEC 60076-7, PV hosting capacity can be increased further (68% higher compared to that of 100% overloading limit) without notably degrading transformer life. It is shown that thermally upgraded insulation paper can be an alternative solution for higher PV hosting capacity by permitting the transformer to operate beyond 98°C of hot-spot temperature during only certain hours per day.

5.5 Laboratory-scaled Test Feeder with Multiple PV Inverters

In this subchapter, a small-scale experimental setup has been built in order to study grid interaction issues of PV inverters. The following technical topics are aimed to investigate them in the laboratory conditions:

- Control of PV inverters (MPPT, current controllers, grid monitoring, etc.),
- Grid voltage rise problem and voltage support coordination between inverters without any communication link
- Power quality problems such as harmonic emissions, network resonance, flicker, etc.

5.5.1 Selecting suitable series impedance for creating overvoltage event

Single-line diagram of the setup is illustrated in Fig. 5.10. Three inverters rated at 2.2 kVA in 3-phase were used and operated as PV inverters. Impedance boxes contain 3-

phase series connected resistors and reactors in order to emulate real feeder impedance. The values of 3-phase series resistors and reactors were determined in such that 1.1-p.u. voltage level at PV3 can be reached with full real power injections from the inverters. So, voltage rise equation derived in (4.1) can be rewritten as:

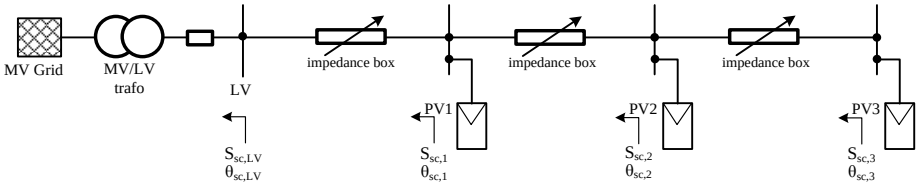

Fig. 5.10. Single-line diagram of the laboratory setup

$$V_{PCC} = |V_G| + \frac{R \cdot P + X \cdot Q}{|V_G|} + j \cdot \left(\frac{X \cdot P - R \cdot Q}{|V_G|} \right) \tag{5.5}$$

If (5.5) is interpreted in terms of short-circuit power, impedance angle, and power factor angle at each location, voltage rise (in %) with respect the nominal grid voltage for lagging power factor becomes:

$$\frac{\Delta V}{|V_{PCC}|} = \frac{1}{SCR} \cdot \left[\cos(\varphi - \theta) + j \cdot \sin(\theta - \varphi) \right] \tag{5.6}$$

where *SCR* is defined as short-circuit capacity ratio (S_{SC}/S_{base}), φ is the angle between local voltage and injected current, θ is the impedance angle. Thus, suitable impedance values can be calculated in such a way that desired voltage rise is obtained at the terminals of PV3. Approximately 1.1 p.u. voltage is estimated with following resistance and reactance values by maintaining R/X=2.5 (Table 5.7): $R_1=1\Omega$, $R_2=1.2\Omega$, $R_3=1.5\Omega$, $X_1=0.4\Omega$, $X_2=0.48\Omega$, $X_3=0.6\Omega$. In final version of the impedance boxes, 6-tap adjustable resistors and reactors was produced:

Table. 5.7. Voltage rise emulation at each connection point

Connection points	**1** $[\Delta V\,\%]$	**2** $[\Delta V\,\%]$	**3** $[\Delta V\,\%]$
only PV1	1.438	1.438	1.438
only PV2	1.438	3.203	3.203
only PV3	1.438	3.203	5.419

PV1+PV2+PV3	**4.314**	**7.844**	**10.060**

1) Variable resistors with 6 taps: 0.3-0.6-0.8-1.0-1.3-1.5 Ω/phase
2) Variable inductors with 6 taps: 1.2-1.5-1.7-1.9-2.1-2.5 mH/phase

Thus, two cases, "*more resistive*" (R/X=1.64 at PV3) and "*less resistive*" (R/X=1.24 at PV3), have been implemented by changing tap settings of the impedance boxes. Measured impedance values, impedance angles and short-circuit power for the two cases are given in Table 5.8. P-Q variation method has been implemented to estimate the impedance values seen by the individual inverters [5.8].

Table. 5.8. Impedance measurements seen by each inverter in the lab setup

Case 1 (more resistive)				
	LV	**PV1**	**PV2**	**PV3**
Rsc (Ω)	1.06	3.093	4.187	5.546
Xsc (Ω)	0.6	2.077	2.654	3.374
R/X	1.767	1.489	1.578	1.644
Zsc (Ω)	1.218	3.726	4.957	6.492
Ssc (kVA)	**131.4**	**42.9**	**32.3**	**24.6**
θsc (°)	**29.51**	**33.82**	**32.37**	**31.31**
Case 2 (less resistive)				
	LV	**PV1**	**PV2**	**PV3**
Rsc (Ω)	1.153	3.38	4.375	5.313
Xsc (Ω)	0.692	2.546	3.49	4.291
R/X	1.666	1.328	1.254	1.238
Zsc (Ω)	1.345	4.232	5.596	6.829
Ssc (kVA)	**119**	**37.8**	**28.6**	**23.4**
θsc (°)	**30.97**	**36.99**	**38.58**	**38.93**

5.5.2 PV control structure

Grid integration studies of PV inverters, firstly, require stable operation of inner current loop controllers. Overall controller scheme used for each 3-phase PV inverter is

illustrated in Fig. 5.11. The inner current loop is regulated by two identical Proportional + Resonant (PR) controllers in stationary reference frame. Controller gains are determined according to the transfer function of LCL output filter including time delays. More specific data for identical inverters is given as following:

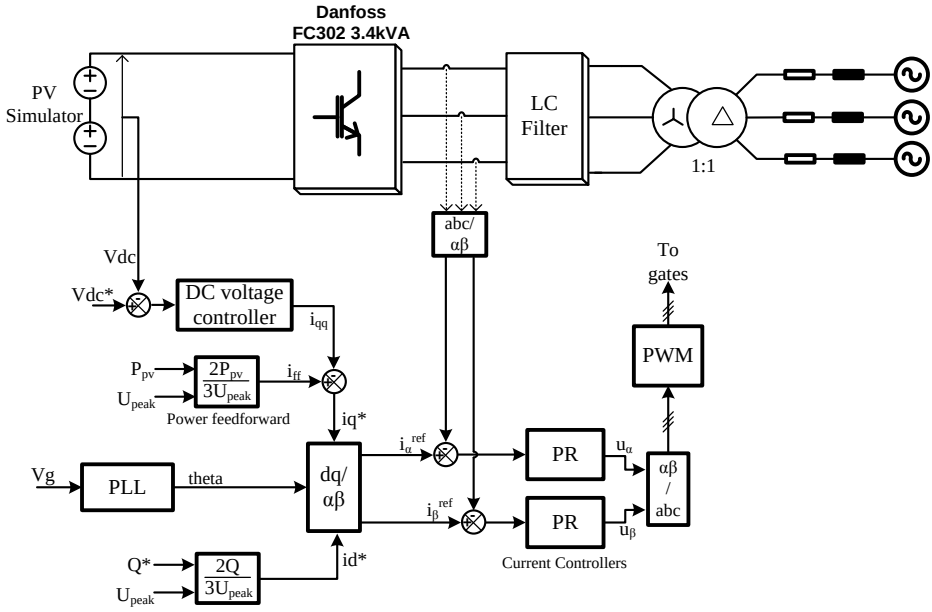

Fig. 5.11. Controller scheme of 3-phase inverter used in the setup

1) 3-phase full-bridge 2.2 kVA,
2) 8 kHz switching frequency, SPWM+3rd harmonic injection modulation,
3) Inverter side filter inductance is 6.9 mH, filter capacitor is 4.7 μF, transformer leakage inductance is 2.5 mH, and accordingly LCL filter resonance frequency becomes 1.7 kHz.

Step response result of reactive power with constant real power is shown in Fig. 5.12. Decoupling of real and reactive power was satisfied.

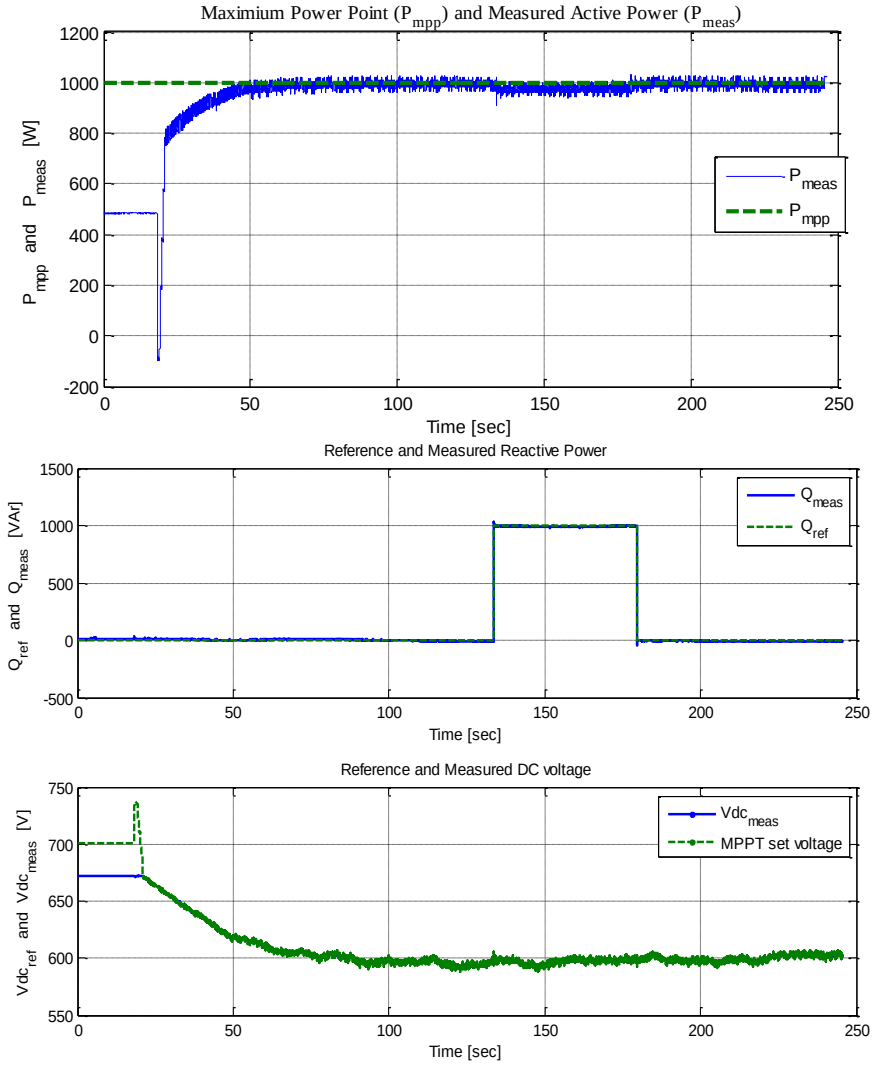

Fig. 5.12. Experimental results of single PV system. MPPT is activated at 21st second. P_{MPP} =1kW, V_{MPP}=590V, G=1kW/m2. DC voltage controller gains: K_P=0.35. Current controller gains: K_P=12, K_{i1}=3000, K_{i5}=K_{i7}=1000 (5th and 7th resonant integrator gains)

5.5.3 PV simulator and MPPT

As long as open circuit voltage (V_{OC}), short-circuit current (I_{SC}), maximum power point voltage (V_{MPP}) and current (I_{MPP}) are specified from PV panel datasheet, (5.7) can be implemented as a slower task compared to switching frequency of 8 kHz [5.9].

$$V_{PV} = N_{PS} \cdot V_{OC} + N_{PS} \cdot N_S \cdot V_T \cdot \ln\left(1 - \frac{i}{I_{SC,1000} \cdot \frac{G}{1000}}\right) \tag{5.7}$$

where N_{PS} is the number of series connected panels, N_S is the number of series connected cells in each panel, V_T is thermal voltage constant.

PV simulator has been built by two identical programmable DC power supplies. MPPT task has been implemented by means of Perturb-and-Observe (P&O) method. The sampling frequency of MPPT has been selected as 2 Hz and the voltage increment is set to 2 V.

5.5.4 Implementation of reactive power methods

When reactive power methods were under investigation, PV panel model was disabled and DC power supplies were set to constant DC voltage mode for the simplification. So, real power and reactive power set values are the only specified inputs. Minimum power factor was limited at 0.9 and all impedance taps were initially positioned at 6. PV1, PV2 and PV3 were connected at and energized the lab feeder respectively. Real power curtailment against to overvoltage condition was also integrated into the controller structure as *V* dependent *P* droop curve.

Measured voltage and injected real power at PV3 are depicted in Fig. 5.13. It can be noticed that voltage change at PV3 is the higher when PV3 is connected and voltage rise at PV3 is resulted in minimum level when PV1 is connected to the grid. This can be explained by voltage sensitivities to real power. At 38th second, real power curtailment is enabled for PV3 and the steady-state voltage converges to around 1.09 p.u. But, real power sharing among PV inverters will become unfair in this case.

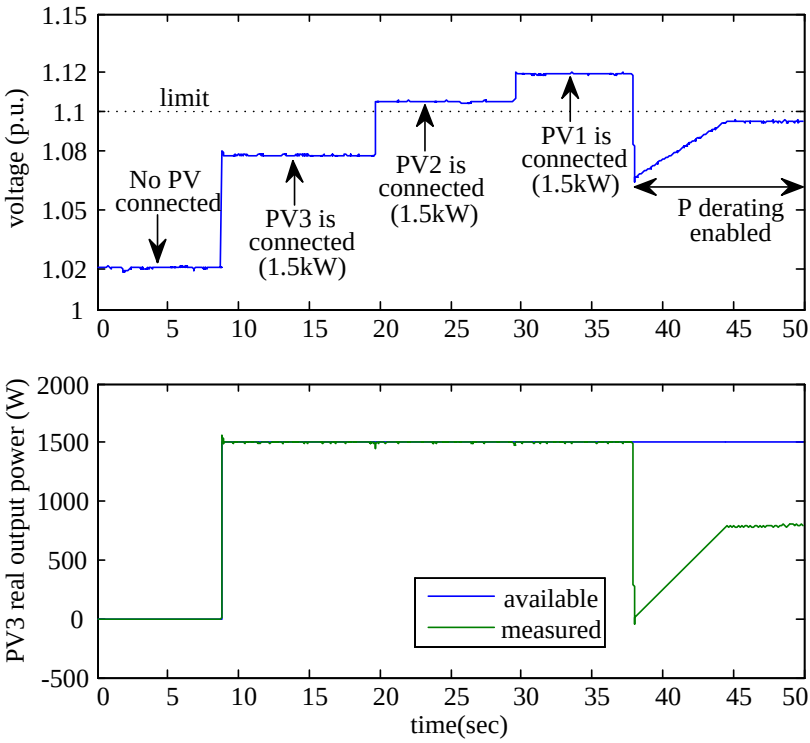

Fig. 5.13. Measured voltage (top) and injected real power (bottom) at PV3

Fig. 5.14 presents voltage and reactive power variations for PV1 and PV3 under different reactive power methods. Between 10s and 20s, Q3 is less than Q1 due to real power curtailment of PV3. This is undesirable condition with *cosφ(P)* method. As the real power of PV3 is reduced, the associated reactive power also decreases because of the constant proportionality of *cosφ*-type methods. Eventually, voltage support by PV3 cannot be fully exploited. On the other hand, *Q(U,P)* method is more effective on the first inverter (PV1). The proposed method forces PV1 to absorb more reactive power between 30s-50s.

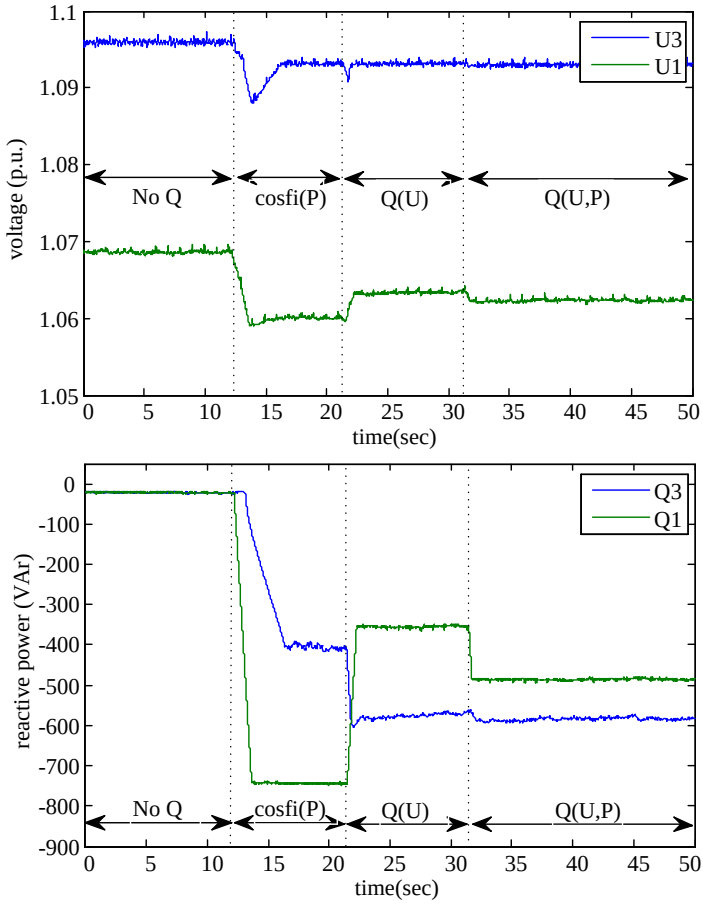

Fig. 5.14. Measured voltage (top) and reactive power (bottom) at PV3

Fig. 5.15 illustrates effects of cable R/X ratio on the grid voltage support and real power curtailment was disabled this time.

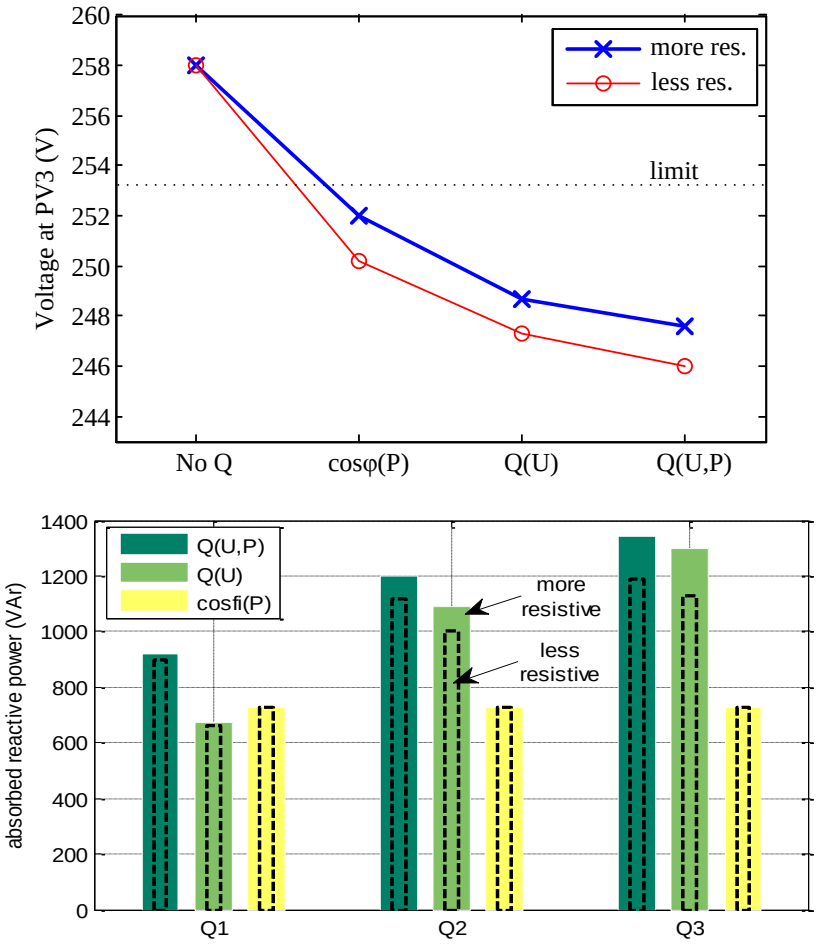

Fig. 5.15. Effect of cable R/X ratio on the voltage support by means of reactive power (*P* curtailment is disabled)

5.5.5 Summary

Following conclusions can be reported:

1) Regarding of the *more resistive* networks, higher amount of reactive power is required to lower the grid voltage.
2) *Q(U,P)* method can help on the voltage rise problem with high penetration of PVs especially at *more resistive* networks.

3) All local Q methods may cause unnecessary Q absorption from the grid. They cannot guarantee maintaining the grid voltage in admissible range. However, *Q(U,P)* method performs better in this sense, because the inverters nearest to the transformers are forced to increase their Q set values.
4) Only Q method with a communication link can achieve optimum Q dispatch among PV inverters.

5.5.6 Bibliography for Chapter 5

[5.1] M. Braun, T. Stetz, T. Reimann, B. Valov, and G. Arnold, "Optimal reactive power supply in distribution networks – Technological and economic assessment for PV systems," *24th European Photovoltaic Solar Energy Conference*, Hamburg, September 2009

[5.2] M. Braun, "Reactive power supply by distributed generators," *IEEE Power Energy Soc. Gen. Meeting*, pp. 1-8, July 2008

[5.3] J. Backes, C. Schorn, and H. Basse, "Cost-efficient integration of dispersed generation using voltage dependent reactive power control," *CIRED Workshop*, Lyon, France, 2010.

[5.4] G. Kerber, "Umrichter und Steuerverfahren fur einen Umrichter," Eur. Patent EP 1 906 505A 1, April 2, 2008.

[5.5] IEA-PVPS_Task 10 Report. Community-Scale PV: Real examples of PV based housing and public developments. [Online]. Available: www.pvdatabase.org/pdf/Sol300.pdf

[5.6] EUROCO Project Report. Demand-side management: End-use metering campaign in 400 households of the European community – Assessment of the potential electricity savings. January 2002.

[5.7] PV-OPT Project Report. Optimization of design of grid-connected PV systems under Danish conditions. April 2009.

[5.8] A.V. Timbus, P. Rodriguez, R. Teodorescu, M. Ciobotaru, "Line impedance estimation using active and reactive power variations," *Proc. of PESC*, pp. 1273-1279, 2007.

[5.9] D. Sera, T. Kerekes, R. Teodorescu, F. Blaabjerg, ”Improved MPPT method for rapidly changing environmental conditions,” in *IEEE International Symposium on Industrial Electronics,* vol. 2, pp. 1420-1425, July 2006.

Chapter 6
Conclusion

This chapter gives a summary of the work addressed in the previous chapters based on the obtained results. Future study direction is also presented at the end of the chapter.

6.1 Summary

The main focus of this thesis is to investigate and analyse local voltage support strategies provided by PV inverters in order to increase PV hosting capacity of LV distribution networks. Reactive power control and real power reduction are essential ancillary services of PV inverters for this purpose although other remedial actions in the distribution networks can be practised as well. When and how much reactive power commanded to individual PV inverters were initial questions to be answered.

In Chapter 2, some PV integration problems have been briefly summarized and voltage rise has been identified as the major challenging problem. Once the PV penetration level is maximized, the other voltage quality issues can be taken into consideration. From voltage rise perspective, three main grid codes (EN 50160, EN 50438, and VDE-AR-N 4105) have been examined. Only VDE-AR-N 4105 addresses network "planning stage" so that network analysis becomes a must to estimate voltage rise before PV systems are installed. The other grid codes cover only network "operation stage". Reactive power supply and real power reduction requirements forced by VDE-AR-N 4105 have been concentrated and explained in more details. Fixed cosφ, fixed Q and cosφ(P) methods are referred in the grid code; however, which method and what

parameters exactly will be used are still an open question. Network operators have to choose one of these methods with optimum parameters according to specific LV network. Furthermore, some proposed state-of-the art strategies from the literature have been presented.

In Chapter 3, a three-phase unbalanced load flow simulation tool has been developed for estimation of maximum PV hosting capacity of LV radial distribution networks taking into consideration of voltage rise and equipment overloading limitations for future studies. In reality, residential applications of single-phase PV systems have widespread use in 230/400-V networks and obviously require three-phase load flow analysis. Although it is not suitable for solving meshed or ring networks, backward-forward sweep method was selected as load flow solver due to providing better (guaranteed) convergence performance compared to those of Gauss-like and Newton Raphson based methods. A breadth-first search algorithm based bus ordering scheme has been described and scripted. Modelling of network components (line/cable, load, 2-winding transformer, voltage regulator) has been revised in 3-phase coordinates. The simulation tool has been validated through 4-bus test feeder and 13-bus test network by comparing obtained voltage mismatches within tolerable errors. Maximum of 0.2% voltage mismatch was observed on the IEEE 4-bus test feeder while the overall mismatches take place in the level of 0.1-2% for IEEE 13-bus network. The voltage mismatches can be reduced further if maximum number of iteration is limited to higher numbers.

In Chapter 4, general considerations on network planning and operation have been briefly summarised from PV integration perspective. A transformer thermal model based on hot-spot temperature estimation has been adopted from IEC 60076-7. Thus, it is shown that distribution transformers can be further overloaded (130% of nominal power) shortly without violating 98°C of hot spot temperature. More accurate estimation of PV hosting capacity should include transformer thermal model. The other addressed issues were network limitation factors against increasing PV penetration level that can differ depending on network structures. Therefore, LV critical reference network models have been revised and characterized. Voltage sensitivity analysis

showed that farm and rural networks exhibit more inductive equivalent impedance seen from PV system connection points. This characteristic allows the PV inverters controlling reactive power more efficiently for voltage rise compensation. Also, the PV inverters located at the furthest point along the feeder are capable of reducing the grid voltage more effectively compared to those of located near transformer. Deducing from the voltage sensitivity analysis, optimised reactive power control methods can be developed. In the end of this chapter, suburban and farm LV reference networks have been analysed with load flow solution for estimating their maximum PV capacities (7.7kW/house for suburban and 6.9kW/house for farm network). The main limiting factor of suburban network was transformer loading limit whereas PV penetration was essentially limited by the overvoltage limitation in the farm network.

Chapter 5 has been dedicated to examination of the static reactive power ancillary services of PV inverters which are connected to LV distribution networks by giving attention to the grid voltage support and grid losses. However, this ancillary service of PV inverters is obviously limited in distribution networks. The main reasons are high R/X ratio of LV networks, PV inverter's current limitation, distribution transformer and cable/line thermal limits with increased reactive power flow. Accordingly, maximum voltage drop should be realized with minimum reactive power absorption from the grid. Important drawbacks of voltage support strategies which were already imposed by grid codes have been underlined in this chapter and based on this, two new methods have been proposed. New Q control methods have been inherited from standard *cos(φ)* and *Q(U)* methods by combining their properties in order to prevent unnecessary reactive power absorption from the grid during admissible voltage range or to increase reactive power contribution from the inverters during grid overvoltage condition. Load flow simulation and lab-scaled experimental validation of these methods have been successfully shown in the end of this chapter.

6.2 Future work

Some important improvements should be added on the work presented here. So, the summary of future work can be listed as following:

A LV network database can be specifically established for Danish case. Certain number of sampled LV distribution networks should allow statistically generating main characteristics of these networks such as average length of feeders, average load density, typical cable sizes and transformer capacity, etc. Based on these results, the most critical network models can be developed and optimum parameters of static Q droop functions can be determined.

In addition to statistical LV network models, Monte Carlo simulation can be carried out to quantify number of overvoltage and overloading violations during one year. This result obviously gives more concrete understanding of the impacts of various static Q control methods on PV penetration level by PV system owners and network operators.

Transformer thermal model has proved that PV hosting capacity can be estimated more accurately. Similarly, cable thermal models, especially for the cables placed at the most critical branches, can be utilized during load flow solution.

Power curtailment method against overvoltage condition was shortly explained in this work. However, various droop parameters of a power curtailment curve should be considered and the best suitable parameters specific to every LV network classes can be investigated with the aim of achieving highest PV energy yield for a year.

Another interesting future work is the determination of PV inverter losses owing to extra Q support. Since the amount of Q absorption of individual PV inverter depends on static Q control method and its connection point (or distance to the transformer), unequal energy losses will be expected among PV inverters. If necessary, different Q droop parameters can be assigned to individual PV inverters in order to maintain unequal loss sharing at minimum level.

Lastly, new optimum Q and P dispatching algorithms can be developed by utilizing communication infrastructure between PV inverters and main control station. IEC 61850 is a promising, vendor-free protocol and can be used to optimally control voltage

levels at LV feeders. This protocol can be embedded into the new generation PV inverters

Appendix A – Cable/Line data

Table A1. Some selected underground cables and their properties

Cable ID	Conductor type	Cross-sectional area (mm2)	Diameter per conductor, d_c (cm) approx.	Insulation thickness, t_i (mm) avg.	Jacket or sheath thickness, t_{ts} (mm) avg.	Overall diameter, d_{ov} (mm) max.	R'$_{ph}$ per conductor appr. (ohm/km)	GMR per conductor (cm)	a (m)	Current carrying capacity buried @20C, appr.
LV-UG1	0.6/1kV NA2XY	4x35	0.668	0.9	1.8	30	1.113	0.260	0.8	140
LV-UG2	0.6/1kV NA2XY	4x70	0.944	1.1	2.0	38	0.568	0.368	0.8	197
LV-UG3	0.6/1kV NA2XY	4x95	1.1	1.1	2.1	40	0.411	0.428	0.8	237
LV-UG4	0.6/1kV NA2XY	4x120	1.24	1.2	2.3	48	0.325	0.475	0.8	269
LV-UG5	0.6/1kV NA2XY	4x150	1.38	1.4	2.4	53	0.265	0.531	0.8	305
LV-UG6	0.6/1kV NA2XY	4x240	1.75	1.7	2.8	59	0.162	0.671	0.8	400
MV-UG1	6/10kV NA2XSEY rm/16	3x50	0.798	3.4	2.5	51	0.822	0.311	0.8	165
MV-UG2	6/10kV NA2XSEY rm/16	3x70	0.944	3.4	2.5	55	0.568	0.368	0.8	203
MV-UG3	6/10kV NA2XSEY rm/16	3x95	1.1	3.4	2.5	58	0.411	0.428	0.8	242
MV-UG4	6/10kV NA2XSEY rm/16	3x120	1.24	3.4	2.5	62	0.325	0.483	0.8	276
MV-UG5	6/10kV NA2XSEY rm/25	3x150	1.38	3.4	2.5	66	0.265	0.537	0.8	309
MV-UG6	6/10kV NA2XSEY rm/25	3x185	1.53	3.4	2.5	69	0.211	0.596	0.8	351
MV-UG7	6/10kV NA2XSEY rm/25	3x240	1.75	3.4	2.5	75	0.162	0.681	0.8	408
MV-UG8	12/20kV NA2XS2Y rm/16	1x50	0.798	5.5	2.5	33	0.822	0.311	0.8	172
MV-UG9	12/20kV NA2XS2Y rm/16	1x70	0.944	5.5	2.5	35	0.568	0.368	0.8	210
MV-UG10	12/20kV NA2XS2Y rm/16	1x95	1.1	5.5	2.5	36	0.411	0.428	0.8	251
MV-UG11	12/20kV NA2XS2Y rm/16	1x120	1.24	5.5	2.5	38	0.325	0.483	0.8	285
MV-UG12	12/20kV NA2XS2Y rm/25	1x150	1.38	5.5	2.5	39	0.265	0.537	0.8	319
MV-UG13	12/20kV NA2XS2Y rm/25	1x185	1.53	5.5	2.5	41	0.211	0.596	0.8	361
MV-UG14	12/20kV NA2XS2Y rm/25	1x240	1.75	5.5	2.5	44	0.161	0.681	0.8	417
MV-UG15	12/20kV NA2XS2Y rm/25	1x300	1.95	5.5	2.5	46	0.129	0.759	0.8	471

Table A2. Some selected overhead (OHL) lines and their properties

Cable ID	Conductor type	Cross-sectional area (mm2)	Diameter per conductor, d_c (cm) approx.	Insulation thickness, t_i (mm) avg.	Jacket or sheath thickness, t_{ts} (mm) avg.	Overall diameter, d_{ov} (mm) max.	R'_{ph} per conductor appr. (ohm/km)	GMR per conductor (cm)	Current carrying capacity in open air @20C, appr.
MV-OHL1	6/10kV A2XS2YT rm/16	1x50	0.798	3.4	2.5	27	0.825	0.311	174
MV-OHL2	6/10kV A2XS2YT rm/16	1x70	0.944	3.4	2.5	28	0.572	0.368	217
MV-OHL3	6/10kV A2XS2YT rm/16	1x95	1.1	3.4	2.5	30	0.415	0.428	264
MV-OHL4	6/10kV A2XS2YT rm/16	1x120	1.24	3.4	2.5	32	0.329	0.483	316
MV-OHL5	6/10kV A2XS2YT rm/25	1x150	1.38	3.4	2.5	34	0.271	0.537	360
MV-OHL6	6/10kV A2XS2YT rm/25	1x185	1.53	3.4	2.5	36	0.217	0.596	416
MV-OHL7	6/10kV A2XS2YT rm/25	1x240	1.75	3.4	2.5	38	0.167	0.681	492
MV-OHL8	6/10kV A2XS2YT rm/25	1x300	1.95	3.4	2.5	40	0.135	0.759	565
MV-OHL9	12/20kV A2XS2YT rm/16	1x50	0.798	5.5	2.5	31	0.825	0.311	176
MV-OHL10	12/20kV A2XS2YT rm/16	1x70	0.944	5.5	2.5	32	0.572	0.368	220
MV-OHL11	12/20kV A2XS2YT rm/16	1x95	1.1	5.5	2.5	34	0.415	0.428	267
MV-OHL12	12/20kV A2XS2YT rm/16	1x120	1.24	5.5	2.5	36	0.329	0.483	324
MV-OHL13	12/20kV A2XS2YT rm/25	1x150	1.38	5.5	2.5	38	0.271	0.537	367
MV-OHL14	12/20kV A2XS2YT rm/25	1x185	1.53	5.5	2.5	40	0.217	0.596	422
MV-OHL15	12/20kV A2XS2YT rm/25	1x240	1.75	5.5	2.5	42	0.167	0.681	499
MV-OHL16	12/20kV A2XS2YT rm/25	1x300	1.95	5.5	2.5	44	0.135	0.759	572

Appendix B – Series impedance of lines/cables

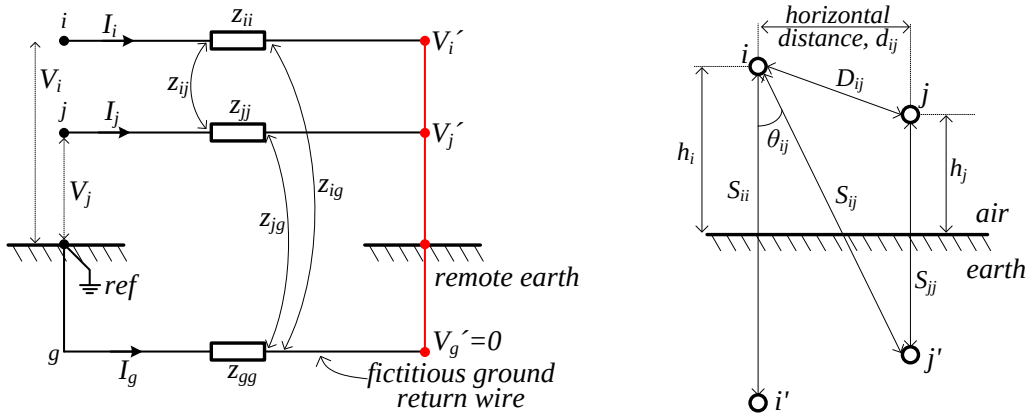

Figure B.1 Carson's two-conductor circuit with ground return (left); physical layout of two conductors with ground return (right)

Fig. B.1 illustrates Carson's line circuit and two-conductor line spacing layout with their image conductors. For unbalanced power flow situation, it is obvious that current injections will return to the source through the earth (fictitious ground wire). When receiving end nodes are shorted at the remote earth together, self- and mutual-impedances of conductors can be determined by knowing sending node voltages (V_i, V_j) and currents flowing along the conductors (I_i, I_j). Thus, as referenced to Fig. B.1 and applying Kirchoff's voltage law for the Carson's two-conductor circuit with shorted remote ends, the sending end voltages can be written as:

$$V_i = z_{ii} \cdot I_i + z_{ij} \cdot I_j + z_{ig} \cdot I_g + V_i'$$

$$V_j = z_{ji} \cdot I_i + z_{jj} \cdot I_j + z_{jg} \cdot I_g + V_j'$$

$$V_g = z_{gi} \cdot I_i + z_{gj} \cdot I_j + z_{gg} \cdot I_g + V_g'$$

All voltage terms V_i, V_j, V_i', V_j' represent node voltages referenced to their corresponding local earth. If writing above equations in closed form, (B.1) is obtained as:

$$\begin{bmatrix} \Delta V_i \\ \Delta V_j \\ \Delta V_g \end{bmatrix} = \begin{bmatrix} V_i - V_i' \\ V_j - V_j' \\ V_g - V_g' \end{bmatrix} = \begin{bmatrix} z_{ii} & z_{ij} & z_{ig} \\ z_{ij} & z_{jj} & z_{jg} \\ z_{ig} & z_{jg} & z_{gg} \end{bmatrix} \cdot \begin{bmatrix} I_i \\ I_j \\ I_g \end{bmatrix} \tag{B.1}$$

where $V_i' = V_j' = V_g'$, $V_g = 0$ and $I_i + I_j + I_g = 0$. Thus, reduced voltage equation for the *i*th *conductor* becomes:

$$V_i = \left(z_{ii} - 2 \cdot z_{ig} + z_{gg}\right) \cdot I_i + \left(z_{ij} - z_{ig} + z_{gg} - z_{gj}\right) \cdot I_j = \overline{z}_{ii} \cdot I_i + \overline{z}_{ij} \cdot I_j \tag{B.2}$$

so that

$$\begin{aligned} \overline{z}_{ii} &= z_{ii} - 2z_{ig} + z_{gg} \\ \overline{z}_{ij} &= z_{ij} - z_{ig} + z_{gg} - z_{gj} \end{aligned} \tag{B.3}$$

The set of equations in (B.3) can be used to extract self-ground (z_{gg}) and mutual-ground impedances (z_{ig}) if the ground-related terms are necessary.

Based on [3.25]-[3.26] and Fig. B.1 (right), self and mutual impedances can be determined by full Carson's equations as following:

$$\begin{aligned} \overline{z}_{ii} &= r_i + 4\omega \cdot G \cdot P_{ii} + j2\omega G \cdot \left(\ln \frac{S_{ii}}{GMR_i} + 2Q_{ii} \right) \quad \Omega/km \text{ or } \Omega/mile \\ \overline{z}_{ij} &= 4\omega \cdot G \cdot P_{ij} + j2\omega G \cdot \left(\ln \frac{S_{ij}}{D_{ij}} + 2Q_{ij} \right) \quad \Omega/km \text{ or } \Omega/mile \end{aligned} \tag{B.4}$$

where

$$P_{ij} = \frac{\pi}{8} - \frac{1}{3\sqrt{2}} r_{ij} \cos\left(\theta_{ij}\right) + \frac{r_{ij}^2 \cdot \cos\left(2\theta_{ij}\right)}{16} \cdot \left(0.6728 + \ln \frac{2}{r_{ij}} \right) + \frac{r_{ij}^2}{16} \cdot \theta_{ij} \cdot \sin\left(\theta_{ij}\right) + \frac{r_{ij}^3}{45\sqrt{2}} \cos\left(3\theta_{ij}\right) - \frac{\pi \cdot r_{ij}^4}{1536} \cos\left(4\theta_{ij}\right) \tag{B.5}$$

$$Q_{ij} = -0.0386 + \frac{1}{2}\cdot\ln\left(\frac{2}{r_{ij}}\right) + \frac{1}{3\sqrt{2}}\cdot r_{ij}\cdot\theta_{ij} - \frac{\pi\cdot r_{ij}^2}{64}\cdot\cos\left(2\theta_{ij}\right) + \frac{r_{ij}^3}{45\sqrt{2}}\cdot\cos\left(3\theta_{ij}\right) - \frac{r_{ij}^4}{384}\cdot\theta_{ij}\cdot\sin\left(4\theta_{ij}\right) - \frac{r_{ij}^4\cdot\cos\left(4\theta_{ij}\right)}{384}\cdot\left(\ln\left(\frac{2}{r_{ij}}\right) + 1.0895\right) \quad \text{(B.6)}$$

$$r_{ij} = 2.8099\cdot 10^{-3}\cdot S_{ij}\cdot\sqrt{\frac{f}{\rho}} \quad \text{(B.7)}$$

$$G = \begin{cases} 10^{-4}, & \text{for } \Omega/km \\ 0.1609347\cdot 10^{-3}, & \text{for } \Omega/mile \end{cases} \quad \text{(B.8)}$$

where

$\overline{Z}_{ii}$ is the self-impedance of conductor *i* in Ω/km or Ω/mile

$\overline{Z}_{ij}$ is the mutual-impedance between conductor *i* and conductor *j* in Ω/km or Ω/mile (Fig.B.1 *(right)*)

r_i is the resistance of conductor *i* in Ω/km or Ω/mile

f is the system frequency in Hz

h_i is the height of conductor *i* in meter ($S_{ii}=2h_i$)

GMR_i is the geometric mean radius of conductor *i* in meter

ρ is the resistivity of earth in Ω-meters

S_{ij} is the distance between conductor *i* and conductor *j'* (image of conductor *j*) in meter (Fig. B.1 *(right)*)

D_{ij} is the distance between conductor *i* and conductor *j* in meter

If full Carson's equations are further simplified by neglecting higher terms in (B.5) and (B.6) as:

$$P_{ij} \cong \frac{\pi}{8}$$

$$Q_{ij} \cong -0.0386 + \frac{1}{2}\ln\frac{2}{r_{ij}} = -0.0386 + \frac{1}{2}\cdot\ln\frac{2}{2.8099\cdot10^{-3}\cdot(2h_i)\cdot\sqrt{f/\rho}} \tag{B.9}$$

$$= -0.0386 + \frac{1}{2}\left(\ln\frac{2}{2\cdot(2.8099\cdot10^{-3})} + \ln\frac{\sqrt{\rho/f}}{h_i}\right)$$

and when the resulted P_{ij}, Q_{ij} terms from (B.9) are substituted into (B.4), the overall self- and mutual impedance of conductor including ground effects thus becomes:

$$\overline{z}_{ii} = r_i + \pi^2 fG + j4\pi fG\cdot\left(\ln\frac{S_{ii}}{GMR_i} + 5.7974 + \ln\frac{\sqrt{\frac{\rho}{f}}}{h_i}\right) \tag{B.10}$$

$$\overline{z}_{ij} = \pi^2 fG + j4\pi f\cdot G\cdot\left(\ln\frac{S_{ij}}{D_{ij}} + 6.4906 + \ln\frac{\sqrt{\frac{\rho}{f}}}{S_{ij}}\right) \tag{B.11}$$

After this point, the primitive series impedance matrix can be formed by using (B.10) and (B.11). It should be noticed that ground-related terms are already merged into the self- and mutual-impedances of phase and neutral conductors if Carson's equations are directly implemented [3.26]. Accordingly, the primitive series impedance matrix is given as:

$$z_{prim} = \begin{bmatrix} \overline{z}_{aa} & \overline{z}_{ab} & \overline{z}_{ac} & \overline{z}_{an} \\ \overline{z}_{ba} & \overline{z}_{bb} & \overline{z}_{bc} & \overline{z}_{bn} \\ \overline{z}_{ca} & \overline{z}_{cb} & \overline{z}_{cc} & \overline{z}_{cn} \\ \overline{z}_{na} & \overline{z}_{nb} & \overline{z}_{nc} & \overline{z}_{nn} \end{bmatrix} \tag{B.12}$$

Appendix C – Modelling data of IEEE 13-bus network

Fig. 3.20 depicts topology of IEEE 13-bus test network. Various lines and cable structures, transformers, shunt capacitors, loads and line drop compensator (LDC) are tested all together [3.41].

Typical physical layouts of overhead lines and underground cables are illustrated in Fig. 3.10 and summarized in Table C.1. Overhead line and underground cable configurations used in IEEE 13-bus test network employ these physical layouts as presented in Table C.2.

Accordingly, the other modelling data are provided in Table C.3-Table C.

Table C.1 Typical layout IDs based on Fig. 3.10

Layout ID	*Description*	*OHL or UG*
ID 500	3-phase 4-wire	overhead line
ID 505	2-phase 3-wire	
ID 510	1-phase 2-wire	
ID 515	3-phase 3 conductor	underground cable
ID 520	1-phase 2 conductor	

Table C.2 Line and cable configurations for IEEE 13-bus test network [3.41]

Configuration	*Phase placements*	*Phase conductors*	*Neutral conductor*	*Layout ID*	*OHL or UG*
CON 601	B-A-C-N	556,500 26/7 ACSR	4/0 6/1 ACSR	ID 500	overhead line
CON 602	C-A-B-N	4/0 6/1 ACSR	4/0 6/1 ACSR	ID 500	
CON 603	C-B-N	1/0 ACSR	1/0 ACSR	ID 505	
CON 604	A-C-N	1/0 ACSR	1/0 ACSR	ID 505	
CON 605	C-N	1/0 ACSR	1/0 ACSR	ID 510	
CON 606	A-B-C-N	250,000 AA Concentrated Neut.	None	ID 515	underground cable
CON 607	A-N	1/0 AA Tape-shielded	1/0 Cu	ID 520	

Table C.3 Branch data for IEEE 13-bus test network [3.41]

"From Bus"	*"To Bus"*	*Length (ft.)*	*Configuration*
2	5	500	CON 603
2	7	500	CON 602
7	8	0	Transformer
5	6	300	CON 603
13	2	2000	CON 601
9	12	800	CON 607
2	3	2000	CON 601
3	9	300	CON 604
3	4	1000	CON 601
3	11	500	CON 606
9	10	300	CON 605

Table C.4 Transformer data used for IEEE 13-bus test network [3.41]

	Rated power (MVA)	*Primary side*	*Secondary side*	*R (%)*	*X (%)*
Transformer	0.5	Yg, 4.16 kV_{LL}	Yg, 0.48 kV_{LL}	1.1	2

Table C.5 Capacitor data used for IEEE 13-bus test network [3.41]

	Rated kVAr for Yg connection		
Bus no	*Ph-A*	*Ph-B*	*Ph-C*
11	200	200	200
10	0	0	100

Table C.6 Spot load data for IEEE 13-bus test network [3.41]

		Ph-A or Ph-AB		*Ph-B or Ph-BC*		*Ph-C or Ph-CA*	
Bus no	*Load type*	*P (kW)*	*Q (kVAr)*	*P (kW)*	*Q (kVAr)*	*P (kW)*	*Q (kVAr)*
8	Y-PQ	160	110	120	90	120	90
5	Y-PQ	0	0	170	125	0	0
6	D-Z	0	0	230	132	0	0
12	Y-Z	128	86	0	0	0	0
3	D-PQ	385	220	385	220	600	420
11	Y-PQ	485	190	68	60	290	212
10	Y-I	0	0	0	0	170	80

Table C.7 LDC data for IEEE 13-bus test network [3.41]

Branch segment			
13 - 2			
Connection type			
3-phase, line-to-ground			
Bandwidth (V)			
2.0			
N_{VT} *ratio*			
20			
CT_p *primary rating (A)*			
700			
	Compensator settings		
	Ph-A	*Ph-B*	*Ph-C*
$R_{comp,V}$	3	3	3
$X_{comp,V}$	9	9	9
V_{SET}	122	122	122

Publications

I. Demirok, E., Sera, D., Teodorescu, R., Rodriguez, P., Borup, U., "Clustered PV inverters in LV networks: An overview of impacts and comparison of voltage control strategies", *Electric Power and Energy Conference (EPEC 2009)*, Canada.

II. Demirok, E., Sera, D., Teodorescu, R., Rodriguez, P., Borup, U., "Evaluation of the voltage support strategies for the low voltage grid connected PV generators", *IEEE Energy Conversion Congress and* Exposition, ECCE 2010, Atlanta, USA.

III. Demirok, E., Frederiksen, K.H.B., Sera, D., Teodorescu, R., "An optimized reactive power control of distributed solar inverters in LV networks", *26th European Photovoltaic Solar Energy Conference and Exhibition (EUPVSEC)*, Hamburg, September 2011.

IV. Demirok, E., Gonzalez, P.C., Svendsen, M.C., Frederiksen, K.H.B., Sera, D., Teodorescu, R., "Reactive power control strategy for distributed solar inverters in low voltage rural distribution grids without communication infrastructure", *IEEE Photovoltaic Specialists Conference (PVSC)*, Seattle, 2011.

V. Demirok, E., Sera, D., Rodriguez, P., Teodorescu, R., "Enhanced local grid voltage support method for high penetration of distributed generators", *37th IEEE Annual Conference of Industrial Electronics Society (IECON)*, Melbourne, 7-10 November 2011.

VI. Demirok, E., Sera, D., Teodorescu, R., "Estimation of maximum allowable PV connection to LV residential power networks: A case study of Braedstrup", *1st International Workshop on Integration of Solar Power into Power Systems*, 24 October 2011, Aarhus, Denmark.

VII. Demirok, E., Gonzalez, P., Frederiksen, K.H.B., Sera, D., Rodriguez, P., Teodorescu, R., "Local reactive power control methods for overvoltage prevention of distributed solar inverters in low voltage grids", *IEEE Journal of Photovoltaics*, vol. 1, issue. 2, p. 174-182, 2011.